Measurement of beauty-production in deep inelastic scattering at HERA II

Dissertation
zur Erlangung des Doktorgrades
des Fachbereichs Physik
der Universität Hamburg

vorgelegt von
Benjamin Kahle
aus Hamburg

Hamburg
2005

Gutachter der Dissertation:	Dr. A. Geiser Prof. Dr. R. Klanner
Gutachter der Disputation:	Dr. A. Geiser Prof. Dr. G. Heinzelmann
Datum der Disputation:	25.11.2005
Vorsitzender des Prüfungsausschusses:	Dr. H. D. Rüter
Vorsitzender des Promotionsausschusses:	Prof. Dr. G. Huber
Dekan des Fachbereichs Physik:	Prof. Dr. G. Huber

Kurzfassung

Diese Dissertation beschreibt eine Messung der Produktion von Beauty-Quarks in tief unelastischer Streuung am ep-Speicherring HERA bei $\sqrt{s} = 318\,\text{GeV}$. Die Messung wurde auf einem Datensatz mit einer integrierten Luminosität von $39\,\text{pb}^{-1}$ durchgeführt, der am ZEUS Experiment in den Jahren 2003/2004 gesammelt wurde.

Die Theorie der starken Kraft, die Quanten-Chromodynamik (QCD), bietet Methoden zur Berechnung von Wirkungsquerschnitten der Beauty-Quark-Produktion. Es wird erwartet, dass diese Berechnungen verlässlich sind wenn eine große Skala, hier die Masse des Beauty-Quarks, vorhanden ist. Daher bietet diese Messung die Möglichkeit, Vorhersagen der QCD zu testen.

In der hier vorgestellten Analyse werden Ereignisse ausgewählt, wenn sie ein gestreutes Elektron, einen Jet und ein Myon in diesem Jet enthalten. Um eine hohe Effizienz des Myon Nachweises zu erhalten, wird die Redundanz verschiedener Myon Detektoren ausgenützt. Diese Methode erlaubt die Auswahl von Myonen in einem großen Pseudo-Rapiditäts-Bereich mit einer niedrigen Transversal-Impuls Schwelle.

Der Anteil der Ereignisse die Beauty-Quarks enthalten wurde mit Hilfe der charakteristischen Verteilung der Transversal-Impulse der Myonen relativ zu den zugehörigen Jets bestimmt. Der totale sichtbare Wirkungsquerschnitt wurde gemessen als

$$\sigma^{b\bar{b}}(ep \to e\, b\bar{b}\, X \to e\, jet\, \mu\, X') = 57.9 \pm 5.8(\text{stat.})^{+3.5}_{-8.1}(\text{syst.})\,\text{pb}.$$

Der kinematische Bereich dieser Messung ist definiert durch: $Q^2 > 4\,\text{GeV}^2$, $y > 0.05$ und $y < 0.7$, ein Jet entstanden aus einem Beauty-Quark mit: $E^{jet}_{t,lab} > 5\,\text{GeV}$ und $-2 < \eta^{jet} < 2.5$ und einem Myon aus dem direkten oder indirekten Zerfall eines Beauty-Quarks innerhalb dieses Jets mit: $p^{\mu}_t > 1.5\,\text{GeV}$ und $\eta^{\mu} > -1.6$.
Der gemessene Wirkungsquerschnitt ist um einen Faktor 2.36 größer als die Vorhersage von Monte-Carlo-Simulationen (MC), die Matrix-Elemente in führender Ordnung mit Parton-Showern verwenden. Diese Unterschätzung der Beauty-Produktion ist typisch für diese Art von MC-Simulationen und wurde auch in anderen Analysen gemessen.

Differentielle Wirkungsquerschnitte in p^{μ}_t und η^{μ}, in p^{jet}_t und η^{jet} und in Q^2 wurden gemessen. Die Form aller Datenverteilungen wird von den MC-Vorhersagen innerhalb der statistischen und systematischen Unsicherheiten beschrieben.

Ein Vergleich mit nächstführender Ordnung (NLO) QCD Rechnungen wurde in einem kinematischen Bereich durchgeführt in dem NLO QCD Rechnungen einer ähnlichen früheren Analyse vorlagen. Das Ergebnis der Messung des totalen sichtbaren Wirkungsquerschnitts ist in Übereinstimmung mit der früheren Analyse und der NLO QCD Vorhersage. Auch die differentiellen Wirkungsquerschnitte $d\sigma/dp^{\mu}_t$ stimmen innerhalb der Unsicherheiten mit den NLO QCD Rechnungen in diesem Phasenraum überein. Die neue Messung zeigt einen geringeren Überschuss im Bereich kleiner p^{μ}_t im Vergleich zu der QCD Vorhersage als die frühere Analyse. In diesem Bereich war die signifikanteste Abweichung zwischen Messung und Vorhersage in der früheren Analyse festgestellt worden.

Außerdem wurden doppelt differentielle Wirkungsquerschnitte $d^2\sigma/dQ^2dx$ gemessen mit Ergebnissen, die in der Form gut mit MC-Vorhersagen übereinstimmen. Die doppelt differentiellen Wirkungsquerschnitte sind nötig für die Messung des Beauty-Anteils an der Proton-Strukturfunktion $F_2^{b\bar{b}}$. Die gute Beschreibung der Daten durch die MC-Simulation, die in dieser Messung beobachtet wurde, ist eine notwendige Bedingung für eine zuverlässige Extrapolation zu $F_2^{b\bar{b}}$.

In den HERA II Daten erlaubt die verbesserte Vertexauflösung bei Verwendung des Mikro-Vertex-Detektors (MVD) die Messung von Stoßparametern. Eine erste Stoßparameterverteilung zeigt, dass die Unsicherheiten aller vorgestellten Messungen durch die Verwendung der Stoßparamter-Methode deutlich verringert werden können.

Abstract

This thesis presents a measurement of beauty quark production in deep inelastic scattering at the *ep*-collider HERA at $\sqrt{s} = 318\,\mathrm{GeV}$. The measurement is based on data collected at the ZEUS detector in the years 2003/2004, using an integrated luminosity of $39\,\mathrm{pb}^{-1}$.

The theory of the strong force, Quantum Chromodynamics (QCD) offers methods to calculate cross sections of beauty quark production. These calculations are expected to be reliable if a hard scale, here the mass of the beauty quark, is present in the process. Thus this measurement provides the opportunity to test the predictions of QCD.

In the analysis presented in this thesis, events were selected that contain a scattered electron, a jet and a muon inside the jet. To reach a high efficiency the redundancy of different muon detectors was exploited. This method allows the selection of muons covering a large pseudo-rapidity range with a low transverse momentum threshold.

The fraction of events from beauty quark production was extracted using the characteristic distribution of the transverse momenta of muons relative to the associated jets. The total visible cross section was measured to be:

$$\sigma^{b\bar{b}}(ep \to e\, b\bar{b}\, X \to e\, jet\, \mu\, X') = 57.9 \pm 5.8(\mathrm{stat.})^{+3.5}_{-8.1}(\mathrm{syst.})\,\mathrm{pb}$$

in the kinematic region defined by: $Q^2 > 4\,\mathrm{GeV}^2$, $y > 0.05$ and $y < 0.7$,
one jet originating from a beauty quark with: $E^{jet}_{t,lab} > 5\,\mathrm{GeV}$ and $-2 < \eta^{jet} < 2.5$
and a muon originating from a beauty quark decay (direct or indirect) included in this jet with: $p^{\mu}_t > 1.5\,\mathrm{GeV}$ and $\eta^{\mu} > -1.6$.
The measured cross section is a factor of 2.36 higher than predicted by Monte Carlo simulations (MC) using leading order matrix elements with parton showers. This underestimation of beauty production is typical for this kind of MC simulations and was seen also in other analyses.

Differential cross sections were measured in p^{μ}_t and η^{μ}, in p^{jet}_t and η^{jet} and in Q^2. The shape of all data distributions are described by the MC prediction within errors.

A comparison of measured cross sections to next-to-leading order (NLO) QCD calculations was performed in a kinematic range where NLO QCD calculations from a similar previous analysis are available. Both the total visible cross section and the differential cross sections $d\sigma/dp^{\mu}_t$ are in agreement with the previous measurement and the NLO QCD predictions in this region of phase space within errors. The new measurement shows a smaller excess compared to the NLO QCD predictions than the previous analysis in the region of low p^{μ}_t, where the most significant discrepancy was seen.

Furthermore, double differential cross sections $d^2\sigma/dQ^2dx$ were measured and the results are found to be in good agreement with the shape of the MC predictions. The double differential cross sections are necessary for a measurement of the beauty contribution to the proton structure function $F_2^{b\bar{b}}$. The good description of the data by the MC, that is found in this measurement, is a necessary condition for a reliable extrapolation to $F_2^{b\bar{b}}$.

For HERA II data the improved vertex resolution using the Micro Vertex Detector (MVD) allows the measurement of impact parameters. A first impact parameter distribution shows, that the uncertainties of all presented measurements can be reduced significantly using the impact parameter method.

Contents

Chapter 1

Introduction

The theory of elementary particle physics, the Standard Model, very successfully describes measurements of many experiments. Quantum Chromodynamics (QCD) is a part of the Standard Model that offers methods to calculate cross sections of interactions by the strong force. QCD calculations are expected to be reliable if a hard scale is present in the process. One hard scale in heavy quark production is the quark mass that is larger than the energy scale at which quarks are confined into hadrons, $\Lambda \sim 250\,\mathrm{MeV}$. While QCD calculations provide an acceptable description of charm quark production ($m_c \sim 1.3\,\mathrm{GeV}$), it is expected that the description is even more precise for the production of the heavier beauty quark ($m_b \sim 4.4\,\mathrm{GeV}$). This process was measured in different experiments at different accelerators. In early experiments at the Tevatron $p\bar{p}$-collider (D0 [Abb00] and CDF [Abe96]) the production rate was significantly higher than predicted. After recent improvements of the experiments and the theoretical calculations, data and QCD calculations are in good agreement [Aco05]. At the HERA ep-collider experiments (the most relevant measurements for this analysis are at H1 [Akt05, Akt05b] and at ZEUS [Che04b, Gut05]) discrepancies between data and QCD calculations are found only in specific regions of phase space (e.g. at low transverse momentum p_t^μ and large pseudo-rapidity η^μ of a muon from semi-leptonic beauty decay).

In deep inelastic scattering at HERA, the proton can be described to a good approximation in terms of a single proton structure function $F_2(Q^2, x)$ depending only on the photon virtuality Q^2 and the Bjørken scaling variable x. The measurement of the contribution of beauty quarks to the proton structure function ($F_2^{b\bar{b}}$) is one goal of this analysis.
The dominant process to produce beauty quarks in ep-collisions is boson-gluon-fusion (BGF) with a boson (a photon) from the electron and a gluon from the proton. Thus this process measures indirectly the gluon content of the proton and contributes to F_2.

Furthermore, the interaction of photons with quarks inside the proton (quark parton model or QPM-like processes) provide insights into the proton quark structure. While the quark content of the proton consists mainly of light quarks, heavy quarks are produced dynamically in the splitting of a gluon into a virtual quark pair. At high photon virtuality ($Q^2 \gg (2m_b)^2$) this process can be reinterpreted to occur inside the proton.

$F_2^{b\bar{b}}$ then measures the virtual beauty quark pairs in the proton.
The process measured in this analysis, the semi-leptonic decay of a beauty quark into a muon and a jet in deep inelastic scattering at HERA:

$$e\,p \rightarrow e\,b\bar{b}\,X \rightarrow e\,\mu\,jet\,X'$$

has a clean signature in the detector and thus allows a good background rejection. The fraction of signal events is determined on a statistical basis using the high transverse momentum of the muon relative to the jet in beauty quark decays.

In addition to leading to a measurement of $F_2^{b\bar{b}}$ as discussed above, cross sections in this channel also test the validity of perturbative QCD.

In a similar earlier analysis [Che04b], QCD predictions underestimate the data. Differences of more than two standard deviations are found e.g. at low transverse momentum as well as low pseudo-rapidity of the muon.

The analysis described in this thesis measures in an extended kinematic region compared to the previous analysis and uses a combination of multiple detector components for muon identification. This allows a lower muon transverse momentum threshold and a higher detection efficiency to investigate these regions of phase space further.

In the Breit frame, defined by $q + 2xP = 0$, where q is the momentum of the exchanged photon, x is the Bjørken scaling variable and P is the proton momentum, a space-like photon and a proton collide head-on. The reconstruction of jets in the Breit frame is useful to suppress QPM-like processes and to select only the main beauty production process, BGF. With this method the previous analysis reached a high signal-to-background ratio in the selected event sample but only in a low statistics sample.

In order to measure the beauty contribution to the proton structure function $F_2^{b\bar{b}}$, beauty quarks produced in BGF and QPM-like events have to be included. Therefore in the analysis described in this thesis, jets are reconstructed in the laboratory system.

In this thesis the measurement of the integrated beauty cross section and of differential cross sections in p_t^μ, η^μ, p_t^{jet}, η^{jet} and Q^2 are presented. Furthermore the main measurement for the determination of $F_2^{b\bar{b}}$, double differential cross sections $d^2\sigma/dQ^2dx$ are part of this thesis.
This analysis is performed on a data sample, taken at the ZEUS detector in the years 2003/04 reaching a luminosity of $39\,\mathrm{pb}^{-1}$. This thesis is organized as follows:
Chapter 2 gives an overview of the theoretical framework for this analysis. Deep inelastic scattering in electron-proton collisions and production mechanisms of heavy quarks are discussed. Furthermore the transition from quarks to jets of hadrons and the differences of jets in the Breit frame and the laboratory frame are described. This chapter ends with an outline of beauty hadron properties.
Results of beauty quark measurements at different experiments, focusing on measurements most relevant to this analysis, are reviewed in **Chapter 3**.
Chapter 4 introduces the experimental environment, the ZEUS detector at HERA, used for this analysis.
The methods and detector components used to reconstruct event quantities at ZEUS

are introduced in **Chapter 5**. The emphasis is placed on the reconstruction of muons. Also the detection of the scattered electron and the reconstruction of jets are described. The method to determine the signal-to-background ratio, the p_t^{rel} method, is explained in this chapter.
The Monte Carlo samples of signal and background and the data samples for this analysis are defined in **Chapter 6**.
The cuts applied to the reconstructed events to suppress background events are shown in **Chapter 7**. The resulting quality of the description of the data by the Monte Carlo is checked using distributions of different quantities.
The cross section measurements for beauty production in DIS are presented in **Chapter 8**. As a comparison with the previous analysis, jets in the Breit frame and a compatible kinematic region are used for a differential cross section measurement. After this check, the cross sections in the expanded kinematic region with jets in the laboratory frame are presented. Furthermore differential and double differential cross sections are shown.
An outlook on planned improvements and further measurements is given in **Chapter 9**.
Chapter 10 concludes the results of this analysis.

Chapter 2

Theory

In this chapter the theoretical framework for this analysis are described. Starting with a short introduction into the Standard Model of particle physics the properties of electron proton scattering, in particular the deep inelastic scattering, are characterized. An overview of QCD, the theory of strong interactions, follows. The production of heavy quarks, in particular beauty quarks, and its relevance as a precise test of QCD is outlined. This chapter ends with the description of beauty hadrons and their decay.

2.1 The Standard Model

The *Standard Model* (SM) [Gri87, Hal84] of particle physics is a theory to describe the elementary particles and their interactions. In the SM, all matter is made out of two kinds of elementary particles: leptons and quarks and their anti-particles, spin-1/2 fermions. They are grouped into three generations. The leptons are: electron with electron-neutrino, muon with muon-neutrino and tau with tau-neutrino. The quarks are similarly ordered into up (**u**) and down (**d**), strange (**s**) and charm (**c**) and beauty (**b**) and top (**t**) (see Tab. 2.1). These particles interact by three fundamental interactions,

	Generations			Interactions		
				el.magn.	weak	strong
Leptons	$\begin{pmatrix} e \\ \nu_e \end{pmatrix}$	$\begin{pmatrix} \mu \\ \nu_\mu \end{pmatrix}$	$\begin{pmatrix} \tau \\ \nu_\tau \end{pmatrix}$	-1 no	yes yes	no no
Quarks	$\begin{pmatrix} u \\ d \end{pmatrix}$	$\begin{pmatrix} c \\ s \end{pmatrix}$	$\begin{pmatrix} t \\ b \end{pmatrix}$	$+2/3$ $-1/3$	yes yes	yes yes

Table 2.1: The fundamental particles in the Standard Model and their interactions.

described by exchanges of (virtual) gauge vector bosons (see Tab. 2.3). Gravitation is not incorporated into the Standard Model.

	particle	mass/ MeV
quarks	u	1.5 to 4
	d	4 to 8
	s	80 to 130
	c	1150 to 1350
	b	4100 to 4400
	t	174300 ± 5100
leptons	e	0.51100
	μ	105.66
	τ	1777.0
	ν_e	< 0.003
	ν_μ	< 0.19
	ν_τ	< 18.2
bosons	γ	$< 6 \cdot 10^{-20}$
	g	0
	$W^\pm$	80425 ± 38
	Z^0	91188 ± 2

Table 2.2: Masses of Standard Model particles [Eid04]

The group structure of the Standard Model is

$$SU(3)_C \times SU(2)_L \times U(1)_Y, \tag{2.1}$$

where $U(n)$ denotes the group of all unitary $n \times n$ matrices and $SU(n)$ is the group of all unitary $n \times n$ matrices with determinant 1. The weak and electromagnetic interaction are unified in the gauge group $SU(2)_L \times U(1)_Y$. The masses of the exchange bosons of the weak interaction are described by a process called *spontaneous symmetry breaking*. The masses are [Eid04]: $M_W = 80.43\,\text{GeV}$ and $M_{Z^0} = 91.19\,\text{GeV}$[1]. All charged particles can exchange virtual photons, the mediators of electromagnetism, described by *quantum electrodynamics* (QED). The strong force is described by *quantum chromodynamics* (QCD) as a $SU(3)_C$ gauge group. The charge of the strong force, denoted as *color*, is carried by the massless gluons. Each quark has a color state assigned, a linear combination of three colors and anti-colors. Bare quarks are not seen experimentally, all particles observed are colorless doublets (quark and anti-quark) or triplets (three quarks). The doublets are called mesons, the triplets denoted as baryons[2]. If one of the quarks or gluons carrying color is, in a hard interaction, kicked out of the meson or baryon, quark anti-quark pairs are produced in order to keep the resulting particles colorless. Leptons do not carry any color and are not directly affected by the strong interaction. The weak interaction affects all quarks and leptons.

[1] in this thesis the convention $c = 1$ and $\hbar = 1$ is used, unless stated explicitely otherwise

[2] also states of five quarks, called *pentaquarks* may have been observed [Che04].

Interaction	boson	Q_{EM}	related group	typical coupling
strong	8 g	0	$SU(3)_C$	1
el.magn.	γ	0	$SU(2)_L \times U(1)_Y$	10^{-2}
weak	Z^0	0	$SU(2)_L \times U(1)_Y$	10^{-6}
	$W^{\pm}$	1		

Table 2.3: The fundamental interactions in the Standard Model. The strength of the interactions is given by their couplings at very low energies $E \ll m_p$.

2.2 Kinematics of *ep*-scattering

In the Standard Model the interaction between particles like electrons and protons can be described by the exchange of a vector boson. In the case that the exchanged boson is a photon (γ) or a Z^0 the interaction is called neutral current scattering (NC); if the boson is a $W^{\pm}$ the reaction is called charged current scattering (CC) (Figure 2.1). The four-

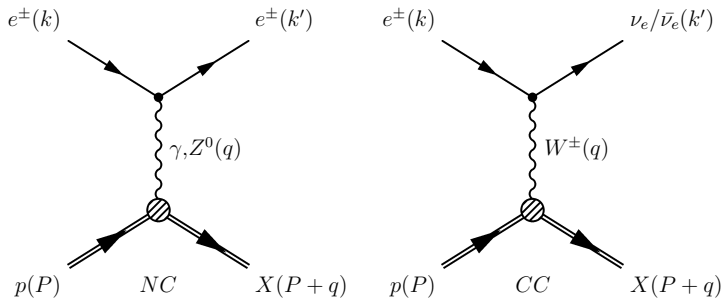

Figure 2.1: Charged current (CC) and neutral current (NC) diagrams of electron-proton scattering. The four-vectors of the particles are given in parentheses.

momenta of the incoming and outgoing electron are denoted k and k' respectively, the momentum of the proton is denoted P. The exchanged boson has the four-momentum q, given by

$$q = k - k'. \tag{2.2}$$

The scattering is described by the following variables:

$$Q^2 = -q^2 \tag{2.3}$$
$$s = (k+P)^2 \tag{2.4}$$
$$y = \frac{P\cdot q}{P\cdot k}, \quad 0 \le y \le 1 \tag{2.5}$$

$$x = \frac{Q^2}{2P\cdot q}, \quad 0 \le x \le 1 \tag{2.6}$$

with Q^2 as the virtuality of the exchanged boson. s is the total center-of-mass energy squared, the *inelasticity* y describes the relative energy transfer from the lepton to the hadronic system in the proton rest frame. x is called *Bjørken scaling variable*. In the Quark Parton Model (see Sec. 2.3.2) x can be interpreted as the fraction of the proton momentum carried by the interacting parton. In the case the proton and electron masses are neglected Equation 2.4 and 2.5 can be simplified to:

$$s = (k+P)^2 \approx 2k\cdot P \tag{2.7}$$
$$y = \frac{P\cdot q}{P\cdot k} \approx \frac{2P\cdot q}{s} \tag{2.8}$$
$$\tag{2.9}$$

and the boson virtuality Q^2 can be expressed as the product of x, y and s:

$$Q^2 = sxy. \tag{2.10}$$

The center-of-mass energy $\sqrt{s}$ is fixed at HERA to a value of 318 GeV by the beam energies (see Chapter 4). Thus only two of the four variables are independent. The variable W, the invariant mass of the hadronic system recoiling against the scattered lepton, can be expressed as

$$W^2 = (P+q)^2 = P^2 + q^2 + 2P\cdot q \approx -Q^2 + ys. \tag{2.11}$$

Scattering processes are experimentally divided into two regions of phase space. Events with a virtuality of the exchanged photon $Q^2 \approx 0$, i.e. quasi-real photons, are classified as *photoproduction* (PHP) events. Events of Q^2 above a few GeV^2 and $W^2 \gg m_P^2$ (with the proton mass m_P) are referred to as *deep inelastic scattering* (DIS).

2.3 Deep Inelastic Scattering

This thesis focuses on beauty production in *neutral current deep inelastic scattering* (NC DIS). The term *deep* refers to $Q^2 \gg m_P^2$, whereas *inelastic* means $W^2 \gg m_P^2$. The process can be seen as the probing of an object (the proton) with very short wavelength (of the photon) to detect very small details (quarks and gluons) of the object. The Q^2 range at HERA up to about 40000 GeV^2 is equivalent to a resolution of 1/1000 of the proton radius, applying $\lambda \approx \hbar c/\sqrt{Q^2} = 10^{-18}$ m.

2.3.1 Inclusive DIS cross section

The inclusive cross section for NC DIS can be expressed as a function depending on Q^2 and x [Bor33]:

$$\frac{d^2\sigma_{NC}}{dxdQ^2} = \frac{2\pi\alpha_{em}^2}{xQ^4}\left[\tilde{F}_2(1+(1-y)^2) + x\tilde{F}_3(1-(1-y)^2) + y^2\tilde{F}_L\right] \tag{2.12}$$

$\tilde{F}_2(x,Q^2)$, $\tilde{F}_3(x,Q^2)$ and $\tilde{F}_L(x,Q^2)$ are generalized *Structure Functions*, which include coupling constants, propagator terms and Structure Functions for exchange of γ, Z^0 and γZ^0 interference terms respectively. For CC DIS similar equations can be derived. The *Structure Functions* F_i are functions of the variables x and Q^2 describing the distribution of electrical charge within the proton. The unpolarized cross sections for NC and CC DIS, differentiated in x and y are [Eid04]:

$$\frac{d^2\sigma_{NC}}{dxdy} = \frac{4\pi\alpha_{em}^2}{xyQ^4} \left[\left(1-y-\frac{x^2y^2M^2}{Q^2}\right)F_2^{NC}+y^2xF_1^{NC}\mp\left(y-\frac{y^2}{2}\right)xF_3^{NC}\right] \quad (2.13)$$

$$\frac{d^2\sigma_{CC}}{dxdy} = \frac{4\pi\alpha_{em}^2}{xyQ^4}(1\pm\lambda^2)\frac{1}{2}\left(\frac{G_FM_W^2}{4\pi\alpha_{em}}\frac{Q^2}{Q^2+M_W^2}\right)^2 \left[\left(1-y-\frac{x^2y^2M^2}{Q^2}\right)F_2^{CC}+y^2xF_1^{CC}\mp\left(y-\frac{y^2}{2}\right)xF_3^{CC}\right] \quad (2.14)$$

where α_{em} is the fine structure constant and G_F the Fermi constant. The charged current Structure Functions F_1^{CC}, F_2^{CC} and F_3^{CC} are the result of $W^\pm$ exchange. The neutral current Structure Functions F_1^{NC}, F_2^{NC} and F_3^{NC} are determined by photon and Z^0 exchange and by their interference. The Z^0 exchange, or $W^\pm$ for CC, is suppressed relative to the γ exchange for Q^2 lower than the squared mass of the exchanged boson:

$$\frac{\sigma(Z^0,W^\pm)}{\sigma(\gamma)} \sim \left(\frac{Q^2}{Q^2+M_{Z^0,W^\pm}^2}\right)^2 \quad (2.15)$$

with M_{Z^0} and $M_{W^\pm}$ as the mass of the Z^0 and $W^\pm$ respectively. In this Q^2 regime the photon mediated NC DIS process dominates (compare Fig. 2.2), the term $x\tilde{F}_3$ in Equation 2.12 becomes negligible and $\tilde{F}_2$ can be reduced to the electromagnetic Structure Function F_2^{em}. Without the small contribution of longitudinal polarized photons, included in the term $y^2\tilde{F}_L$, the cross section becomes:

$$\frac{d^2\sigma^{NC}}{dxdQ^2} = \frac{2\pi\alpha^2}{xQ^4}\left[F_2(x,Q^2)(1+(1-y)^2)\right]. \quad (2.16)$$

2.3.2 Quark Parton Model

A simple model, useful to understand many aspects of deep inelastic scattering, is the *Quark Parton Model*. In 1969 two models, the *Quark Model* [Gel64] and the *Parton Model* [Fey69] were developed to describe the proton. In the Parton Model the constituents of the proton are quasi-free point-like *partons*. The momentum of the proton p is carried by the partons: $p_i = \xi_i p$, where ξ_i $(0 \le \xi_i \le 1)$ is the fraction of total proton momentum carried by parton i. In this model the DIS cross section is the incoherent

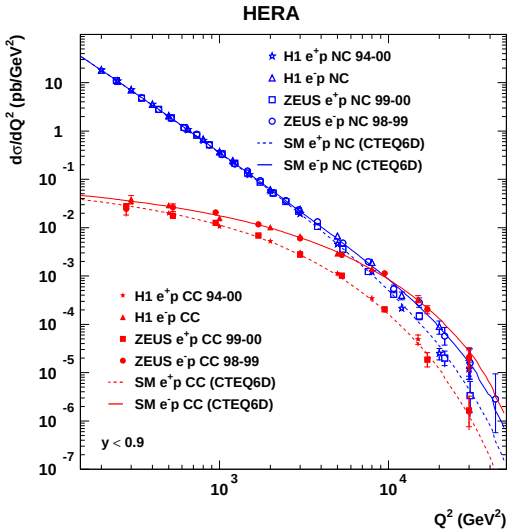

Figure 2.2: Inclusive differential charged current (CC) and neutral current (NC) cross sections as a function of Q^2 from the ZEUS and H1 collaborations [Gab04]. The Standard Model predictions for NC and CC DIS are shown in solid and dashed lines respectively. The suppression of the CC cross section with respect to the NC cross section is visible at Q^2 values lower than the $W^\pm$ mass squared.

sum of elastic scattering processes of the electron off the partons:

$$\frac{d^2\sigma}{dxdQ^2} = \sum_{i=\text{partons}} e_i^2 \cdot f_i(x,Q^2)\left(\frac{d^2\sigma_i}{dxdQ^2}\right). \quad (2.17)$$

where e_i is the charge of parton i and $f_i(x,Q^2)$ is the probability of probing parton i carrying a momentum fraction between x and $x+dx$ in the proton. A prediction of this model is the independence of the proton structure of Q^2. This effect is called *scale invariance* and was predicted by Bjørken [Bjo69]. Only three partons are constituents of the proton in the Parton Model, even at higher momentum transfer no new substructure of the proton becomes visible. In the high Q^2 limit ($Q^2 \to \infty$) but x finite, referred as *infinite momentum frame*, the partons can be considered massless and all transverse momenta are negligible. In the proton infinite momentum frame, the interactions between partons can be ignored, due to the Lorenz time dilatation. The other partons do not participate in the hard interaction and are called *spectator partons*. In this model

the Structure Functions $F_{1,2}$, are functions of x (the Bjørken scaling variable) but not of Q^2. In this frame x can be interpreted as the longitudinal momentum fraction of the proton ξ carried by the interacting parton.

The identification of quarks as the partons of the Parton Model, led to the Quark Parton Model (QPM). In the QPM $F_{1,2}$ can be expressed as a sum of quark and anti-quark densities. They are related to each other by the Callan-Gross relation [Cal69]

$$F_2 = 2xF_1. \tag{2.18}$$

This equation was experimentally confirmed at SLAC [Blo69] and it proved that the charged partons of the proton are spin 1/2 particles (for spin 0 the prediction $2xF_1/F_2 = 0$ leads to an inconsistency with the data).

The Structure Functions are not yet calculable from first principles but have to be measured in experiments. The QPM predicts the independence of the Structure Functions from the virtuality of the photon Q^2 at high energies and that $F_{1,2}$ depends only on the scaling variable x. Later the violation of this prediction was found (see Fig. 2.7). Only about half the momentum of the proton is carried by the *valence quarks*. Valence quarks are the three quarks (uud) in the proton, mentioned earlier. For $x \ll 0.1$ the Structure Functions increase for increasing values of Q^2. This behavior was later explained by quantum chromodynamics (QCD).

2.3.3 Quantum Chromodynamics

In the theory of QCD the quarks can not be treated as free particles, but they exchange gluons. QCD is a renormalizable non-Abelian gauge theory, describing the strong interaction as exchange of gluons. The gluons and the quarks couple via color charges. Each quark or anti-quark holds one of the three colors or anti-colors respectively. The symmetry of QCD is therefore $SU(3)$. 8 independent linear combinations of color-anti-color exist, represented by 8 different gluons.

Perturbative QCD (pQCD) offers a method to calculate cross sections as power series in the coupling constant of the strong interaction α_s. The 0-th order are QPM-like processes. Higher orders include gluon and quark loops, called *virtual corrections* (see Fig. 2.3).

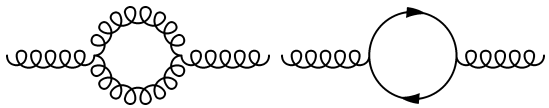

Figure 2.3: One-loop corrections to the gluon propagator.

To calculate cross sections, integration over the full phase space of virtual and real quarks and gluons is needed. This integration introduces divergencies caused by infinite momenta of the virtual particle loops, referred to as *ultraviolet divergencies*. The soft or collinear emission of massless gluons, causes *infrared divergencies*.

To remove these divergencies, first a procedure called *dimensional regularization* introduces additional dimensions ε to the integration. In a second stage, a procedure called *renormalization* replaces divergent integrals by finite expressions. This procedure introduces a new mass μ, the *renormalization scale*. All measurable quantities of the final state particles have to be independent of the choice of the arbitrary scale μ. Thus an effective coupling "constant" $\alpha_s(\mu)$ depends on the scale μ [Eid04]:

$$\mu \frac{\partial \alpha_s(\mu)}{\partial \mu} = 2\beta(\alpha_s). \tag{2.19}$$

The β-function is a perturbative expansion in α_s, covering the dependency of α_s on the scale μ^2:

$$\beta(\alpha_s) = -\frac{\beta_0}{4\pi}\alpha_s^2 - \frac{\beta_1}{8\pi^2}\alpha_s^3 - \dots \tag{2.20}$$

with

$$\begin{aligned} \beta_0 &= 11 - \frac{2}{3}n_f, \\ \beta_1 &= 51 - \frac{19}{3}n_f. \end{aligned}$$

n_f is the number of quark flavors with a mass lighter than the scale μ. The solution of Eq. 2.19 in the first order of α_s is:

$$\alpha_s(\mu) = \frac{12\pi}{(33 - 2n_f)\ln(\mu^2/\Lambda^{n_f}_{\mathrm{QCD}})}. \tag{2.21}$$

$\Lambda^{n_f}_{\mathrm{QCD}}$ is the scale of QCD and represents the energy at which α_s becomes large and perturbative QCD is not longer valid.
Figure 2.4 shows the dependence of α_s on the scale μ. The rise of α_s for small values of μ corresponds to soft interactions and large distances. At large scales $\mu \to \infty$ the value of α_s vanishes and the quarks are quasi-free. In this region of *asymptotic freedom*, perturbative QCD is applicable. The region of soft interactions has to be treated in a different approach.

2.3.4 Factorization

Factorization is the separation of the ep-scattering process into two parts. One part is the hard process, the interaction of high energy particles, the second is the long range part of low energy processes. The hard process is calculable by pQCD. The low energy part is not covered by pQCD. The Structure Function F_2 can be expressed as the convolution

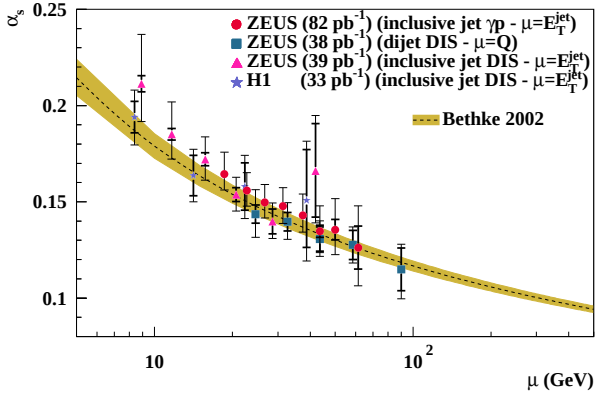

Figure 2.4: Running of α_s with the scale μ measured at HERA. The data are compared with QCD predictions (shaded band) [Gla03].

of a perturbative part, the *coefficient functions* (C_2^i) and the non-perturbative *parton density functions* (PDFs) $f_i(\xi, \mu_f, \mu)$. The PDFs have to be measured experimentally, while the coefficient functions are calculable. The factorization introduces a scale μ_f defining the boundary between the perturbative and the non-perturbative regime. The $f_i(\xi, \mu_f, \mu)$ are the probabilities of finding a parton i with a proton momentum fraction ξ (see Fig. 2.5):

$$F_2 = \sum_{i=parton} \int_x^1 C_2^i \left(\frac{x}{\xi}, \frac{Q^2}{\mu^2}, \frac{\mu_f^2}{\mu^2}, \alpha_s(\mu) \right) f_i(\xi, \mu_f, \mu) d\xi. \tag{2.22}$$

The evolution of the PDFs in μ is described by the Dokshitzer-Gribov-Lipatov-Altarelli-Parisi equations [Alt77] or DGLAP equations. They have the form:

$$\frac{df_{q_i}(x,Q^2)}{d\ln(Q^2)} = \frac{\alpha_s(Q^2)}{2\pi} \int_x^1 \frac{d\xi}{\xi} \left[P_{qq}(x/\xi) f_{q_i}(\xi, Q^2) + P_{qg}(x/\xi) f_g(\xi, Q^2) \right] \tag{2.23}$$

$$\frac{df_g(x,Q^2)}{d\ln(Q^2)} = \frac{\alpha_s(Q^2)}{2\pi} \int_x^1 \sum_i \frac{d\xi}{\xi} \left[P_{gq}(x/\xi) f_{q_i}(\xi, Q^2) + P_{gg}(x/\xi) f_g(\xi, Q^2) \right] \tag{2.24}$$

The functions $P_{ba}(x/\xi)$ are the DGLAP *splitting functions*. They describe the probability of a parton a to emit a gluon or quark and become parton b carrying a fraction $z = x/\xi$ of the momentum of parton a:

$$P_{qg}(z) = \frac{4}{3} \frac{1+z^2}{1-z} \tag{2.25}$$

$$P_{gg}(z) = 6 \frac{(1-z(1-z))2}{z(1-z)} \tag{2.26}$$

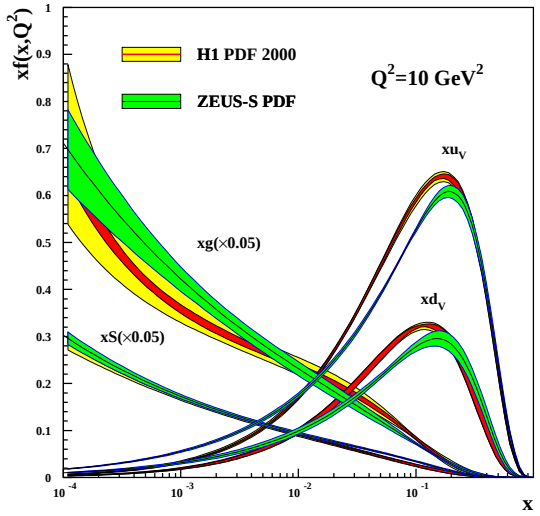

Figure 2.5: Parton density functions [Zeu04] of the valence u and d quark, the gluons and the s quark content of the proton.

$$P_{q\bar{q}}(z) = \frac{1}{2}(z^2 + (1-z)^2) \tag{2.27}$$

The emission of soft gluons causes problems, because P_{qg} and P_{gg} diverge for $z \to 1$. An upper cut-off z_{max} solves this issue.

Although pQCD can predict the evolution of the PDFs from the scale μ_0 to any other scale, a measurement at a particular μ_0 is required to derive values at other scales μ.

As mentioned before, the Structure Functions can be expressed as a power series in α_s. The series contain terms of $\ln \mu^2$ and $\ln(1/x)$. The leading $\ln \mu^2$ term emerges from the evolution along the chain of partons, emitted from the quark before entering the hard interaction with the photon (see Fig. 2.6). By construction, the chain is strongly ordered in transverse momenta, i.e. $\mu^2 \gg k_{t,n}^2 \gg k_{t,n-1}^2 \gg ...$ where k_t denotes the transverse momentum of the parton in the nth position in the ladder. The leading-order (LO) sums up all $\alpha_s \ln \mu^2$ terms. The next-to-leading order (NLO) sums up terms of $\alpha_s(\alpha_s \ln \mu^2)^{n-1}$. This is important, if the construction of a strongly k_t ordered ladder is not an appropriate approach. Problems with this method emerge at very low values of x, due to the $\ln(1/x)$ terms.

A different approach is followed by the Balitsky-Fadin-Kuraev-Lipatov (BFKL)

equation [Kur76]. The $\ln(1/x)$ terms are important in particular in the low x regime. The BFKL equation sums up $\alpha_s(\ln(1/x))^n$, coming from strong ordering in x at leading order (LO).

The attempt of a unification of the DGLAP evolution, based on Q^2 ordering, and the BFKL evolution, based on ordering in x, led to the development of the Ciafaloni-Catani-Fiorani-Marchesini [Cia88] (CCFM) evolution equations.

However so far the measurements show no significant evidence of deviations from the DGLAP equations. Figure 2.7 shows inclusive HERA F_2 data in excellent agreement with with DGLAP-based NLO QCD fits.

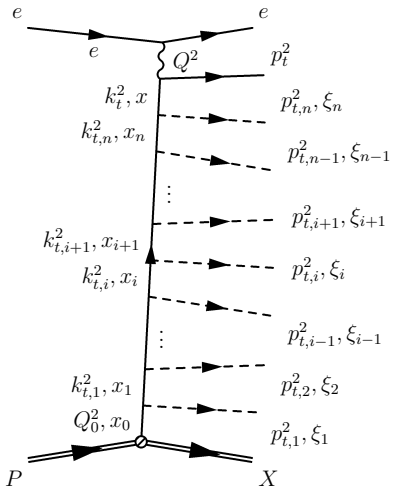

Figure 2.6: Diagram of the k_t-ladder. A quark from the proton interact with a virtual photon from the electron after radiating n partons (dashed lines). Each parton is characterized by a longitudinal momentum fraction x_i and a transverse momentum $k_{t,i}$. Strong ordering corresponds to $Q^2 \gg k_{t,n}^2 \gg k_{t,n-1}^2 \gg ... \gg k_{t,1}^2$.

2.4 Heavy quark production

The production of heavy quarks, like the charm or the beauty quark, can not easily be explained in the naïve picture of the QPM. The mass of the proton is lower than the mass of the heavy quark ($m_c \approx 1.35\,\text{GeV}$ and $m_b \approx 4.4\,\text{GeV}$[3] [Eid04]) and no heavy

[3]estimated in the $\overline{\text{MS}}$ scheme

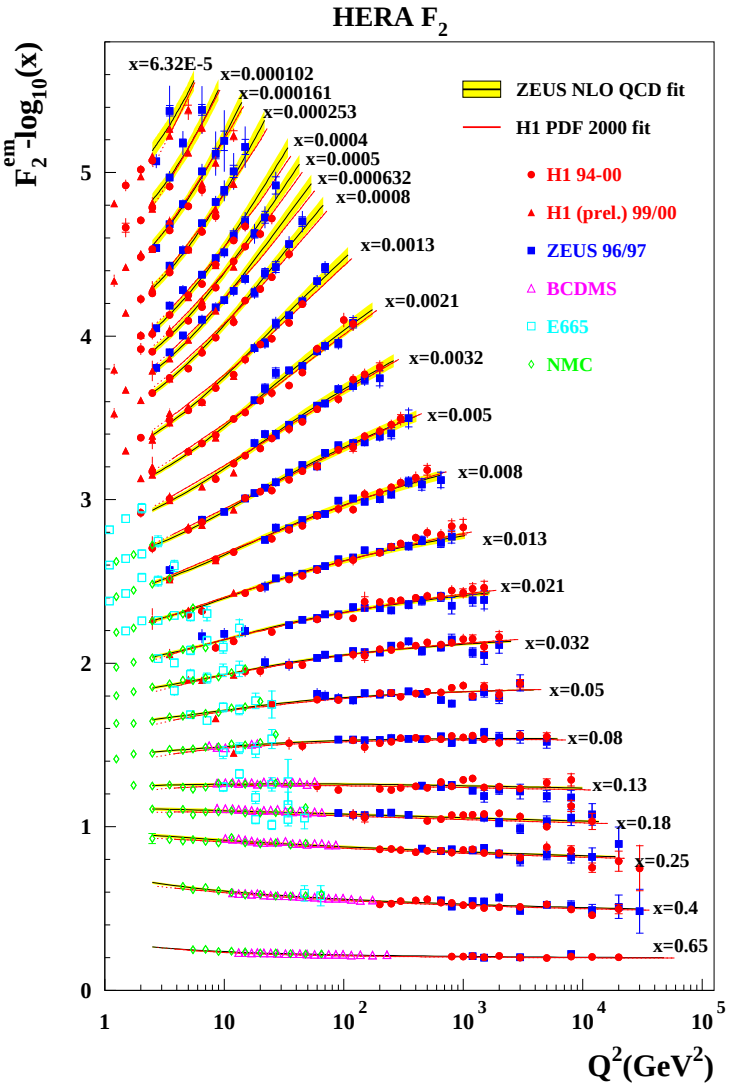

Figure 2.7: Dependence of the proton Structure Function $F_2^{em}(x, Q^2)$ on Q^2 at different values of x measured at HERA and fixed target experiments. While the Structure Function is constant in Q^2 for high values of x, it is rising with Q^2 at lower x values, denoted as *scaling violation*.

quarks on their mass shell can be constituents of the proton. The lowest order process of heavy quark production is the boson-gluon-fusion (BGF) (see Fig. 2.8). This process

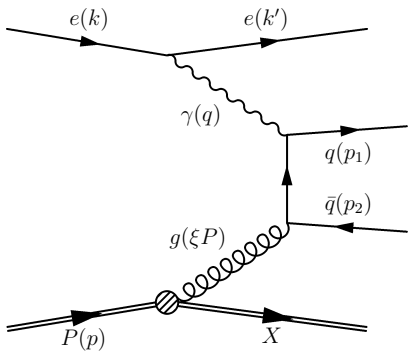

Figure 2.8: Boson-gluon-fusion. At low Q^2 the lowest order mechanism to produce heavy quarks in *ep*-scattering

($\gamma^* g$) can produce a pair of quark and anti-quark if the center-of-mass (CMS) energy squared $\hat{s}$ of the photon-gluon system exceeds the squared mass of the $q\bar{q}$-pair:

$$\hat{s} = (\gamma^* g)^2 = (q + \xi P)^2 > (2m_{q,heavy})^2, \tag{2.28}$$

with the mass of the heavy quark $m_{q,heavy}$ and the four-vectors γ and ξP of the photon and gluon respectively. The high quark mass sets a hard scale for the process and a reliable description by pQCD calculations should be possible, e.g. demonstrated by the low value of the running coupling α_s at a scale corresponding to the beauty quark mass (see Fig. 2.4). Thus the heavy quark production is an excellent test of pQCD. Furthermore heavy flavor measurements provide insights into the gluon contribution of the proton, due to the dominating photon-gluon production process. Two kinematic regions can be distinguished for heavy quark production. In the region of $Q^2 \leq (2m_{q,heavy})^2$, BGF is the lowest order production process of a quark, anti-quark pair of mass $2m_{q,heavy}$. For high $Q^2 \gg (2m_{q,heavy})^2$ the splitting of a gluon into a virtual $q\bar{q}$-pair can be reinterpreted to occur inside the proton and the QPM picture is applicable for the production mechanism.

In Figure 2.9 *ep*-scattering processes up to order α_s are symbolized by Feynman diagrams. The leading order processes in *ep*-scattering are QPM-like events. In addition virtual corrections to this process have to be taken into account. The next process shown is BGF, the dominant process of heavy quark production at low to medium Q^2. The radiation of a gluon before or after the scattering is called QCD *Compton-scattering* (QCDC).

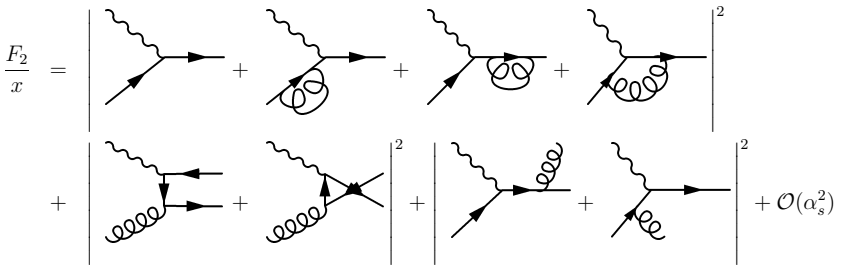

Figure 2.9: Feynman diagrams of processes contributing to F_2 up to $\mathcal{O}(\alpha\alpha_s)$. The diagrams in the upper line are the QPM diagram and virtual corrections. The BGF contribution is shown in the lower left while QCDC graphs are shown on the lower right.

2.4.1 BGF cross sections

The cross section of the production of a heavy $q\bar{q}$-pair in BGF can be calculated [Jon78]:

$$\hat{\sigma}_{\mathrm{BGF}} = \frac{\pi e_b^2 \alpha\alpha_s}{\hat{s}} \left[(2 + 2\omega - \omega^2) \ln \frac{1+\chi}{1-\chi} - 2\chi(1+\chi) \right], \tag{2.29}$$

where e_b denotes the electromagnetic charge of the beauty quark, ω and χ are defined as

$$\omega = \frac{4m_b^2}{\hat{s}}, \quad \chi = \sqrt{1-\omega}. \tag{2.30}$$

In the same way the charm cross section can be calculated using the charm mass and charge respectively. The production of charm is favored with respect to beauty production due to the different charge and mass of b and c quarks. At the energy of the HERA collider, the beauty quark is mainly produced near the mass threshold. In this kinematic region the cross section of beauty quark production is about two orders of magnitude lower than the charm cross section.

2.4.2 Resolved photon process

For low Q^2, the exchanged photon is quasi-real and the probability to fluctuate into a quark, anti-quark pair is significant. The processes where a part of the hadronic structure of the photon interacts with a gluon from the proton are referred to as *resolved processes* (see Fig. 2.10). The strict definition of resolved processes is only possible at LO QCD. At NLO, the definition depends on the technical implementation (see also Fig. 2.14). The point-like process (Fig. 2.10 left) is suppressed by the high mass of the

heavy quark. Hadron-like events (Fig. 2.10 right) contribute significantly to the cross section of beauty production in PHP. In DIS, hadron-like events are suppressed due to the high virtuality of the exchanged photon. As a consequence, resolved processes are not simulated by the MC generator and are neglected in this analysis.

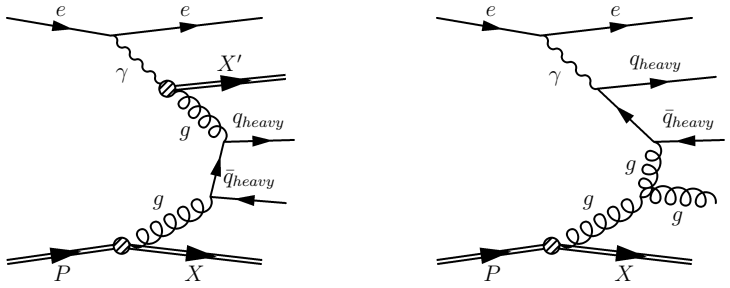

Figure 2.10: Gluon-gluon-fusion in resolved processes. Resolved hadron-like event (left) and point-like (right) in heavy quark production.

2.4.3 Next-to-Leading order processes

Perturbative QCD calculations of heavy quark production are available also in next-to-leading order (NLO). The NLO contributions to the cross section are found to be significant. Feynman graphs of real corrections, emission of gluons, are given in Figure 2.11. In Figure 2.12 virtual corrections, contributing to the interference term with LO, are shown. Two conceptually different calculation approaches can be distinguished

massive scheme : In the massive scheme, only light quarks and gluons are considered as active initial state partons. In the perturbative expansion of the hard scattering cross section $\hat{\sigma}$ all terms up to $\mathcal{O}(\alpha_s^2)$ are taken into account (fixed order approach). This method is reliably applicable in the phase space region where the transverse momentum p_t of the heavy quark is less than or similar to its mass. This scheme is thus particularly relevant for the low Q^2 region.

massless scheme : For $p_t \gg m_q$ (or $Q^2 \gg m_b^2$), large terms proportional to $\ln(p_t^2/m_q^2)$, accounting for collinear gluon emission from a heavy quark and gluon or photon splitting into a heavy $q\bar{q}$-pair, might spoil the convergence of the perturbation series. In so called *resummed calculations*, these contributions are included also beyond $\mathcal{O}(\alpha_s^2)$. Technically, this can be achieved by absorbing the heavy quark associated collinear singularities into fragmentation functions and PDFs. As this requires to set the quark mass to zero, this approach is denoted *massless scheme*.

In contrast to the massive scheme, where the heavy flavors can only be produced dynamically in the hard subprocess, the massless approach treats the heavy quarks as intrinsic photon and proton constituents, which can appear in the final state through heavy quark excitation processes.

For the kinematic range relevant for this analysis, the massive scheme is considered the appropriate method. The production cross section decreases rapidly with increasing p_t and only minor contributions from the regions $p_t \gg m_b$ or $Q^2 \gg (2m_b)^2$ are expected.

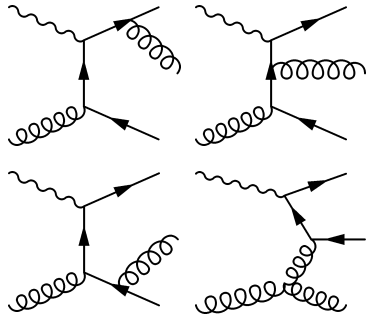

Figure 2.11: Real NLO QCD contributions to heavy quark production

2.5 Hadronization

As a consequence of the color confinement in QCD, the colored partons have to form colorless hadrons. The transformation of strongly interacting particles to hadrons is referred to as *hadronization* or *fragmentation*. The usual approach is to use *event generators* to model this process explicitly. The fixed order hard subprocess is calculated using QCD. The radiation of additional partons before and after the hard subprocess is perturbatively calculable (see Fig. 2.13). The production of hadrons from these *parton showers* has to be treated in a non-perturbative step using phenomenological *hadronization models*. Both stages are described in the following sections.

2.5.1 Parton shower

The parton shower (PS) approach models the evolution equation as a sequence of particle branchings $a \to bc$. The probability that one of these branchings occurs depends on the corresponding splitting function and the virtuality of the initial and final state partons.

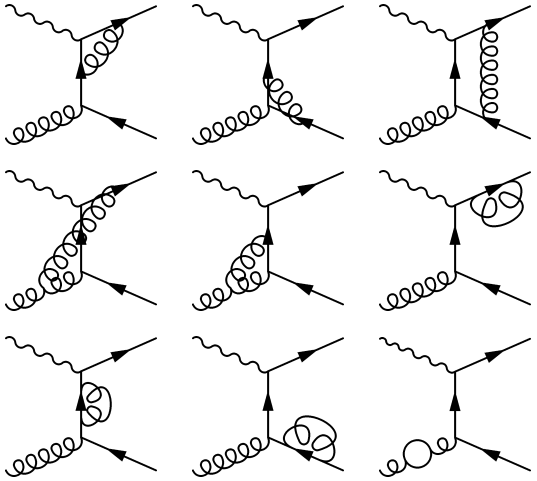

Figure 2.12: Virtual NLO QCD contributions to heavy quark production

The parton shower algorithm starts from a parton of the proton and models the radiation of space-like parton showers until the parton reaches the hard subprocess. The Q^2 of radiated partons is ordered, going towards lower values. Any parton with positive virtuality can be the starting point of a time-like shower. Showers before the photon vertex and after the vertex are separated, neglecting any interference. The branching sequence is stopped when the virtuality of the outgoing partons reaches a cut-off value. Usually this cut-off is chosen to be $1\,\mathrm{GeV}^2$. Below this value pQCD becomes unreliable.

A distinct assignment of a process to LO plus parton shower or NLO is not always possible. As shown in Figure 2.14, the LO plus PS model simulates higher order processes, for instance NLO, in the parton showering.

2.5.2 Hadronization models

The hadronization models are phenomenological models to describe the formation of hadrons from partons. The two main hadronization models used in event generators are the *independent fragmentation* and the *string model*.

Independent fragmentation: The partons from the parton cascade fragment in this model independently. Each parton i transforms to a hadron h carrying a fraction of the longitudinal momentum z of the parton, characterized by *fragmentation*

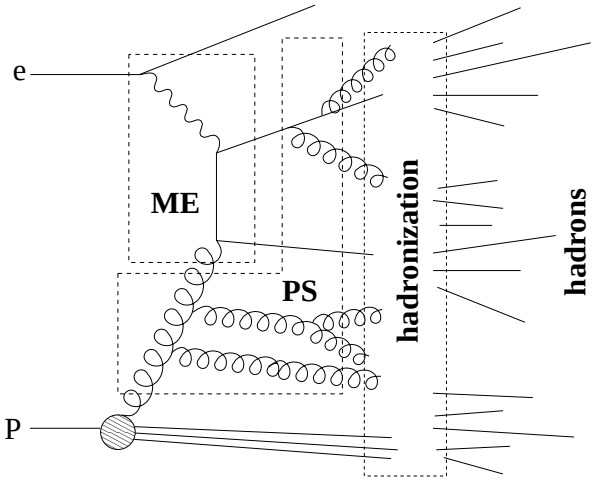

Figure 2.13: Elements of the hadronization process as they are simulated in some Monte Carlo generators. The matrix element (ME), the parton showering (PS) and the hadronization are sketched.

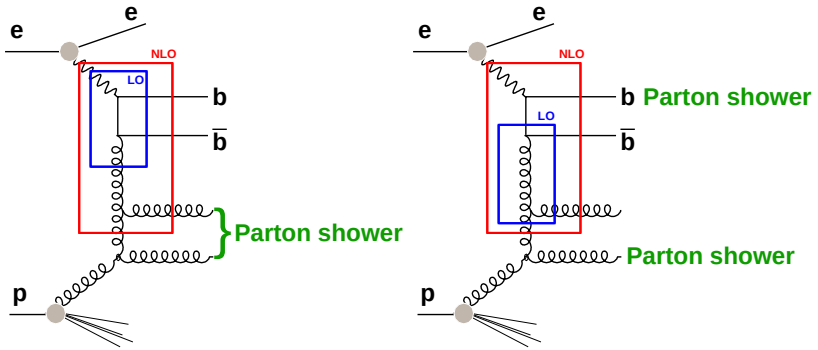

Figure 2.14: LO, NLO and PS in heavy quark production. A part of the parton shower applied to initial and final state partons in LO plus PS is part of the hard scatter in NLO [Blo05b].

functions $D_i^h(z)$. The transverse momentum of the hadrons is assumed to be distributed Gaussian around the parton momentum. The additional quarks and anti-quarks needed to form the hadron are produced as $q\bar{q}$-pairs until the available

energy is spent (see Fig. 2.15, left).

String fragmentation: In the string model the color dipoles of $q\bar{q}$-pairs form *color strings*. As the partons get separated, the string is pulled apart until the energy stored in the string is sufficient to produce a quark/anti-quark pair (see Fig. 2.15, right). The energy in the string rises proportional to the distance of the $q\bar{q}$-pair. This process goes on until the string energy is too low to form additional particles. The string fragments are combined into hadrons using fragmentation functions $D_i^h(z)$.

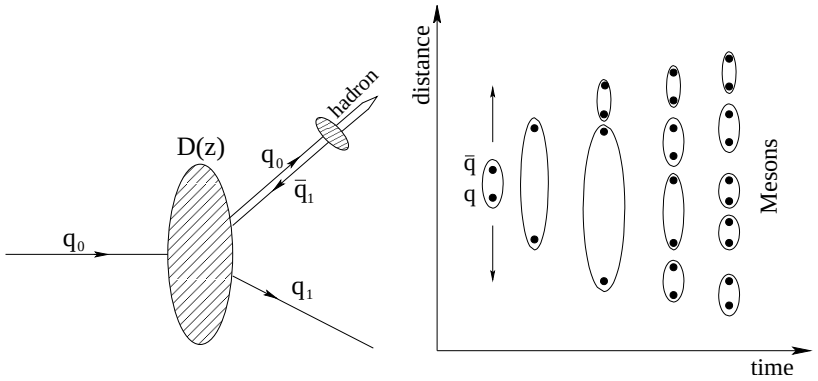

Figure 2.15: Parton fragmentation models: independent fragmentation (left) and the string model (right).

A widely used fragmentation function is the *Peterson fragmentation* [Pet83]:

$$\mathcal{D}_q^h(z) \propto \frac{1/z}{(1 - 1/z - \epsilon/(1-z)^2)}. \tag{2.31}$$

ϵ has to be determined by measurements, while the value of ϵ depends on the treatment of parton showering. For beauty quark production ϵ has been extracted from a fit of B mesons in e^+e^- collisions [Bus95] to be $\epsilon = 0.0033$. For charm fragmentation the ϵ is significantly higher at $\epsilon = 0.040$. Thus the fragmentation function for charm peaks at lower values of z, i.e. the fragmentation of beauty quarks is *harder* (see Fig. 2.16).

The *Lund string model*, used in this analysis, combines the string fragmentation with the *Lund fragmentation function* [And83].

2.5.3 Jets

According to the hadronization, each strongly interacting final state parton from the hard subprocess results in a group of outgoing hadrons. In high-energy processes, where

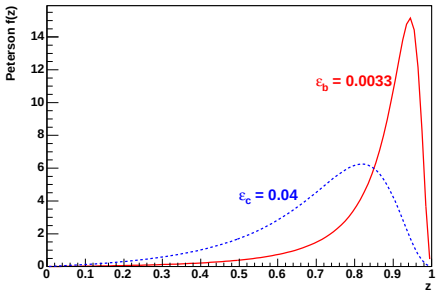

Figure 2.16: Shapes of the Peterson fragmentation functions for charm (dotted line) and beauty (solid line) quarks. The beauty fragmentation function peaks at higher values of z.

the momentum of the original parton is sufficiently high, these hadrons form a collimated flow of particles, called *jet*. Each jet is usually geometrical well separated from the other final state particles.

A strict correspondence of partons to jets is in general spoiled by higher order QCD processes and fragmentation connecting also particles originating from different partons. Nevertheless the jet topology is expected to reflect important properties of the underlying partonic process. In order to exploit this feature using observables based on jets, it is necessary to have a well defined procedure to group final state particles into jets. Furthermore, a rule has to be given to construct a jet momentum from the corresponding set of particle momenta, called *recombination scheme*.

Jets are not considered fundamental QCD objects and the jet structure depends on the reconstruction method used. To be able to compare jet observables with pQCD predictions, some theoretical aspects have to be considered. Results based on jet variables should be *collinear* and *infrared safe*, i.e. safe against collinear radiation or emittance of soft partons. The jet topology should be closely correlated to the partonic final state and *hadronization corrections*, connecting observables on hadron level with the corresponding parton level quantities, are preferred to be small.
The coefficient functions C_2^i, introduced by factorization (see Sec. 2.3.4), depend on Bjørken x and the momentum fraction ξ of the parton involved in the hard interaction only via the ratio x/ξ. Thus they are calculable at parton level without reference to the incoming hadron momentum. The jet algorithm should not destroy this dependency.

The algorithm used in this analysis, the k_t-algorithm [Cat92] meets these requirements. The jet algorithm is Lorentz invariant, so it is possible to use not only the laboratory frame but the *Breit frame* to combine particles to jets.

Breit frame jets

In QPM processes the incoming quark collides with the virtual boson. The Breit frame is defined as the frame where the incoming quark arrives from $-z$ on the z-axis and is scattered back anti-parallel without transverse momentum. The direction of the incoming proton is taken as the z-axis of the Breit frame. In this convention the four-momentum of the exchanged boson (i.e. the photon) is

$$q = (0, 0, 0, -Q). \tag{2.32}$$

Figure 2.17 shows the QPM, QCDC and BGF processes in the Breit frame. The four-momenta of the incoming and scattered quark, p and p' respectively, are

$$p = (Q/2, 0, 0, Q/2) \tag{2.33}$$
$$p' = (Q/2, 0, 0, -Q/2). \tag{2.34}$$

The quark reflects back from the photon, as if the photon were a "brick wall". Events originating from BGF or QCDC produce particles with non-zero transverse momenta in the Breit frame. In principle, this gives a handle to distinguish between QPM events and BGF events, at low Q^2 the lowest order process for beauty production in DIS. Events with transverse momentum in the Breit frame can only be produced by strong interaction. In the laboratory frame, in contrast, events with particles of high transverse momentum can originate from the balancing of the DIS electron and are not necessarily related to heavy quark production. At very high values of Q^2, the heavy quark production can also be interpreted as QPM-events (see Sec. 2.4) and the benefit of the Breit frame measurement vanishes. In addition, the measurement of F_2 requires the measurement of QPM-like processes and is thus not possible using jets in the Breit frame.

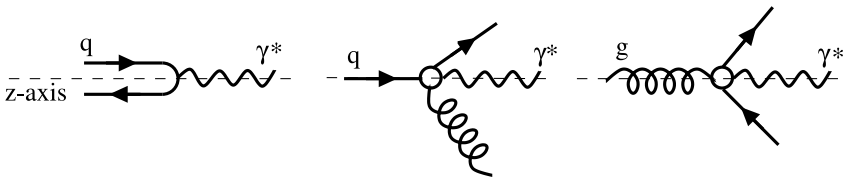

Figure 2.17: QPM, QCDC and BGF events in the Breit frame [Chi03]

2.6 Beauty hadrons

Since beauty quarks produced in the hard interaction fragment to beauty hadrons, the properties of these hadrons are outlined in this section. This analysis is restricted to

semi-leptonic decays of *open beauty* mesons. The term *open* denotes, that particles with the beauty flavor quantum number $B \neq 0$ are produced. While the decay of hidden beauty mesons ($\Upsilon = b\bar{b}$) is suppressed by the OZI-Rule [Zwe64, Oku77], the open beauty mesons ($B^{\pm}$, B^0) and baryons (Λ_b^0) decay with a lifetime of $\sim 1 \cdot 10^{-12}$ s (see Tab. 2.4). The lifetime is relatively long for a decay via the weak force. It is about a factor of three higher than the typical life time of a c meson, e.g. D^0. The element of the CKM (Cabbibo-Kobayashi-Maskawa) matrix $|V_{cb}|$ is responsible for the decay of $b \to cW^-$. Its value is about 25 times lower than $|V_{cs}|$, relevant for $c \to sW^+$:

$$|V_{cb}| = 0.039 \text{ to } 0.044 \tag{2.35}$$
$$|V_{cs}| = 0.9730 \text{ to } 0.9744 \tag{2.36}$$

On the other hand, the Lorentz-boost of the lighter charm meson is higher for a given CMS energy and the decay length in the laboratory system is therefore not necessarily shorter than the decay length of beauty mesons. The higher beauty quark mass results in larger decay angle and this leads to a higher significance for the discrimination between the decay and the production vertex. This gives a handle to distinguish decays of charm and beauty mesons on a statistical basis using *impact parameters* or *secondary vertices* (see Sec. 5.13).

hadron	quark content	mass/ MeV	$c\tau/\,\mu$m
B^+/B^-	$u\bar{b}/\bar{u}b$	5279.0 ± 0.5	501
$B^0/\overline{B^0}$	$d\bar{b}/\bar{d}b$	5279.4 ± 0.5	460
$B_s^0/\overline{B_s^0}$	$s\bar{b}/\bar{s}b$	5369.6 ± 2.4	438
$\Lambda_b^0/\overline{\Lambda_b^0}$	$udb/\overline{udb}$	5624 ± 9	368
D^+/D^-	$c\bar{d}/\bar{c}d$	1869.4 ± 0.5	312
$D^0/\overline{D^0}$	$c\bar{u}/\bar{c}u$	1864.6 ± 0.5	124

Table 2.4: Beauty and charmed hadrons [Eid04]

2.6.1 Semi-leptonic beauty quark decay

The semi-leptonic decay of beauty hadrons into muons is a process with a clean experimental signature. The large mass of the b quark compared to the second quark in the meson (mainly u or d) allows the description by the *spectator model* [Isg89]. In this model, the light quark does not affect the decay process of the heavy quark (see Fig. 2.18).

The b quark most likely decays into cW. If the W produces a pair of leptons $l\nu$, the process is denoted as *semi-leptonic decay* of the beauty quark. The W can also decay into a pair of quarks. The c quark decays further into an s quark and a W. The W, again could materialize into lepton and neutrino. The branching ratio of the direct semi-leptonic decay $B \to \mu\ X$ is about 10.6% [LEP01]. About 8% of all B,

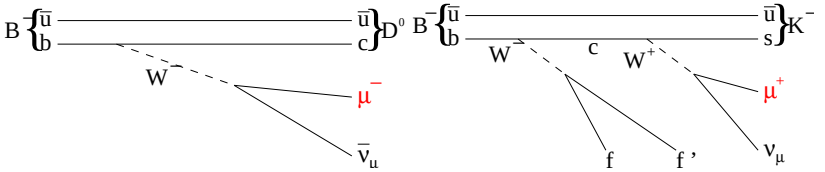

Figure 2.18: Examples of B decay in the spectator model. The prompt decay on the left and the charm cascade on the right.

produce a muon from a charm quark in the indirect decay ($B \to cX \to \mu\nu_\mu sX$) and 2% produce a muon from anti-charm quarks. Other decay modes of beauty quarks, e.g. $B \to J/\Psi\ X \to \mu\mu\ X$ or $B \to \tau\ X \to \mu\ X'$, are much smaller. The spectrum of direct semi-leptonic beauty decay and cascade decay via the charm quark is shown in Figure 2.19. A comparison of lepton momenta from semi-leptonic B hadron decays

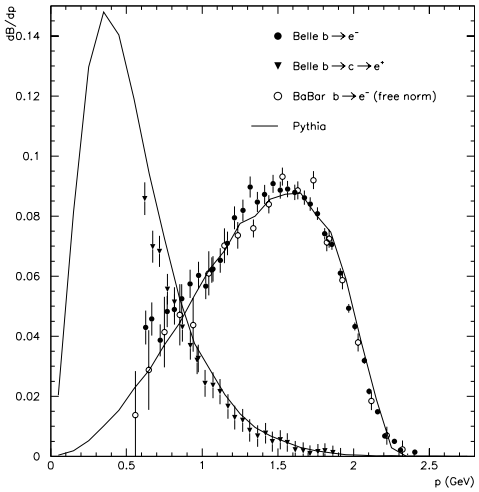

Figure 2.19: Differential branching ratio dB/dp for the electron momentum in the B hadron CMS system as measured by the Belle Experiment for direct (circles) and cascade (triangles) B-meson decays compared to PYTHIA MC prediction (line) [Abe02]. The momentum distribution of the BaBar Experiment is shown with arbitrary normalization (open circles) [Aub03].

is shown in Figure 2.20 for different B hadron admixtures. The spectrum of decay

electrons at the $\Upsilon(4s)$ resonance ($B^\pm/B^0$) is compared with the muon spectrum from B hadrons in another admixture ($B^\pm/B^0/B_s^0/b-$baryon) at higher energies. Even though the B composition is different for these measurements, the momentum spectra of decay leptons are similar. In addition, the results show the lepton universality at energies where the mass difference between electron and muon is negligible. Thus, for muons from b decay at HERA, the same distribution can be expected.

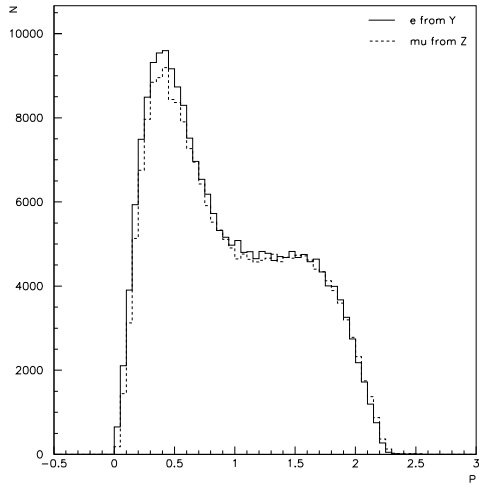

Figure 2.20: MC prediction for the momentum distribution of semi-leptonic decay electrons from B hadrons at the $\Upsilon(4s)$ resonance (BaBar/Belle CMS energies) compared with the momentum spectrum of muon from semi-leptonic decays of B hadrons at LEP CMS energies.

Chapter 3

Measurement of beauty production

Different experiments measured the production of beauty quarks in a wide range of center-of-mass energies. From fixed target experiments (E789 [Jan95], E771 [Ale99] or HERA-B [Abt03]) to $p\bar{p}$-collider experiments (UA1 [Alb91], CDF [Aco02] and D0 [Aba95]), e^+e^--collider experiments (DELPHI, OPAL and L3 [Ach05]) and ep-collider experiments (H1 [Akt05, Akt05b] and ZEUS [Bre00, Che04b, Che04a, Gut05]).
Only the measurements, most relevant for this analysis are reviewed in the following. The selection of results is restricted to beauty quark identification techniques closely related to this thesis. While the center-of-mass energy for the UA1 results is compatible with HERA energies, CDF and D0 are measuring at higher energies. The presented results from ZEUS and H1 are closely related to this analysis. Emphasis is placed in particular on results of the beauty in DIS at ZEUS measurement, because these results are directly comparable to results of a similar measurement presented in this thesis.

3.1 Beauty production at $Sp\bar{p}S$

The UA1 experiment at the $Sp\bar{p}S$ collider at CERN, measured the beauty quark cross section in single and dimuon events [Alb94]. The events were produced in $p\bar{p}$-collisions at a center-of-mass energy of $\sqrt{s} = 630\,\text{GeV}$. Muons were selected, requiring a transverse momentum of at least $p_t^\mu > 6\,\text{GeV}$ for single muons and $p_t^\mu > 3\,\text{GeV}$ for dimuons. In addition a dimuon mass cut of $m_{\mu\mu} < 35\,\text{GeV}$ was applied. To identify beauty events, the p_t^{rel} (explained in Sec. 5.11) method was used and the cross sections were measured in a rapidity range $|y_b| < 1.5$.
All measured beauty quark cross section, shown in Figure 3.1, are in good agreement with NLO QCD predictions [Nas88].

Furthermore the correlation between both b quarks was measured. The configuration in the $b\bar{b}$ center-of-mass system is back-to-back for leading order processes. For events produced by higher order processes ($\Delta\varphi_{b\bar{b}} < 120°$) the quantity $\Delta R_{b\bar{b}} = \sqrt{\Delta\eta_{b\bar{b}}^2 + \Delta\varphi_{b\bar{b}}^2}$ is calculated (see Fig. 3.2). The description of the shape of data distributions by the NLO QCD calculation is quite good, even at lower $\Delta\varphi_{b\bar{b}}$, showing the validity of the

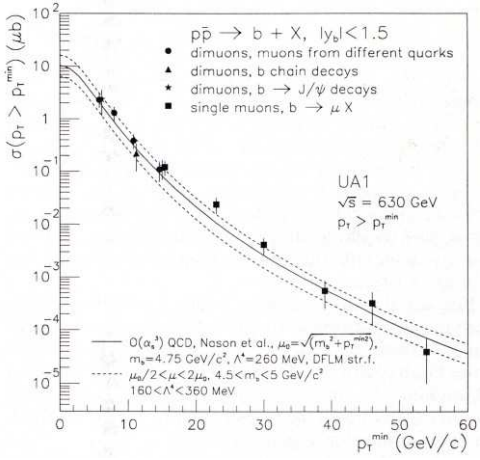

Figure 3.1: Inclusive single beauty quark cross section for $|\eta| < 1.5$ from UA1. Shown are cross sections extracted from single muon events and dimuon events originating from different beauty quarks and from beauty chain decays. Also measurements extracted from single muon events originating from J/Ψ from beauty quarks and a comparison to NLO QCD calculation are shown [Nas88].

higher order contributions to QCD calculations. The normalization differences between data and NLO are within the theoretical errors.

3.2 Beauty production at Tevatron

The experiments D0 [Aba95] and CDF [Abe96] at the Tevatron $p\bar{p}$-accelerator, are measuring beauty production at higher energies. In the first running period from 1992 to 1995 (RUN Ia and Ib) the center-of-mass energy $\sqrt{s}$ was 1.8 TeV, since 2001 (RUN IIa) the energy has been increased to 1.96 TeV.
Early cross section measurements at CDF are shown in Figure 3.3 (left). The CDF collaboration reported compatibility of the NLO QCD shape, but a normalization difference of a factor ~ 2. The D0 collaboration showed good agreement of NLO calculations to data (Fig. 3.3 right).
Further measurements of the D0 collaboration [Abb00] showed a similar normalization problem as the CDF results. The calculation was a factor of ~ 3 lower than the data.

The differential cross section measurement $d\sigma/d\Delta\varphi_{\mu\mu}$ at D0 (see Fig. 3.4) is well described by NLO calculations of the program HVQJET.

After recent improvements of the experiments and the theoretical calculations, data

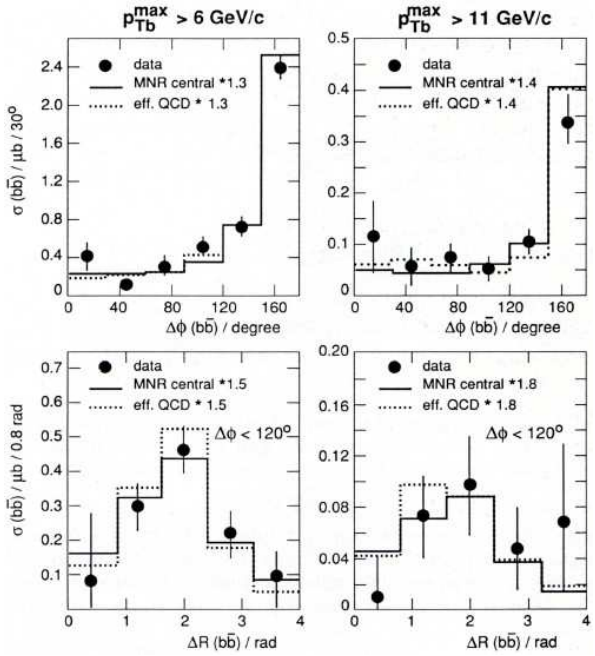

Figure 3.2: Higher order contributions to $\sigma_{b\bar{b}}$ for $\Delta\varphi_{b\bar{b}}$. For higher order processes the $\Delta R_{b\bar{b}}$ is shown in two different regions of transverse momentum of the highest beauty quark: $p_{tb}^{max} > 6\,\mathrm{GeV}$ (left) and $p_{tb}^{max} > 11\,\mathrm{GeV}$ (right) [Nas88].

and NLO calculations are in good agreement [Aco05]. In Figure 3.5 the CDF results of RUN I and preliminary results of RUN II data are compared to refined NLO calculations, including resummation of logarithmic corrections for all perturbative orders and proper treatment of hadronization/fragmentation. The normalization discrepancy seems to be solved by these improved NLO calculations.

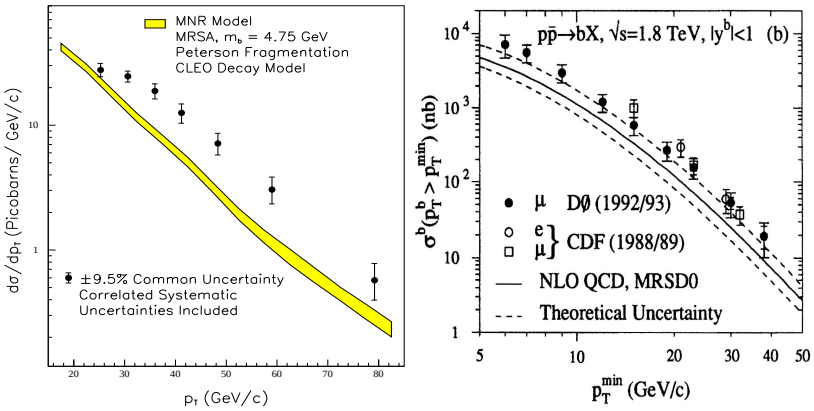

Figure 3.3: Left: Differential beauty quark cross section from CDF as a function of p_t^b. The shape of the cross section for $p_t^\mu > 9\,\mathrm{GeV}$, $|\eta^\mu| < 0.6$ and $|\eta^b| < 1.5$ is compared to NLO QCD calculations. Right: beauty quark cross section from D0 as a function of p_t^b using the p_t^{rel} method for $|y^b| < 1.0$ compared to NLO calculations.

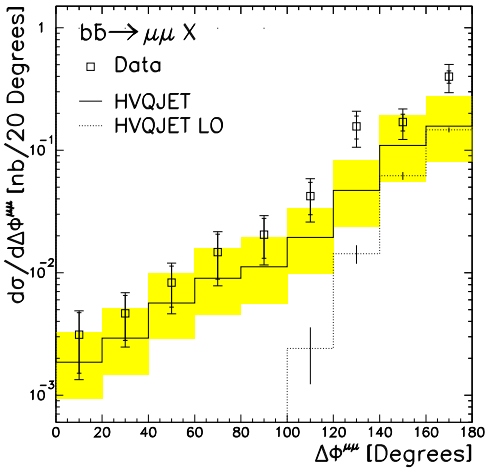

Figure 3.4: Beauty quark cross section as a function of $\Delta\varphi^{\mu\mu}$ for $|y_b < 1.0|$ compared to NLO calculations.

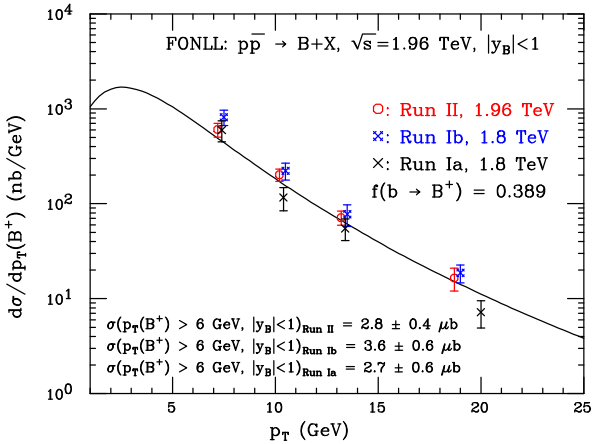

Figure 3.5: Beauty cross sections at CDF for RUN Ia, Ib and II compared to improved NLO predictions.

3.3 Beauty production at HERA

The production of beauty quarks in ep-collisions at HERA is studied at the experiments H1 [Abt97] and ZEUS [Hol93]. Different measurements in the DIS and photoproduction regime have been performed, here only the beauty identification by the semi-leptonic decay into a muon is reviewed.

3.3.1 Beauty in PhP with μ+jet

H1 has measured differential cross sections in events with a muon and 2 jets [Akt05] in the photoproduction regime for $Q^2 < 1\,\mathrm{GeV}^2$ using an integrated luminosity of $50\,\mathrm{pb}^{-1}$. The determination of the beauty fraction used a simultaneous p_t^{rel} and impact parameter fit (for definitions of p_t^{rel} and impact parameter, see Sec. 5.11 and 5.13 respectively). Cross sections calculated from this fit are given in Figure 3.6. A similar measurement at ZEUS [Che03] used the p_t^{rel} method only. The η range of the muon was wider ($|\eta^\mu| < 2.5$) than at H1 and the data points are not directly comparable between ZEUS and H1. The comparison of differential cross sections in p_t^μ and η^μ with the massive NLO QCD prediction (FMNR) is shown in Figure 3.6. A correction factor from LO+PS MC simulations has been applied to the NLO QCD calculations at parton level, to describe the measured hadron level properties. The agreement of the NLO prediction with data is reasonable, but the p_t^μ spectrum of H1 data seems to be softer than the prediction and at low p_t^μ the NLO QCD calculation is more than two standard deviations below

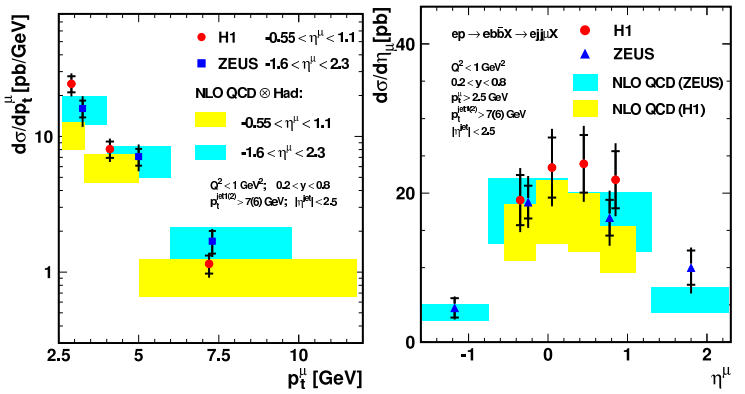

Figure 3.6: Differential cross sections in p_t^μ and η^μ of muons from beauty events in PHP as measured by H1 and ZEUS compared to NLO QCD predictions [Blo05]. Due the different η range, H1 and ZEUS data are shown with separate NLO QCD calculations.

the data of H1.

3.3.2 Beauty in DIS in μ+jet at H1

In the DIS regime, similar measurements were performed. The kinematic region of the H1 measurements is given as:

- $2\,\mathrm{GeV}^2 < Q^2 < 100\,\mathrm{GeV}^2$
- $p_t^\mu > 2.5\,\mathrm{GeV}$
- $-0.75 < \eta^\mu < 1.15$
- $0.1 < y < 0.7$
- $p_{t,Breit}^{jet} > 6\,\mathrm{GeV}$
- $|\eta_{lab}^{jet}| < 2.5$

Differential cross sections in η^μ and p_t^μ are shown in Figure 3.7. The data are well described by NLO calculations at low η^μ, but at higher pseudo-rapidity, the data are above the prediction. The p_t^μ spectrum is slightly steeper than the prediction.

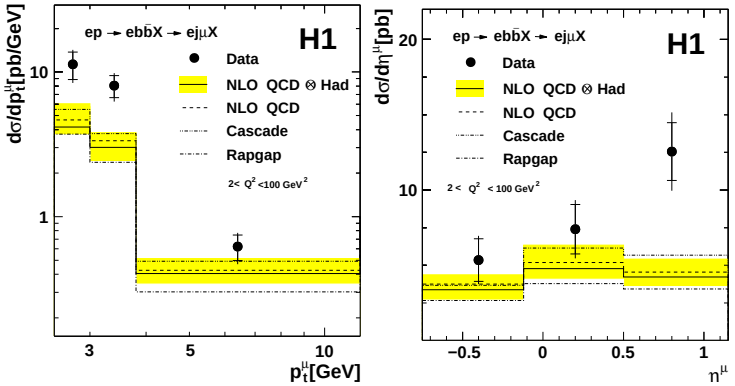

Figure 3.7: Differential cross sections in p_t^μ (left) and η^μ (right) of muons from beauty events in DIS, measured by H1 [Akt05].

3.3.3 Inclusive measurements using impact parameters

In addition to the measurement of muons from beauty, H1 performed an inclusive lifetime measurement [Akt05b] of all tracks of an DIS event with high $p_t > 0.5\,\text{GeV}$ and precise vertex tracker information. For these tracks the significance of the impact parameter $S_{1,2,3} = \delta_{1,2,3}/\sigma_{\delta_{1,2,3}}$ was calculated for the track with the largest, second largest and third largest impact parameter δ (with $|\delta| < 0.1\,\text{cm}$). For events containing a jet, the sign of the impact parameter was determined relative to the jet, for other events, the sign was chosen relative the hadronic final state. This method yields high statistics and a good separation of beauty from charm and light flavor processes (see Fig. 3.8).

Beauty contribution to F_2

To determine the beauty contribution to the proton structure function F_2, this method was used to measure double differential beauty cross sections in bins of x and Q^2. The resulting $F_2^{b\bar{b}}$ is shown in Figure 3.9. Good agreement with both the H1 PDF 2000 fit [Adl03] and MRST03 [Mar04] was found (see Tab. 3.1).

The integrated beauty cross section for $Q^2 > 150\,\text{GeV}^2$ and $0.1 < y < 0.7$ has been determined at H1 to be $\sigma^{b\bar{b}}(e\,p \to e\,b\bar{b}\,X) = 55.4 \pm 8.7(\text{stat.}) \pm 12(\text{syst.})\,\text{pb}$. As shown in Table 3.1, this result agrees with NLO QCD predictions in the massless scheme, but is also compatible within errors with calculations in the massive scheme.

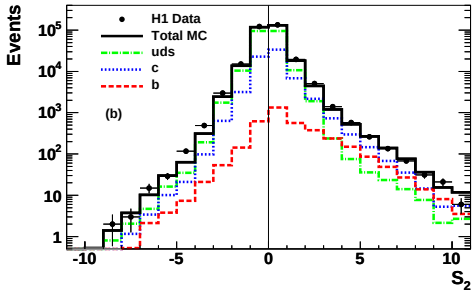

Figure 3.8: Significance distribution $\delta/\sigma(\delta)$ of the track with the second highest absolute significance at H1. Shown is the light flavor MC from DJANGOH and RAPGAP MC for b and c quarks. The contributions from the various quark flavors are shown after applying the scale factors obtained from a fit to the subtracted significance distributions of the data [Akt05b].

Source	Cross section
H1 measurement	$\sigma^{b\bar{b}} = 55.4 \pm 8.7 \pm 12\,\text{pb}$
H1 PDF 2000 (massless scheme)	$\sigma^{b\bar{b}} = 52\,\text{pb}$
NLO (massive⊗massless scheme)	$\sigma^{b\bar{b}} = 47\,\text{pb}$
NLO (massive scheme)	$\sigma^{b\bar{b}} = 37\,\text{pb}$

Table 3.1: Comparison of measured and calculated $b\bar{b}$ cross sections at H1

3.3.4 Beauty in DIS at ZEUS

The direct predecessor of this analysis is an analysis of beauty in DIS for ZEUS data from 1999 to 2000, corresponding to a luminosity of $72.4\,\text{pb}^{-1}$ [Che04b]. It used events with at least one hard jet in the Breit frame and a muon from a b decay. To extract the beauty fraction, the p_t^{rel} method was used. The measurement was restricted to a limited region of phase space, in which the scattered electron, the muon and the jet are well reconstructed in ZEUS. The muon had to be reconstructed by an algorithm called BREMAT requiring the outer muon chambers and thus was restricted to transverse momentum $p_t^\mu > 2\,\text{GeV}$ in the pseudo-rapidity range $-0.9 < \eta^\mu < 1.3$ or to $p^\mu > 2\,\text{GeV}$ in the region of $-1.6 < \eta^\mu < -0.9$ (for details of muon reconstruction see Sec. 5.7). At least one jet, reconstructed in the Breit frame, with $E_t^{Breit} > 6\,\text{GeV}$ was required, the muon was associated to a jet with $E_t^{Breit} > 4\,\text{GeV}$. After these cuts 941 events remained. The achieved beauty fraction, extracted from a maximum-likelihood p_t^{rel} fit was 30.2% with a statistical error of 4.1%.
The visible cross section in the kinematic region, defined as:

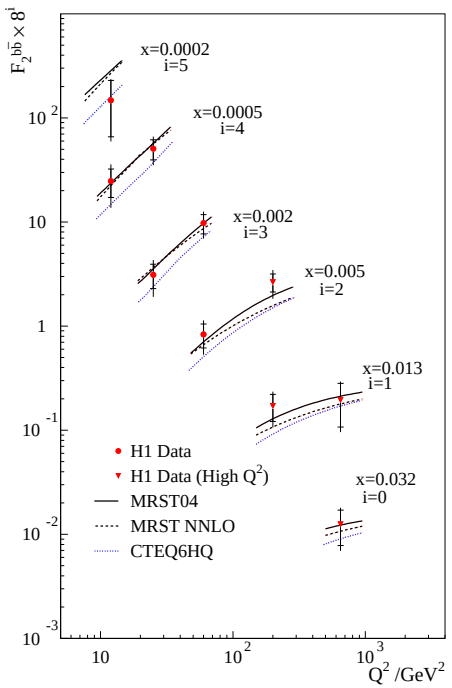

Figure 3.9: The measured $F_2^{b\bar{b}}$ as a function of Q^2 for various x values at H1. Predictions of QCD are also shown [Akt05b].

- $Q^2 > 2\,\mathrm{GeV}^2$
- $0.05 < y < 0.7$
- $-0.9 < \eta^\mu < 1.3$ and $p_t^\mu > 2.0\,\mathrm{GeV}$ or $-1.6 < \eta^\mu < -0.9$ and $p^\mu > 2.0\,\mathrm{GeV}$
- $E_{t,Breit}^{jet} > 6\,\mathrm{GeV}$
- $-2.0 < \eta_{lab}^{jet} < 2.5$

was calculated to be: $\sigma^{b\bar{b}}(e\,p \to e\,b\bar{b}\,X \to e\,\mu\,jet\,X') = 40.9 \pm 5.7(\mathrm{stat.})^{+6.0}_{-4.4}(\mathrm{syst.})\,\mathrm{pb}$. The NLO QCD prediction with hadronization corrections is $20.6^{+3.1}_{-2.2}\,\mathrm{pb}$ which is about

2.5 standard deviations lower. The CASCADE MC program predicts $\sigma^{b\bar{b}} = 28\,\mathrm{pb}$ while RAPGAP gives $\sigma^{b\bar{b}} = 14\,\mathrm{pb}$.

The differential cross sections in Q^2 and in $\log_{10}(x)$ compared with NLO predictions and with MC are shown in Figure 3.10. A comparison of differential cross sections in p_t^μ and η^μ is given in Figure 3.11.

The NLO QCD predictions are in general consistent with the data, but at low values of Q^2, Bjørken x, muon p_t and high values of muon η and jet E_t (not shown), the prediction is about two standard deviations below the data. The CASCADE MC gives a good description of the data, but it is below the data at low p_t^μ, low Q^2 and low x. RAPGAP is well below the data for all measured cross sections.

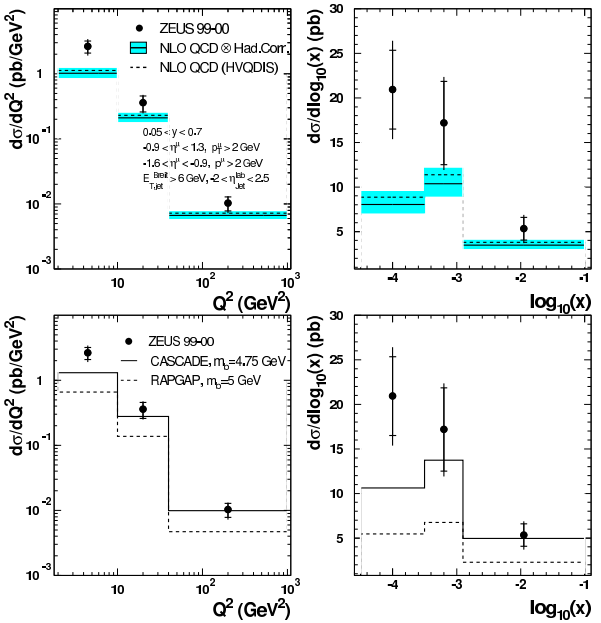

Figure 3.10: Differential beauty cross sections in Q^2 (left) and $\log(x)$ (right) in DIS at ZEUS [Che04b]. A comparison of data with NLO QCD calculations is shown (upper line) and a comparison with the MC programs CASCADE and RAPGAP (lower line).

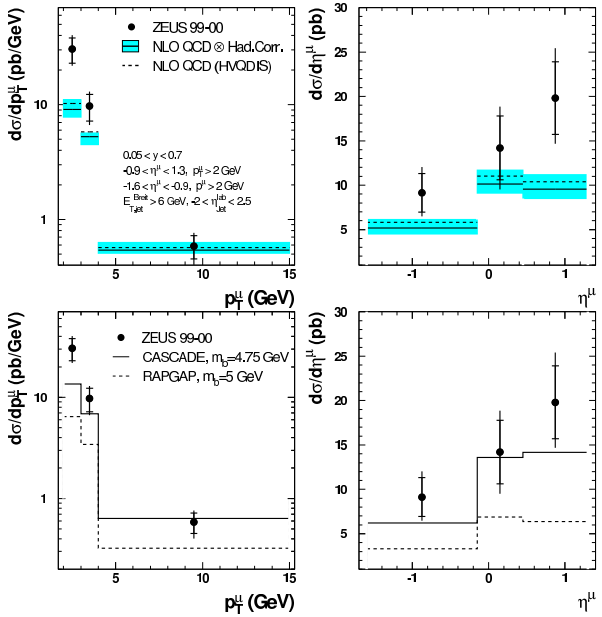

Figure 3.11: Differential cross sections in p_t^μ (left) and η^μ (right) of muons from beauty events in DIS as measured ZEUS [Che04b].

3.4 Conclusions

The beauty quark production measured at $p\bar{p}$-collisions is in good agreement with NLO QCD predictions. At ep-collisions, the NLO QCD predictions for beauty cross sections in general agree with the data, however they are below the data in some regions of phase space (low Q^2, x, p_t^μ, high η^μ and E_t^{jet}). One aim of the analysis described in this thesis is the improvement of measurements in these regions in particular with a direct comparison at low transverse momentum of the muon.

Chapter 4

The ZEUS detector at HERA

This chapter describes briefly the ZEUS detector at HERA. The detector is used to measure beauty production in ep-collisions described by this thesis. The parts of the detector essential for this analysis will be discussed in more detail.

4.1 The HERA ep-collider

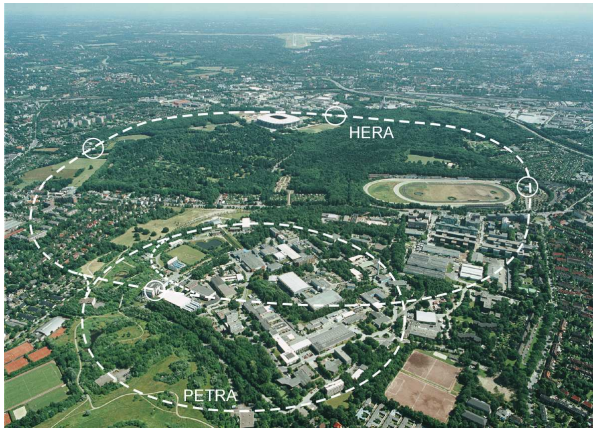

Figure 4.1: Aerial view of the DESY site. The contours of the HERA tunnel and the PETRA pre-accelerator are indicated.

HERA (Hadron Elektron Ring Anlage)[Ham81] is the only lepton proton collider in the world. It accelerates leptons, either electrons or positrons, and protons and brings them to collision in the centers of the experiments H1 and ZEUS. The ring is built in a tunnel of 6.3 km circumference 15−30 m below ground. It is situated at DESY (Deutsches

Elektronen SYnchotron) in Hamburg, Germany. HERA consists of two separate rings to accelerate and store protons and electrons or positrons. The maximum energy of the protons is 920 GeV and that of the electrons/positrons[1] 27.5 GeV.

The leptons are accelerated using normal and superconducting cavities to compensate the energy loss due to synchrotron radiation. The synchrotron emission of the protons is negligible, so only normal conducting cavities are used to accelerate to the nominal energy. To force the particles on orbit normal conducting magnets of a field strength of 0.3 T are used for the lower momentum leptons but superconducting magnets (5 T) are needed for the bending of the higher momentum protons.

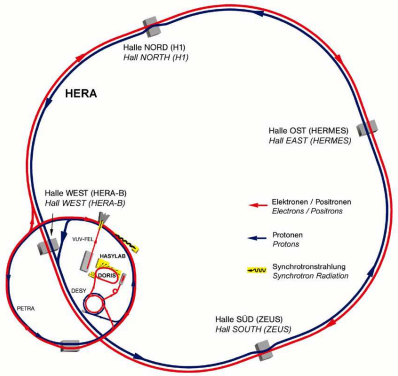

Figure 4.2: The HERA accelerator and pre-accelerators

The particles are brought to collision at zero crossing angle in the north and the south hall, where the two collider experiments H1 and ZEUS are located (see Sec. 4.2). The HERMES experiment in the east hall uses only the electron beam to study the spin structure of the nucleon in a gas target. In the west hall the HERA-B experiment was situated, whose goal was to measure CP-violation in decays of B mesons in fixed target pN-collisions.
HERA can collide electrons as well as positrons with protons. The leptons for different data taking periods of HERA are given in Tab. 4.1.

Built between 1984 and 1990 HERA started operation for physics data 1992. Initially protons were accelerated to 820 GeV and positrons to 27.5 GeV (see Fig. 4.3). In 1998 the proton energy was increased to 920 GeV and instead of positrons electrons were accelerated. The switch back to positrons took place in 1999 and lasted till 2000. The data before the shutdown will be called in the following HERA I data.

HERA was upgraded in a shutdown 2000/2001 to achieve a higher luminosity at the colliding experiments. The specific luminosity increased by a factor of five [Sch98]. In

[1] In the following, unless stated otherwise, the term *electron* is used for both electrons and positrons

Data taking period	leptons	proton energy [GeV]	lepton energy [GeV]	CMS energy [GeV]
HERA I				
1996-1997	e^+	820	27.5	300
1998-1999	e^-	920	27.5	318
1998-2000	e^+	920	27.5	318
HERA II				
2003-2004	e^+	920	27.5	318
2004-2005	e^-	920	27.5	318

Table 4.1: Data taking periods of HERA with the lepton and the energies

addition the electron beam is now longitudinally polarized at both collider experiments. There were severe problems with background from high synchrotron radiation at ZEUS, that were solved in a further shutdown [Bai02]. The physics data taking started again in October 2003. These data will be called HERA II data in the following.

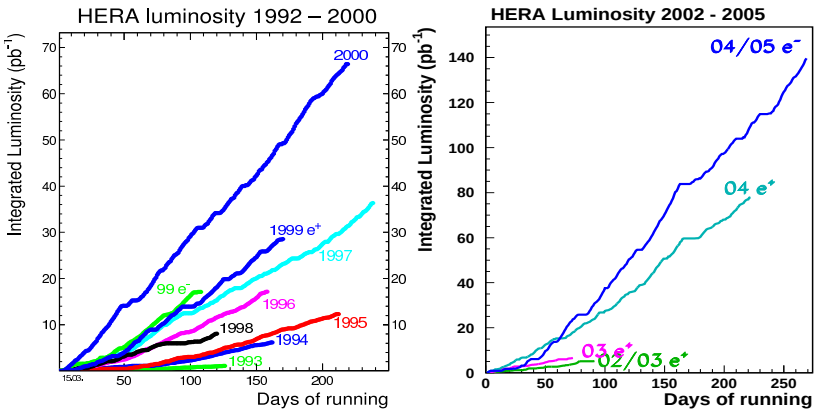

Figure 4.3: The luminosity delivered by HERA for 1992-2000 (HERA I, left) and 2002-2005 (HERA II, right)

4.2 The ZEUS detector

The ZEUS[2] detector is a general purpose detector build to study various aspects of proton electron scattering [Hol93]. The detector has a large asymmetry in the forward-backward[3] direction to accommodate the boost of the center-of-mass system caused by the much higher energy of the proton beam with respect to the electron beam. The ZEUS coordinate system is a Cartesian right-handed system with its origin at the nominal interaction point. The x-axis pointing towards the center of HERA, the y-axis upwards and the z-axis along the flight direction of the proton beam. The polar angle θ and the azimuth angle φ are measured relative to the z- and x-axis respectively.

The main part of the detector has a size of $12\,\mathrm{m}\cdot 10\,\mathrm{m}\cdot 19\,\mathrm{m}$ and a weight of about 3600 tons. A schematic view of ZEUS is shown in Fig. 4.4.

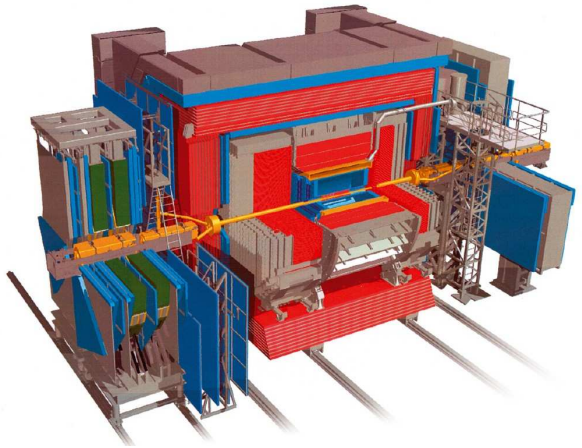

Figure 4.4: Scheme of the ZEUS detector, showing the main components.

In the following the main parts of the detector are mentioned (see Fig. 4.5 and 4.6). The innermost space around the interaction-point (IP) is covered since HERA II by the MVD (see Sec. 4.2.1), a silicon strip micro-vertex-detector. The central tracking detector (CTD, see Sec. 4.2.2), a cylindrical drift chamber, surrounds the beam pipe in the central region (including the MVD). It is enclosed by a super-conducting solenoid, providing a magnetic field of 1.4 T parallel to the beam pipe, allowing to determine the charge and momentum of charged particle tracks. In the forward region the CTD is supplemented

[2] Zeus, the husband of Hera in Greek mythology can also be seen as an acronym in ancient Greek: Ζευς: ζήτησις καθ' εύρετής ὑποκειμένης συμμετρίας = Search to Elucidate Underlying Symmetry [Sax87].

[3] forward refers to the direction of the proton beam

by three sets of planar drift chambers (FTD) with transition radiation detectors (TRD) in between. The rear region is covered by one planar drift chamber consisting of three layers (RTD).

The tracking system is surrounded by a uranium-scintillator calorimeter (CAL, see Sec. 4.2.3) which is the main device for energy measurements. It is divided into forward (FCAL), barrel (BCAL) and rear (RCAL) sections. In the rear region around the beam pipe an additional detector is located to determine the scattered electron position (SRTD, see Sec. 4.2.4). An iron yoke, providing the return path for the magnetic field flux of the solenoid, encloses the CAL. The iron is magnetized to 1.6 T by copper coils and is instrumented with proportional chambers to measure the energy leaking through the uranium-calorimeter and to act as a tracking calorimeter for muon detection. It is referred to as backing calorimeter (BAC, see Sec. 4.2.5). Detectors, dedicated to identify muons (see Sec. 4.2.6) are located inside (FMUI, BMUI and RMUI) and outside (FMUO, BMUO and RMUO) the iron yoke.
The VETOWALL in the rear direction, a detector composed of iron and scintillators, is used to reject proton beam related background.
The LUMI detector (see Sec. 4.2.7) is a small calorimeter, made of lead and scintillators, at $z = -107$ m to detect photons from bremsstrahlung events for the luminosity measurement. There are several other components not used for this analysis and therefore neglected in this list.

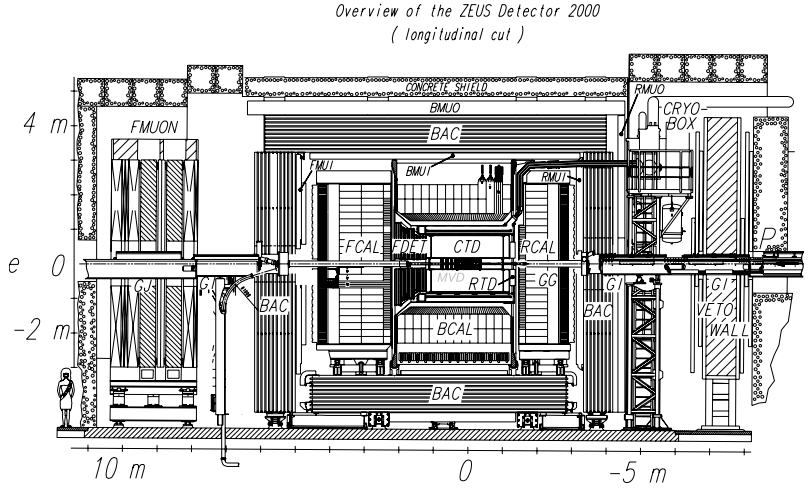

Figure 4.5: Cross section of the ZEUS detector parallel to the beam pipe. For a description of the different detector components see text.

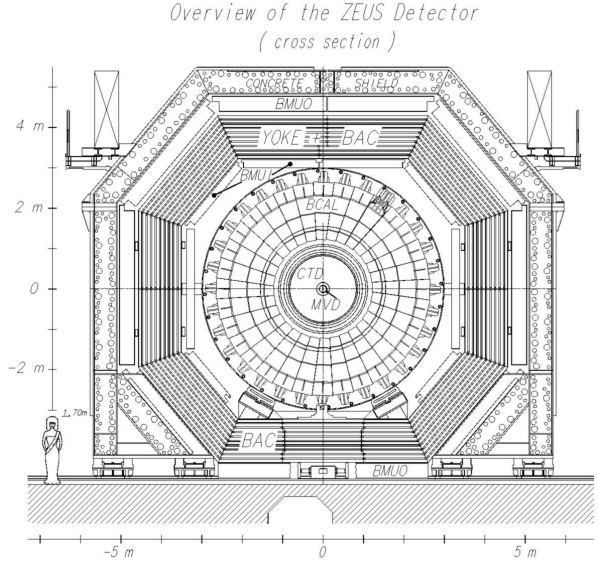

Figure 4.6: Cross section of ZEUS, perpendicular to the beam pipe.

4.2.1 The micro vertex detector MVD

The micro vertex detector MVD [Zeu97] is a silicon-strip vertex detector, installed in ZEUS during the shutdown 2001 to improve the resolution of the tracking system[4]. The main goal is to be able to detect impact parameters with respect to the primary vertex and secondary vertices, originating from heavy meson decays.

Design parameters of the MVD are [Gar99]:

- polar angle coverage of 10° to 150°
- at least three hits per track
- single hit resolution of 20 μm
- two track separation of 200 μm
- hit efficiency better than 95%
- noise occupancy better than 10^{-3}

[4]The former vertex detector VXD was damaged and removed 1994

The MVD consists of two regions, the barrel region 620 mm long, with three layers (cylinder 0,1 and 2) of silicon-strip-detectors, mounted on so called *ladders* parallel to the beam pipe (see Fig. 4.8, left) and the forward region consisting of four *wheels* of 14 wedge shape sensors, mounted perpendicular to the beam pipe (see Fig. 4.8, right). To fit around the elliptical beam pipe, the innermost cylinder is not complete and two detectors in each wheel are shorter.

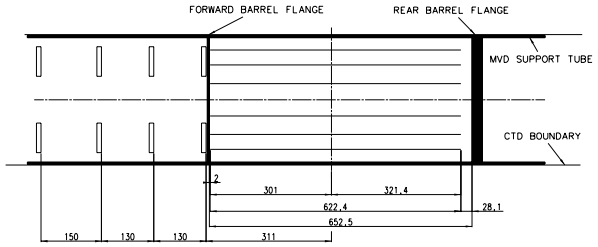

Figure 4.7: Cross section of the MVD, parallel to the beam pipe with the barrel region on the right and the forward region on the left.

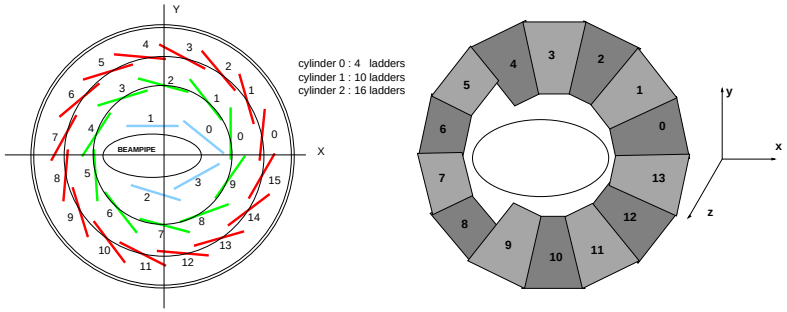

Figure 4.8: Cross section of the MVD, perpendicular to the beam pipe. Barrel region on the left (with three cylinders), forward region on the right (one of the four wheels).

The strip-sensors are made of 300 μm thick n-type silicon (see Fig. 4.9), with p^+ implantations of 12 μm and 14 μm. 512 channels are read out, while the total number of strips is 6 times higher (see Fig. 4.10). Using the *capacitive charge sharing* the readout of one out of six strips allows a good resolution of less than 20 μm despite of the readout pitch of 120 μm. Capacitive charge sharing means, that a charge in one strip couples via the p^+ implementation to each other strip. The n-type silicon acts as a capacity, distributing the signal to the readout strips.

Two strip-sensors of $64.2 \cdot 64.2\,\mathrm{mm}^2$ form a *half module*. A kapton foil with etched copper strips connects the sensors with the controller and readout chips (HELIX 3 chips).

Two adjacent channels (from two sensor strips perpendicular to each other) are read out in one channel. This adds up to 512 channels for each half module. Two half modules, mounted mirror imaged form a *full module*. Due to this type of readout, for one hit two combinations of x and y position are possible. This ambiguity of the readout is resolved at reconstruction level. In the barrel MVD 300 half modules are mounted on 30 ladders, carbon fiber supporting structures, arranged in three cylinders around the beam pipe (see Fig. 4.7, left). The forward MVD consists of 112 half modules mounted in two back-to-back layers on each of the 4 carbon fiber wheels. It covers a pseudo-rapidity up to $\eta = 2.6$ for forward tracks. Overall the MVD provides about 210000 readout channels.

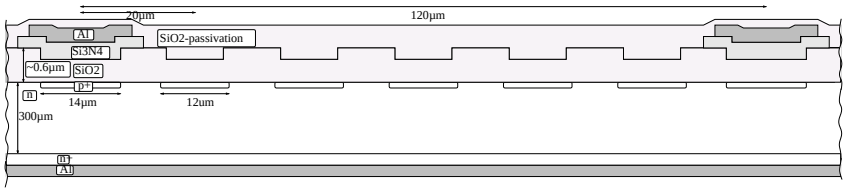

Figure 4.9: Structure of a MVD strip-sensor.

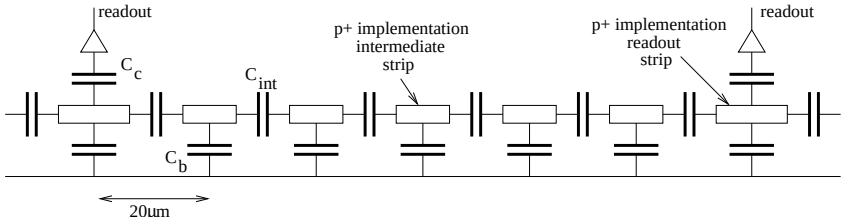

Figure 4.10: Coupling of the MVD strips.

To achieve high precision measurements, the position of the MVD and of each ladder separately has to be known accurately. The external alignment of the MVD with respect to the CTD and the internal alignment of the ladders used cosmic muons and improved the resolution of the hit reconstruction significantly. The impact parameter resolution, quoted in [Koh05], after the alignment is parameterized by:

$$\delta D[\,\mathrm{mm}] = 0.151/p_T \oplus 0.0058. \tag{4.1}$$

4.2.2 The central tracking detector CTD

The central tracking detector (CTD) [Har89] is a cylindrical gas-filled wire chamber. It provides a high precision measurement of the track and transverse momentum of

charged particles. In addition the measurement energy loss dE/dx provides information for particle identification.

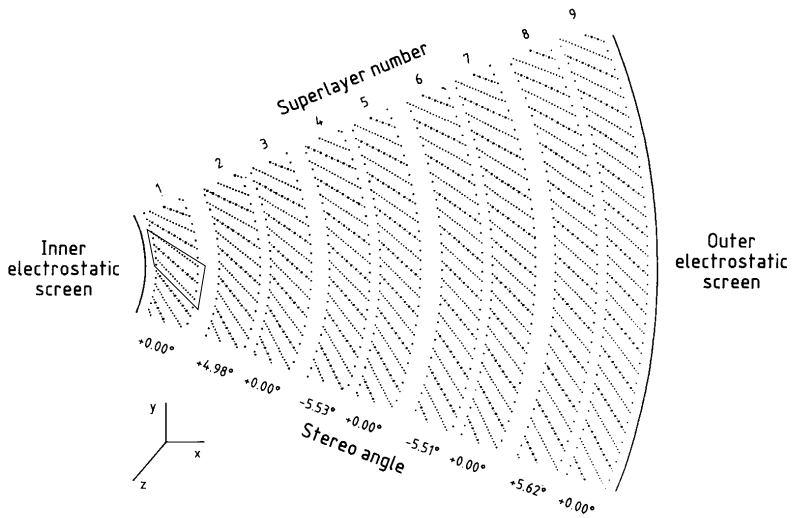

Figure 4.11: Cross section of a CTD octant. The wires are arranged in nine *superlayers*. The dots represent sense wires.

The CTD has a length of 205 cm, an inner radius of 18.2 cm and an outer radius of 79.4 cm. It covers a polar angle θ range from 11.3° to 168.2°. It is filled with a gas admixture of 80% argon (Ar), 8% carbon-dioxide (CO_2) and 2% ethane (C_2H_6). The CTD consists of 72 radial layers organized in 9 *superlayers* (SL) (see Fig. 4.11). The even numbered SL are parallel to the beam axis, whereas the four odd numbered layers are inclined by ±5° to allow a measurement of the z position of the hits. The resolution achieved by this stereo technique is about $\sigma_z = 1.0 - 1.4$ mm. The resolution in the $r - \varphi$ plane is about 230 μm. An other method for the z position measurement is called z-by-timing method. SL 1, 3 and 5 are designed to calculate the z position with a resolution of 4 cm, using timing information. The fast z-by-timing system mainly provides z-positions for the trigger decision.

Charged particles traversing the CTD ionize the gas along their path. The electrons are attracted by the positively charged sense wires, while the heavier cations drift to the negative field wires. The drift velocity of the electrons is approx. constant at 50 μm/ ns. Avalance-like multiplication occurs in the electrical field near the sense wires resulting in an amplification factor of about 10^4. Only the distance of the hit to the wire is measured, but not the direction w.r.t. the wire. This ambiguity of the hit

position is solved at reconstruction level by requiring continuous particle trajectories. For tracks crossing at least three SL, originating from the nominal vertex position with a transverse momentum of $p_T > 150$ MeV, the relative transverse momentum resolution can be parameterized as:

$$\frac{\sigma(p_T)}{p_T} = 0.0058 \cdot p_T \oplus 0.0065 \oplus 0.0014/p_T \tag{4.2}$$

with p_T in GeV. The first term gives the contribution of the position resolution of the hits, whereas the second and third term result from multiple scattering before and inside the CTD, respectively. In the HERA II period, the MVD is included in the track reconstruction. The hit resolution of the combined tracking is improved, but the additional material between the interaction point and the CTD increases the multiple scattering probability. The resolution of the combined system of CTD and MVD in not yet final, but a current approximation is [Gut05] (see also Sec. 5.3.2)

$$\frac{\sigma(p_T)}{p_T} = 0.0026 \cdot p_T \oplus 0.0104 \oplus 0.0019/p_T. \tag{4.3}$$

4.2.3 The calorimeter CAL

The uranium calorimeter CAL [Der91] is a compensating sampling calorimeter consisting of alternating layers of absorbing uranium and scintillator material. The calorimeter needs to be hermetical with a nearly full-solid angle coverage. A good hadronic energy resolution is achieved due to the equal response to hadronic and electromagnetic showers. The absorber plates are made of 3.3 mm thick depleted uranium (98.1% U^{238}, 1.7% Nb and 0.2% U^{235}) covered in stainless steel foils. To measure the particle energy, plastic scintillator plates (SCSN38) of 2.6 mm are located between the absorber plates. Usually the ratio of the measured energy to the energy of the incoming particle is higher for electromagnetic showers than for hadronic showers. The hadronic particles interact with the nuclei of the absorber and some energy is lost due to binding energy, nuclear fission fragments and undetected decay products. For electrons and photons the energy loss is smaller because they interact with the electrons of the molecules. Using uranium as an absorber for the hadronic calorimeter has the advantage to provide a high yield of spallation neutrons which transfer the energy to the hydrogen nuclei of the scintillators. In addition the photons from neutron capturing help to compensate the signal loss for hadronic showers. The ratio of the pulse heights for electrons to hadrons e/h for the ZEUS CAL is optimized to

$$e/h = 1.00 \pm 0.03 \tag{4.4}$$

for particle energies above ~ 5 GeV using the quoted thickness of uranium and scintillator layers. On that account the CAL is a so-called *compensating* calorimeter. The energy resolution of the CAL has been measured for electromagnetic and hadronic showers to be

$$\frac{\sigma_e}{E} = \frac{18\%}{\sqrt{E}} \text{ and } \frac{\sigma_{\text{had}}}{\text{E}} = \frac{35\%}{\sqrt{\text{E}}} \tag{4.5}$$

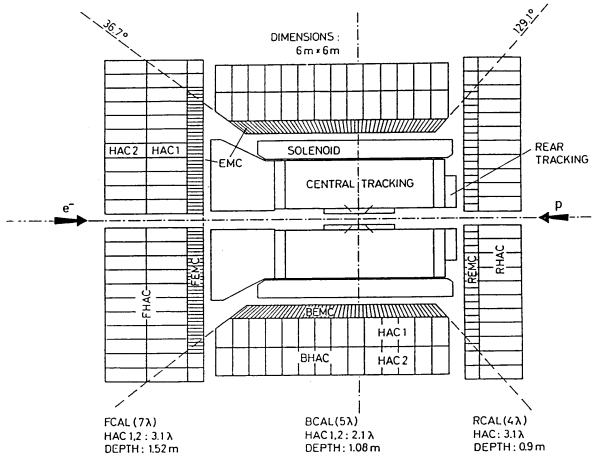

Figure 4.12: The regions of the CAL, showing the FCAL, BCAL and the RCAL with their electromagnetic (EMC) and hadronic (HAC) parts.

with the particle energy E in GeV.

The three regions of the CAL are the FCAL in the forward region, the BCAL in the barrel and the RCAL in the rear (see Fig. 4.12). Each CAL region is divided into *modules* separated into $20 \cdot 20\,\mathrm{cm}^2$ *towers* (Fig. 4.13 shows a FCAL module). Towers are longitudinally divided into one electromagnetic section (EMC) and two hadronic sections (HAC1 and HAC2). The EMC towers are divided further into four (in the RCAL only two) *cells*. The EMC cell size is $20\,\mathrm{x}\,5\,\mathrm{cm}^2$ for FCAL and RCAL, $20\,\mathrm{x}\,10\,\mathrm{cm}^2$ in the FCAL. In total the CAL consists of 5918 cells. Each cell is read out on two sides using photomultiplier tubes (PMT) with wavelength shifters. Due to that reason the sum of the PMT signals is approximately independent of the hit position in the cell and the horizontal position can be determined comparing both signals. Background particles coming not from the *ep*-collisions can be rejected using the high time resolution of $< 1\,\mathrm{ns}$ for particles with $E \geq 3\,\mathrm{GeV}$. The calibration procedure of the PMTs uses the natural radioactivity of the uranium and has to be performed about once a day.

4.2.4 The rear tracking detector SRTD

The precise measurement of the scattered electron is required to determine kinematic variables of the event. The *Small angle Rear Tracking Detector* (SRTD) [Bam97] is able to improve the angular measurement compared to the RCAL. In addition it identifies pre-showering electrons with the possibility to correct the energy loss in inactive material and identifies proton-beam-gas events from outside of ZEUS based on timing. The SRTD

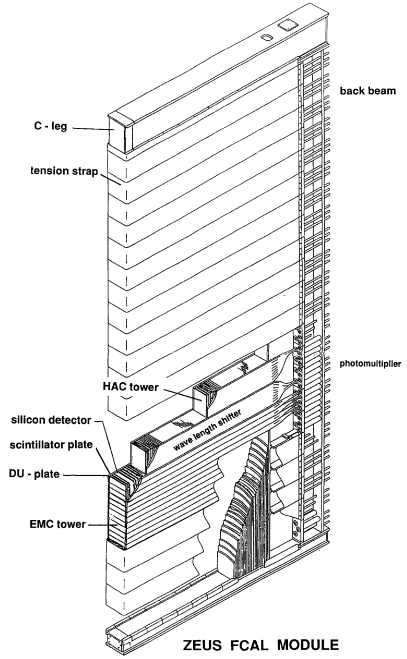

Figure 4.13: Layout of an FCAL module.

consists of two scintillator strip layers. One layer mounted in the vertical and one in the horizontal direction. The strips are either 24 cm or 44 cm long, 1 cm wide and 0.5 cm thick. The total surface is about $4200\,\mathrm{cm}^2$ around the rear beam pipe at $z = -148\,\mathrm{cm}$. The angular coverage is $162° < \theta < 176°$. The photomultipliers are located 2.5 m apart from the scintillators, in order to avoid the high magnetic field near the beam pipe. They are connected by bundles of optical fibers and provide 272 readout channels.

4.2.5 The backing calorimeter BAC

The backing calorimeter (BAC) [Bob92] uses the return yoke as an absorber to build an additional tracking calorimeter. It consists of aluminum proportional tubes filled with Ar-CO_2. The BAC vetoes showers leaking out through CAL, allowing the selection of event samples with a resolution corresponding to the intrinsic resolution of the CAL. It can distinguish between hadron and muon showers and provides muon identification and trigger capabilities in particular in the bottom yoke and other areas where no muon

chambers are present.

The BAC is built from modules inserted into the yoke (Fig. 4.5) consisting of $7-8$ tubes of a cross section of $11 \times 15\,\text{mm}$ and a length of $1.8-7.3\,\text{m}$. The modules are equipped with 50 cm long aluminum cathode pads in addition to the gold plated tungsten wires of $50\,\mu\text{m}$ diameter. The wires are read out at one side and provide both analog and digital signals whereas the pads have only an analog read out.

Energy is measured by summing up the analog signals from the wires grouped in addition into towers of a width of $25-50\,\text{cm}$ ($2-4$ modules) over the full depth of the BAC. The pads of $2-4$ adjacent modules are added to pad towers with an area of $50 \times 50\,\text{cm}^2$ (4 modules) similar to the wire towers. They provide a determination of the position of the energy deposit along the wires. The signals from the wires provide also pattern of hit positions in the BAC to reconstruct muon trajectories.

A summary of the BAC modules is given in Table 4.2.

	Barrel	Bottom	Forward	Rear
Area [m^2]	1902	296	460	322
Number of layers	9	9	10	7
Gas volume [m^3]	38.0	5.9	9.2	6.4
Number of 8-tube modules	2246	193	840	572
Number of 7-tube modules	658	120	280	112
Module length [m]	4.5 and 5.5	7.3	$1.8 \rightarrow 3.6$	$1.8 \rightarrow 3.6$
Number of wires	22574	2384	7980	5360
Wire towers	100	10	32	36
Pad towers	1100	150	222	230

Table 4.2: Summary of BAC modules.

The spatial resolution of the BAC is $\sim 1\,\text{mm}$ perpendicular to the wires, whereas the resolution parallel to the wires is constrained by the pad size. The energy resolution determined by test beam measurements is given as

$$\frac{\sigma_E}{E} \sim \frac{1.1}{\sqrt{E}} \tag{4.6}$$

with the particle energy E given in GeV.

4.2.6 The forward and barrel/rear muon chambers FMUON BRMUON

Apart from the BAC, the muon detector at ZEUS consists of two parts, the forward FMUON chambers and the BRMUON covering the barrel and rear area. The inner chambers, FMUI and BRMUI are located between the CAL and the BAC, the outer chambers FMUO and BRMUO outside of the BAC.

Fmuon

The FMUON [Hol93] (see Fig. 4.14) has the following structure:

- four planes of *limited streamer tubes* for triggering. They are equipped with a digital readout for ρ and φ (LST1 - LST4)
- two coverage planes of limited streamer tubes at larger polar angle (LW1, LW2). The digital readout of ρ and φ is supplemented by a analog readout of ρ
- four planes of *drift chambers* (DC1 - DC4)
- two large toroidal magnets producing a field of 1.7 T to be able to measure the momenta of the muons

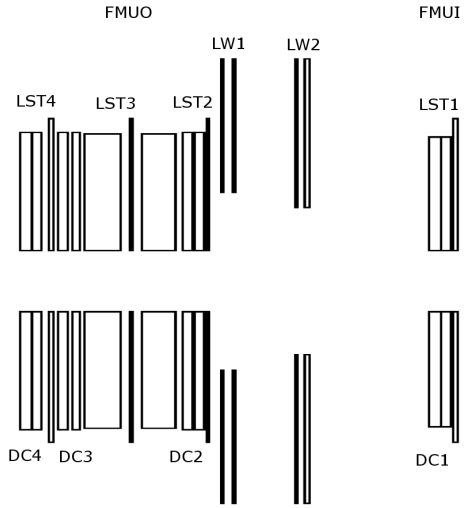

Figure 4.14: The FMUON detector.

The components mentioned before are described in more detail in the following.

The limited streamer tube planes (LST) serve the purpose to trigger on muon candidates and to reconstruct their position in terms of the azimuthal and radial coordinates of the track. A trigger plane is made of four LST chambers grouped in two half-planes. A quadrant consists of two layers of LST positioned horizontally inside a plastic sheet. The tubes of the two planes are slightly displaced (0.5 cm)

in order to achieve a complete geometrical acceptance. Each quadrant is contained in an air tight aluminum box. On the outer side, copper strips are glued in polar geometry. The LSTs induce a signal in the copper strips if a particle crosses the plane. The number of radial ρ strips is 132 while each strip is 1.9 cm wide. They are divided along the bisector of the quadrant so that the simplest unit of the trigger plane to be read out is the octant. The number of φ strips is 32 per octant. Each strip covers an interval of 1.4° in the azimuth angle.

The drift chambers are needed in order to obtain a good momentum resolution. Each plane consists of four chambers grouped two by two in two half planes fixed on a support panel. The basic element of the chamber is the *cell* made of four sense wires and of the layers needed to generate the appropriate electric field. The four sense wires measure the radial coordinate. The information gathered by the wires are sent to a TDC which converts them into a time interval related to the drift distance by a known relation.

The large angle coverage planes (LW) are needed in order to achieve the desired geometrical acceptance also in the region uncovered by the toroids ($16° < \theta < 32°$). Each plane consists of eight air tight aluminum wrappings that contain a LST layer. The LST signal is induced on copper strips with radial geometry spaced of 0.7° in the φ coordinate and of 1.8 cm in the ρ coordinate. The number of φ strips is 64 per octant while the ρ strips are 192 per octant. The achieved resolution in the ρ coordinate, using a center of gravity algorithm, is ~ 1 mm.

BRmuon

The BRMUON [Abb93] (see Fig. 4.15) chambers are different in shape and dimensions depending on their location, but the internal structure of each chamber is the same. The supporting structure of a chamber is an aluminum honeycomb frame 20 cm thick in the inner and 40 cm in the outer chambers. Two planes of LST are placed on both sides of the frame. The two layers on the same side of the chamber are displaced by 8.3 mm in order to minimize inactive areas for particles traversing at 90° with respect to the wire plane. Each LST is made of a plastic profile with eight cells. In each cell a copper-beryllium wire of 100 μm diameter is located. The distance between two sense wires is 1 cm.

Each LST plane is equipped on one side with 13 mm wide readout strips with 15 mm pitch that run orthogonal to the wires. In the BMUI and BMUO chambers the LSTs are parallel to the beam direction while in RMUI and RMUO they are horizontal (parallel to the ZEUS x direction). With the analog strip readout the achievable spatial resolution on the coordinate orthogonal to the wires is 200 μm while it is 700 μm for the coordinate parallel to the wires.

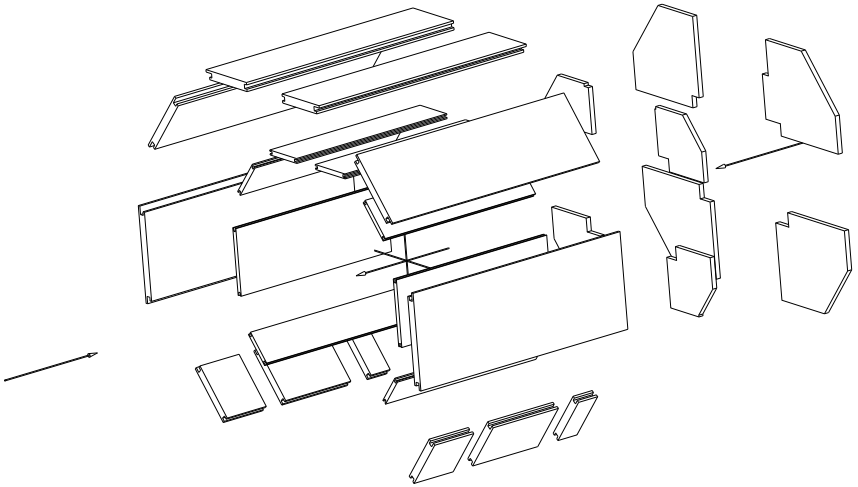

Figure 4.15: The BRMUON detector.

4.2.7 The luminosity monitor LUMI

The high precision measurement of the integrated luminosity is essential for the determination of cross sections. The reaction used at ZEUS is the Bethe Heitler Bremsstrahlung process $ep \rightarrow e'p\gamma$. As a QED process, the event rate is well known (it is calculated differentially as a function of the photon energy to an accuracy of 0.5 %) and the rate is sufficiently high ($\sigma_{BH} \approx 20$ mb) to avoid the domination of the statistical error. The luminosity $\mathcal{L}$, integrated over time, is defined as

$$\mathcal{L} = \frac{N_{proc}}{\sigma_{proc}}. \tag{4.7}$$

N_{proc} is the number of events produced in a process with cross section σ_{proc}. The photons from this process are scattered at very low angles, so they escape the main detector through the beam pipe and leave the beam pipe at $z = -92.5$ m through a Cu-Be window. They are detected in the luminosity monitor at $z = -107$ m (Fig. 4.16). The LUMIG detector [And01] is a lead/scintillator sampling calorimeter. It is shielded against synchrotron radiation by a sandwich structure of carbon and lead. The energy resolution of this system is measured to be $23\ \%/\sqrt{E}$ with E in GeV. The luminosity is calculated, counting the numbers of photons above a certain energy threshold and correcting for the detector acceptance and pile-up effects. The main origin of background is the Bremsstrahlung of the electrons interacting with residual beam gas. To take this background into account, it is measured using *pilot bunches*, i.e. electron bunches without a matching proton bunch. The systematic errors mainly come from the background

subtraction, pile-up effects, energy calibration, linearity and acceptance of the photon calorimeter. That gives an overall systematic uncertainty between 1.5 % and 2 %.

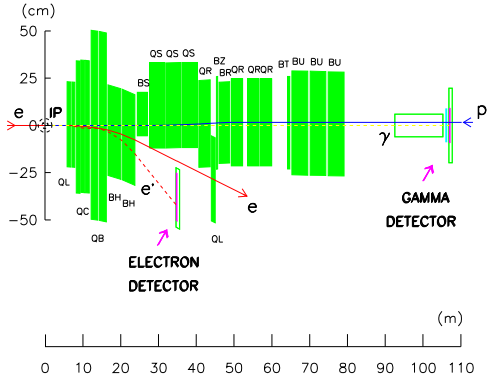

Figure 4.16: The lumi monitor system with the gamma detector (LUMIG) and the electron detector (LUMIE).

4.2.8 Trigger and data acquisition

The HERA bunch structure leads to a beam crossing every 96 ns corresponding to a event rate of up to 10.4 MHz. The raw rate of hits in different detector components is very high and it is neither possible nor reasonable to keep all this information. Apart from noise in the sensors and the electronics, the main background comes from beam gas events. These are collisions of electrons and protons with residual gas nuclei or with the beam pipe at a rate of 10 kHz. Muons produced in the atmosphere, called *cosmic muons*, traverse the CTD at a rate of about 500 Hz. The rate that the ZEUS data acquisition system (DAQ) is able to write to tape is about 10 Hz. Thus a significant reduction of the number of events is needed. The purpose of the trigger system is to preselect interesting physics events and to reduce the rate of events to record (see Fig. 4.17). The trigger [Smi92] is organized in three levels with increasing complexity and decreasing event rate.

first level trigger FLT: Each detector component is equipped with a FLT, hard-wired in single-component logic circuits. Each FLT provides a trigger decision within 2.2 μs based on thresholds, energy sums or timing information.These trigger decisions are gathered at the *global first level trigger* (GFLT) while the event data is stored in logical pipelines. The GFLT combines different trigger slots and provides the decision after $\approx 4.4\,\mu$s. The accepted events are passed to the second level of the trigger system. The trigger processing for all components is pipelined and dead-timeless, accepting data from every bunch crossing. The output rate of the GFLT has to be below 1 kHz.

second level trigger SLT: The SLT is implemented on a transputer network. The decision of the GFLT is analyzed further and the event quantities are recalculated to a higher degree of precision. CAL timing information is used to reject beam gas events. The decisions of several branches of the SLT are collected by the *global second level trigger* (GSLT) which provides a decision for up to 64 slots after 7 ms and reduces the event rate to $50 - 100$ Hz. In HERA II, the *global tracking trigger* (GTT) [Dha03] was implemented in hardware and software to combine the information of the main tracking devices (CTD, MVD and STT) to benefit from the enhanced tracking capabilities. The combined trigger decision can be used to efficiently reduce the rate on the second trigger level and is currently finding its commissioning.

third level trigger TLT: For accepted events the data of all components is combined in a single record of ADAMO [Fis93] database tables by the event builder and passed on to the TLT. The TLT uses a computer farm for the analysis and classification of each event. Based on physical quantities of the fully reconstructed events, such as kinematical variables, output of the electron finding algorithms, topologies of hadronic final states etc., a decision is made split into 192 trigger slots and the accepted events are classified. Accepted events (with a size of approximately 150 kbyte) are written to tape at a rate of $10 - 15$ Hz. Offline they are fully reconstructed by the ZEUS software.

4.3 Detector simulation

To provide the same data structure for data measured with ZEUS and simulated data using Monte Carlo (MC) generators, the detector is simulated using different stages. The MC generator (e.g. RAPGAP or PYTHIA) produces lists of final state particles with their four-vectors for every event. The *detector simulation* takes care of the interaction of particles with the detector in the path of the particle. The detector geometry is implemented in a program called MOZART using the GEANT package [Bru84]. The detector response is simulated by GEANT, taking into account processes like energy deposit, multiple scattering and in-flight decays. Also the trigger logic has to be simulated before the event is passed to the event reconstruction ZEPHIR which is the same for Monte Carlo and for recorded data.

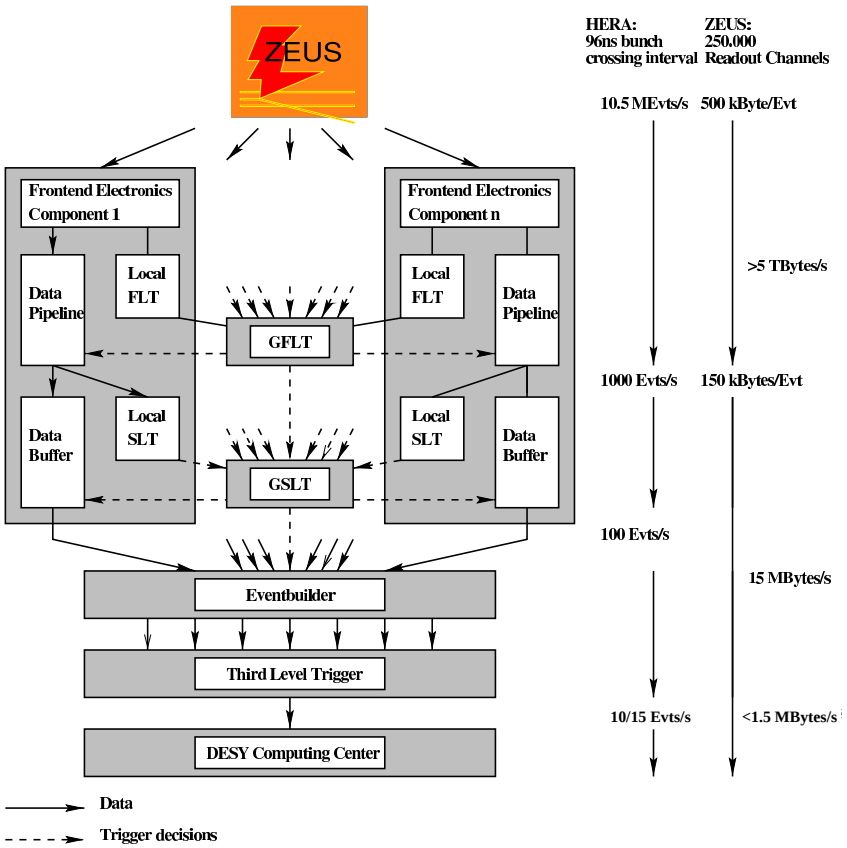

Figure 4.17: Diagram of the ZEUS trigger and data acquisition system

Chapter 5

Event Reconstruction

This chapter describes the algorithms used to reconstruct event quantities for the process:

$$e\,p \rightarrow e\,b\bar{b}\,X \rightarrow e\,\mu\,jet\,X', \tag{5.1}$$

the production of a beauty quark and anti-quark pair in deep inelastic scattering and the semi-leptonic decay of at least one b quark into a muon and a jet.
In this chapter the measurement techniques are introduced. The cuts that are used to select the event sample are described in Chapter 7.

5.1 Introduction

Events fulfilling the pre-selection of the trigger algorithm are available for a detailed reconstruction of event properties.
As an example Figure 5.1 shows a beauty candidate event in the ZEUS event display. The first step is the reconstruction of particle tracks using information from the tracking detectors (MVD, CTD and also the CAL).
The kinematic variables Q^2, x and y are obtained mainly using the measurement of the scattered electron.
In the main part of this chapter the reconstruction of muons is described. Great effort is required to achieve high muon detection efficiency. Many different detector components and algorithms are combined in a new muon reconstruction, called GMUON.
The hadronic part of an event is represented by four-vectors, called EFOs. The EFOs are corrected for different reasons, like the presence of a muon, before they are used for jet reconstruction.
The last step is the association of a muon and a jet to measure p_t^{rel}.

5.2 Trigger algorithms

As described in Section 4.2.8, events are recorded only if they are accepted by at least one trigger slot. During the HERA II data taking period, the configuration of the trigger

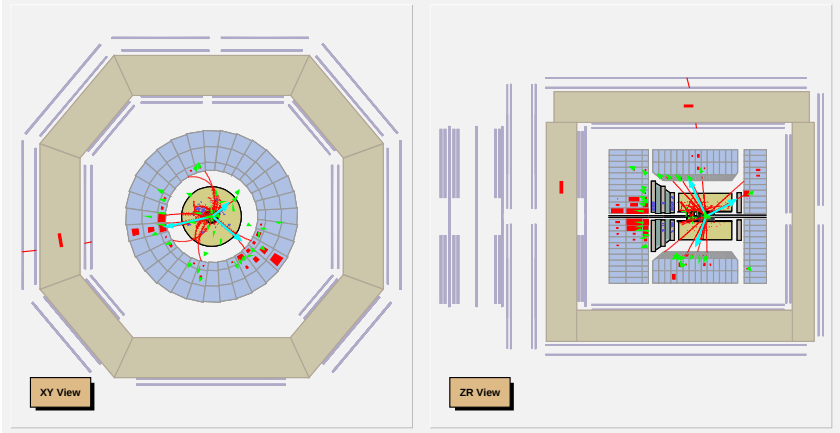

Figure 5.1: Event display of a beauty candidate event in the xy-plane (left) and in the zr-plane (right). Shown are reconstructed track helices (red lines, see Sec. 5.3), the CAL cluster (red cells in the CAL) and the EFOs (green arrows), see Section 5.6. Two jets are reconstructed (blue arrows), the third arrow in the rear part is the DIS electron, this is not a jet in this analysis (see Sec. 5.4). A muon associated to one jet is clearly detected by its MIP signature in the CAL, a hit in the muon chambers and in the BAC (see Sec. 5.7).

changed a couple of times. Thus, the simulation of the trigger system takes these changes into account. For DIS events the main slots on the third trigger level (TLT), used in this analysis are: an inclusive DIS trigger (called SPP02), a trigger for mesons in DIS (HFL2), a muon in DIS trigger (HFL14) and a trigger for jets in DIS (HFL6). For the definition of trigger cuts, see [Tri05].

5.3 Track reconstruction

To reconstruct charge and momentum of a particle, the measurement of the track in the magnetic field inside the detector is used. Furthermore the energy loss along the track sometimes even allows the identification of the particle. Tracks are reconstructed particle trajectories extracted from hit information in the tracking detectors. The routine to reconstruct tracks has to take into account the influence of the magnetic field and the multiple scattering in the detector material. The main tracking devices in ZEUS are the CTD (see Sec. 4.2.2) and for HERA II also the MVD (see Sec. 4.2.1). Technically the tracks are described by five parameters in the helix parameterization [Har98] (see Fig. 5.2). This parameterization is chosen to describe the particle track in the toroidal magnetic field parallel to the beam pipe. The first three parameters define a circle in

the xy plane and the latter two parameters the location and pitch in z. The parameters are:

a_1 φ_H: angle tangent to the helix in xy

a_2 Q/R: ratio of charge Q to local radius R

a_3 $Q \cdot D_H$: D_H connects the helix to the reference point at $(X_{ref}, Y_{ref}) = (0, 0)$

a_4 Z_H: the z position of the reference point

a_5 $\cot\theta$: the angle of dip in the xy plane

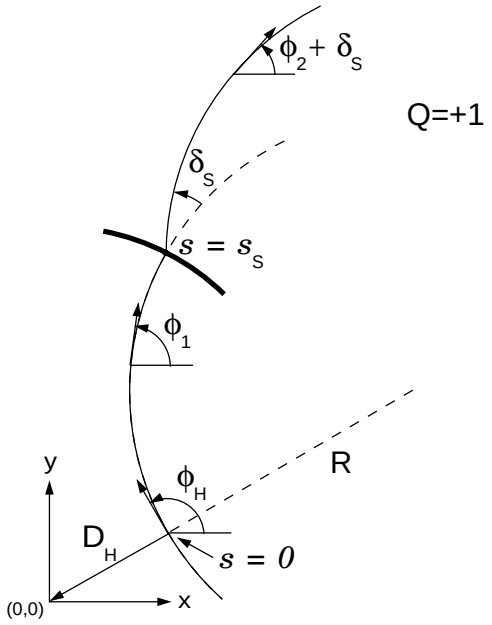

Figure 5.2: Helix parameterization[Har98]

The track reconstruction in the HERA I data period is based on the CTD. Only in HERA II the MVD is available to improve the track resolution. The former track reconstruction is called CTD-*only*, while the latter is denoted as *regular tracking*.

5.3.1 CTD-only tracking

The CTD hits, including their errors, are used to perform a helix track fit. In the first step the three outermost axial CTD hits are used as a seed for *pattern recognition*. In the next step these seed hits together with all other hits picked up in the same superlayer, called CTD *segment*, are assigned to tracks. The ambiguity of the hit position on the CTD wires is solved requiring the reconstruction of continuous track (see Sec. 4.2.2). After the track fit a vertex fit follows, using the vertex as an additional constraint.

5.3.2 Hera II-tracking

In the HERA II data the MVD supplements the track reconstruction procedure providing high precision position measurements near the vertex.

The pattern recognition of the so called *regular-tracking* incorporates hits from the CTD and the MVD and combines matching track segments in the CTD with clusters of hits in the MVD. Tracks that are found only in one detector component are also used. The vertex fit takes all track categories into account.

The tracking precision can be improved by using a *Kalman filter* [Kal60, Fru87]. This method (called *ZTT-tracking*) uses CTD-MVD fitted tracks as a seed to improve the track parameter accuracy near the vertex. It includes multiple scattering in the inactive material of the MVD. The Kalman-fitted tracks are used as input to a second vertex fit. The resulting tracks are useful to study secondary vertices in the range of hundreds of micrometers, e.g. from beauty meson decay, or to measure impact parameters.
Fig. 5.3 shows the tracking resolution for the CTD-only and regular tracking.

The transverse momenta of reconstructed tracks are compared to the corresponding true information using MC simulations [Mad04]. The resolution of the Kalman filter track reconstruction (Eq. 4.3) is similar at lower transverse momenta and significantly better at higher transverse momenta compared to the HERA I resolution (Eq. 4.2). Advancements in the internal alignment of the MVD and the alignment with respect to the CTD will improve the resolution further.

For impact parameter studies, the accuracy of the reference point is an important ingredient and usually the primary vertex is chosen. Currently, the primary vertex is technically not yet stable. Therefore, the beam-spot is taken as the reference. The beam-spot is the average of the vertex distribution per run. Using Kalman-fitted tracks and the latest MVD alignment with a transverse momentum cut of $p_t^{track} > 0.5\,\text{GeV}$ and at least 4 used hits in the MVD, the primary vertex is determined by a vertex fit in all events of the run fulfilling above requirements. The distribution of primary vertices per run is fitted with a Gaussian where the sigma of the fitted Gaussian distributions gives the reconstruction width of the beam-spot and therefore its resolution. Fig. 5.4 shows an exemplary beam-spot fit for a single run yielding a vertex resolution of $\sim 150\,\mu$m in x and $\sim 140\,\mu$m in y.

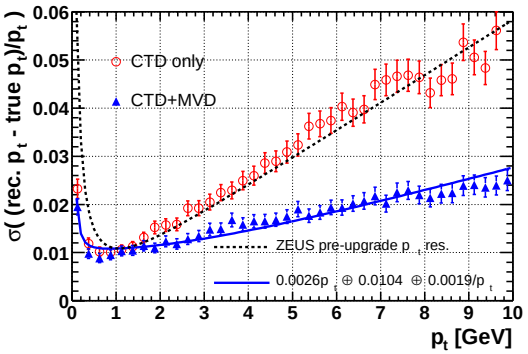

Figure 5.3: Resolution of the CTD-only and the CTD-MVD combined track reconstruction. The relative p_T^{track} error of the comparison of true and reconstructed transverse momentum of a track is shown [Gut05].

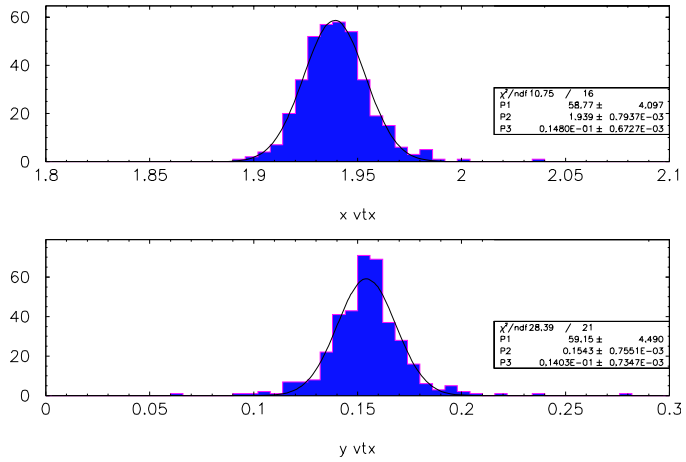

Figure 5.4: Width of the beam-spot vertex distribution using Kalman-fitted tracks. The beam-spot width is $\sim 150\,\mu$m in x and $\sim 140\,\mu$m in y [Gut05].

5.4 DIS electron identification

Deep inelastic scattering events are characterized by a scattered electron in the detector and thus a $Q^2 > 1\,\text{GeV}^2$. The kinematic variables, like Q^2, $x_{bjørken}$ and inelasticity y,

can be reconstructed from the quantities of the scattered electron. Thus it is essential for a DIS analysis to gain a high efficiency and purity of the electron reconstruction. To find this electron the specialized electron finder Sinistra [Abr95] is used. Sinistra uses neural-network techniques to find the electron candidate with the highest probability to be the DIS electron. The algorithm was trained on shower properties of electrons and hadrons in the CAL. Every event is characterized by a set of variables. To collect these variables, the first step is to cluster the CAL cells that are hit into *calorimeter islands*. In addition the shape of the energy distribution is recorded, in particular the longitudinal component, to distinguish between electrons and hadrons. The output of the neural-network P can be interpreted as the probability, that the shower is caused by an electron. Islands with $P \geq 90\%$ and $E_e > 4\,\text{GeV}$ are called electron candidates. The efficiency of Sinistra to find the DIS electron in an event is about 85% for electrons of $\theta_{electron} \geq 2.2\,\text{rad}$, $E_{electron} \leq 30\,\text{GeV}$ and $Q^2 \leq 100\,\text{GeV}^2$ [Lop99].

In this analysis the identified DIS electron is also used to reconstruct the kinematic variables. The scattering angle θ_e is measured using the electron position in the calorimeter combined with the vertex position. The electron position in the CTD is determined using the cells associated to the electron candidate. If possible, the CTD and SRTD are used to improve the resolution of the position measurement. The details of the position determination can be found in [Doe94]. The achieved resolution is 1 cm in x and in y.

For low values of Q^2, thus small scattering angles ($\theta_e > 162°$), the SRTD is used. Due to its fine segmentation (see Sec. 4.2.4) the resolution nearly reaches 3 mm [Ng95]. 45% of the events selected for this analysis are measured in this region. The increased amount of material between the vertex and the SRTD in HERA II and the resulting degradation of the resolution is still under investigation.

5.5 Kinematic variables

An event can be separated into two parts: the electron state and the hadronic state. While the electron state is defined by θ_e and E_e, the hadronic state (everything that is not part of the electron state) can be described by δ_{had} and the total transverse momentum $p_{t,had}$:

$$\delta_{had} = \sum_{had}(E_{had} - p_{z,had}) \tag{5.2}$$

$$p_{t,had} = \sqrt{\left(\sum_{had} p_{x,had}\right)^2 + \left(\sum_{had} p_{y,had}\right)^2} \tag{5.3}$$

The sum runs over all hadrons or hadronic EFOs (see Sec. 5.6.1) respectively.

The hadronic part can also be transformed to E_{had} and γ_{had}, the energy and the angle of the hadronic system respectively. The angle of the hadronic system is expressed by:

$$\cos\gamma_{had} = \frac{p_{t,had}^2 - (E_{had} - p_{z,had})^2}{p_{t,had}^2 + (E_{had} - p_{z,had})^2} \tag{5.4}$$

Only two of the kinematic variables x, y and Q^2 are independent (see Sec. 2.2), so only two of the four measured variables are needed. In the following, two different methods are described to reconstruct the kinematic variables.

5.5.1 Electron method

The so-called *electron method* only uses the energy and angle of the scattered electron. The kinematic variables Q^2, x and y are expressed as:

$$Q^2_{el} = \frac{E_e^2 \sin^2\theta_e}{1-y_{el}} \quad (5.5)$$

$$y_{el} = 1 - \frac{E_e}{2E_{e,beam}}(1-\cos\theta_e) \quad (5.6)$$

$$x_{el} = \frac{Q^2_{el}}{s y_{el}} \quad (5.7)$$

using the energy of the incoming $E_{e,beam}$ and scattered E_e electron. θ_e is the scattering angle and s the center-of-mass energy squared. The relative error of y_{el} is given by [Kle91]:

$$\frac{\delta y_{el}}{y_{el}} = \left(1-\frac{1}{y_{el}}\right)\frac{\delta E_e}{E_e} \oplus \left(\frac{1}{y_{el}}-1\right)\cot\left(\frac{\theta_e}{2}\right)\delta\theta_e \quad (5.8)$$

This method relies on an accurate reconstruction of angle and energy of the scattered electron. The measurement of the electron angle is quite accurate, but the energy measurement is more difficult due to inactive material and initial state radiation.

5.5.2 Jacquet-Blondel method

An other method to estimate the kinematic variables, introduced by Jacquet-Blondel [Blo79] uses the hadronic final state. The quantities can be expressed as:

$$Q^2_{jb} = \frac{p^2_{t,had}}{1-y_{jb}} \quad (5.9)$$

$$y_{jb} = \frac{\delta_{had}}{2E_e} \quad (5.10)$$

$$x_{jb} = \frac{Q^2_{jb}}{s y_{jb}} \quad (5.11)$$

where $p_{t,had}$ denotes the total hadronic transverse momentum and $\sum_{had}$ is the sum over the hadronic final state particles in the detector. The Jacquet-Blondel method gives a better resolution for low y than the electron method, because the resolution does not depend on terms proportional to $1/y$:

$$\frac{\delta y_{jb}}{y_{jb}} = \frac{\delta E_e}{E_e} \oplus \cot\left(\frac{\theta_{jb}}{2}\right)\delta\theta_{jb} \quad (5.12)$$

This is the only method for CC DIS events, but for NC DIS the resolution of the electron method is usually better.

Other methods, like the double angle method [Ben91] or the Σ method [Bas95] are not used in this analysis and therefore only mentioned here.

5.6 Hadronic system

In order to measure the momentum or energy of particles two different approaches are used in ZEUS. The uranium calorimeter (see Sec. 4.2.3) is the main device to measure the energy of the hadronic system. Tracks in the magnetic field of the solenoid are measured using the CTD to determine the momentum of particles
The CAL measurement is accurate for high energy particles but for particles with low energy the detector noise dominates the resolution (see Fig 5.5). The CTD resolution is better at low momentum, because the curvature of charged particle tracks in the magnetic field is stronger for low particle momenta. The best reconstruction is achieved, using a combination of CTD measurements mainly for particle energies below 10 GeV to 15 GeV and CAL measurements for particles with higher energies.

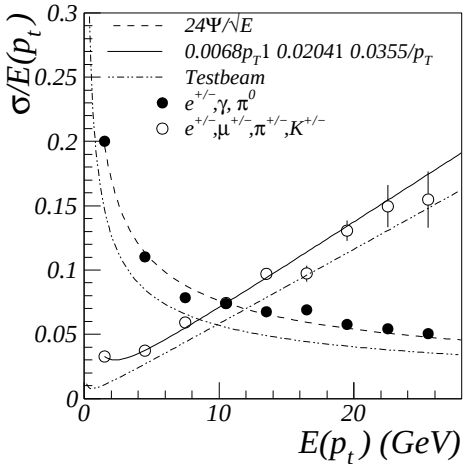

Figure 5.5: Relative resolution of the measurement of p_t in the CTD (open dots) and the electro-magnetic energy in the EMC of the CAL (full dots) obtained from single particle MC [Tun01].

The methods to combine both measurements and to apply energy corrections due to inactive material are described in the following. Furthermore, the subtraction of the DIS electron is explained.

5.6.1 Energy Flow Objects EFO

The hadronic system in ZEUS is represented by four-vectors, so-called *Energy Flow Objects* (EFOs)[1]. The EFOs are obtained by a clustering algorithm consisting of two stages. In the first stage, hits in each section of the CAL, the EMC, HAC1 and HAC2 are clustered to *cell islands* (see Fig. 5.6). The cell with the highest energy deposit is the starting point. Then the adjacent cell with the highest, non-zero energy is connected to the starting cell. Also cells next to the nearest neighbors are considered. This procedure is repeated for each cell to produce a unique assignment of cells to cell islands.

The second stage clusters the cell islands into 3-dimensional *cone islands*, connecting the CAL sections. The matching starts at HAC2 and goes inwards. The angular separation to neighboring islands is calculated in polar and azimuth angle. A matching probability is calculated according to the separation in a single pion MC simulation [Tun01]. After the clustering, charged particle tracks originating from the inner tracking detectors (see Sec. 5.3), are extrapolated to the inner surface of the CAL and associated to cone islands. Only tracks fulfilling the following quality requirement are used for the matching. The track has to be vertex fitted and has to traverse at least 4 CTD superlayers, the transverse momentum has to be in the range $0.1 < p_t < 20\,\text{GeV}$ or $0.1 < p_t < 25\,\text{GeV}$ for more than 7 crossed superlayers. The matching is done by calculating the *distance-of-closest-approach* (DCA) of a track to a cone island. For a DCA smaller than 20 cm or if the track lies inside the area of the island, the track is associated to the island. Which four-vector is assigned to the new EFO depends on the association of tracks to islands. For EFOs using the momentum measurement in CTD, the calculation of the EFO four-vector assumes the EFO to be a pion ($m_{\text{EFO}} = m_\pi$). If the three-vector of the EFO is determined from CAL information, the EFO mass is set to zero. Different cases can be distinguished:

- A track without a matching island: the EFO energy is determined from the tracking momentum
- CAL island without a track: the calorimeter energy is used to determine the three-vector of the EFO
- for a association of one track to two or three islands or two tracks to one or two island, the sum of the island energies or track momenta is used
- more than three tracks are associated to one island: the calorimeter information is used for the EFO

To gain the best resolution, the track information is used for the EFO if the following requirements are met:

- The CAL energy deposit is due to the associated track alone: The momentum of the track exceeds the energy in the calorimeter island more than the CAL measurement error. To cover a possible underestimation of the error, the error is scaled up by 20%.
- The relative error of the track momentum is smaller than the error of the CAL energy (see Fig. 5.5).

If the EFO is classified as a muon candidate, the track information is favored because the muon usually loose only the energy of a MIP in the CAL (see Sec. 5.7).

[1] in ZEUS nomenclature they are also called ZUFO, ZEUS Unidentified Flow Objects

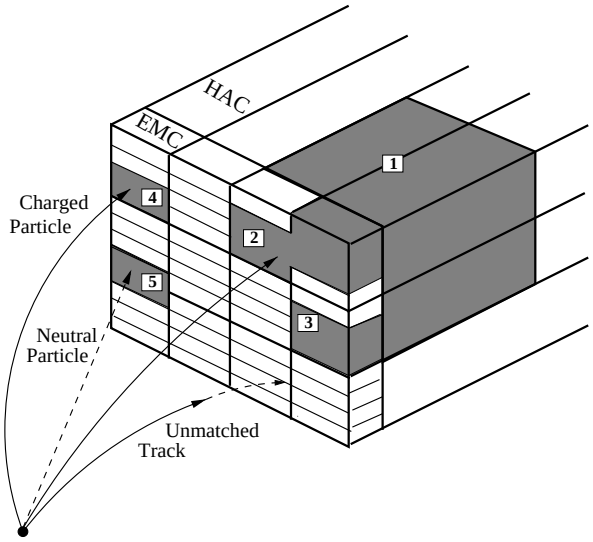

Figure 5.6: Schematic view of an EFO. Four EMC cell islands and one HAC cell island are shown. EMC cell islands 1 and 2 are joint with the HAC cell island to a cone island[Tun01].

5.6.2 Cone Island Corrections

The energy of the EFOs, determined by the calorimeter, has to be corrected for different reasons. The measurement in the CAL can overestimate the energy, e.g. for low momentum hadrons, or underestimate the energy for muons or particles passing inactive material in front of the CAL. The EFO that corresponds to the DIS electron is flagged for later identification.

Inactive material correction

In principle, the distribution of inactive or dead material, mainly the beam-pipe, the tracking detectors and the solenoid, is implemented in MC programs. In particular for the additional material in HERA II, the MVD with cables and support structures, the simulation is not very accurate. The distribution of material in front of the calorimeter is shown in Figure 5.7. The amount of matter varies between 1 and 3 radiation length X_0 depending on φ and θ. The energy loss is more significant for low particle energies and the correction is applied as a function of the energy and the position of the EFO.

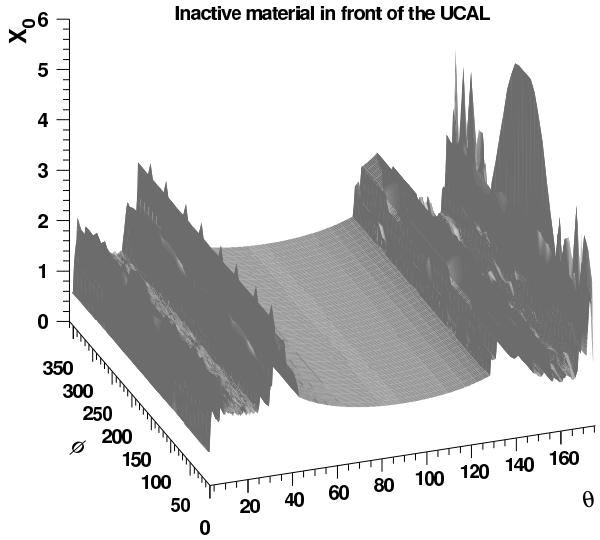

Figure 5.7: Map of the material distribution in units of the interaction length x_0 between the interaction region and the CAL as a function of θ and φ.

Correction of low momentum hadrons

Hadrons or muons with momenta below about 1 GeV lose their energy dominantly through ionization without hadronic interactions. In this case, the calorimeter is not compensating, the e/h ratio falls to $e/h \approx 0.6$. Therefore the measured energy is about 60% higher than it should be and is corrected.

Muon correction

Muons with a momentum above some GeV are not absorbed by the CAL. They traverse the calorimeter, leaving only the MIP energy. As described in Sec. 5.6.1, the energy of EFOs identified as muons is preferably taken from the track measurement. For calorimeter islands without a track association or with more than one track pointing to it, the situation is more complicated. In particular muons inside hadron jets, as required in this analysis, are often not isolated and further corrections to the EFO energy have to be applied. The energy deposit in the CAL as a function of the polar angle φ is shown in Figure 5.8. The average energy loss of a muon is about $1.5 - 3$ GeV in the whole CAL. The energy of the CAL island is corrected using the expected energy deposition

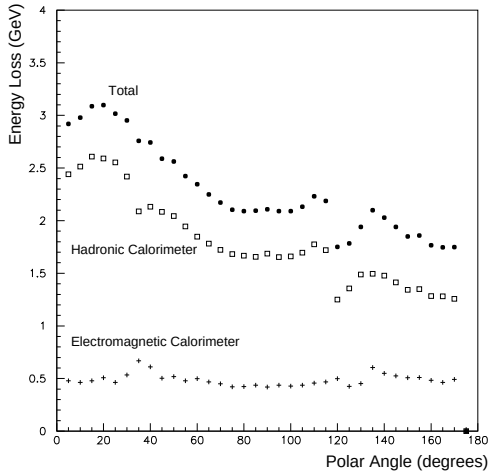

Figure 5.8: Measured energy loss of muons in the CAL as a function of the polar angle φ. The full dots indicate the total energy deposit, the open squares and the crosses are the energies in the HAC and the EMC respectively [Lon03].

of the muon. The muons are selected by the general muon reconstruction (see Sec. 5.7). A preselection of good muons is performed applying the cuts:

- muon quality ≥ 4
- $p > 1$ GeV
- only vertex fitted muon track

The corrections to the EFO depends on the rate of the expected MIP energy deposit and the measured EFO energy. They are categorized as follows:

- If the EFO uses the track for the energy determination, no further correction is needed
- If the EFO uses the energy of the calorimeter island and this energy is compatible with a muon ($50\%E_{\mathrm{MIP}} < E_{\mathrm{EFO}} < 150\%E_{\mathrm{MIP}}$), the EFO energy is replaced with the track measurement
- If the EFO uses the energy of the island which is higher than the expected MIP energy, the EFO is split into two EFOs. One EFO is set to the four-vector of the muon track, while the other holds the difference between the original EFO and the muon EFO in order to separate the muonic and the hadronic system of the event.
- If the energy of the EFO is much lower than the expected MIP energy loss, a new EFO of the muon four-vector is added to the list of EFOs.

Electron flagging

For DIS events, the list of EFOs is searched for the best correlation with the electron candidate with the highest Sinistra probability. The energy, φ and θ are used to find the electron-EFO. To exclude it later easily from jet clustering algorithms (see 5.10) it is flagged.

5.7 Muon reconstruction

The selection and reconstruction of muons is important, in particular for this analysis in order to measure muons from semi-leptonic beauty quark decays. Therefore more than one detector component and algorithm is used to reconstruct the muon properties.
Muons are special particles concerning the penetration power in matter. They are minimal ionizing particles (MIPs), that means their energy loss in the uranium of the calorimeter is almost independent of the muon momentum. The energy deposit can be calculated as [Eid04]:

$$\frac{dE}{dx} = 1.082\frac{\mathrm{MeV}}{\mathrm{g/\,cm^2}} \tag{5.13}$$

giving a range in iron of about:

$$\mu \text{ range in iron} \approx 1\,\mathrm{m/\,GeV} \tag{5.14}$$

The composition of uranium and scintillator in the CAL yields a similar range. The nuclear interaction length of hadrons (about 17 cm for pions in iron) gives a much shorter range of hadrons in matter. Electrons with energy above some MeV lose their energy inside the calorimeter mainly by bremsstrahlung and pair production generating electromagnetic showers. These are absorbed within centimeters. Taus are too instable to travel longer distances. Neutrinos are not detectable in ZEUS.
The key characteristics to identify muons and distinguish between semi-leptonic muons and background muons from pion and kaon in-flight decays, are:

- vertex association of the track; for high precision measurements also association to a secondary vertex from heavy quark decay close to the primary vertex
- MIP energy loss in all detector components along their track
- long range and reaching of the outer detector components e.g. muon chambers and the BAC

To detect and measure muons in ZEUS, different components are useful. The tracking, calorimetric and dedicated muon detectors are listed as an overview:

- tracking detectors:
  - MVD (only available in the HERA II period)
  - CTD (central region)
  - FDET (forward region)
  - FMUON (forward region)
- calorimeter detectors:
  - CAL (forward, barrel and rear parts)
  - BAC (partially also tracking detector)
- muon chambers:
  - FMUON (forward chambers)
  - BRMUON (barrel and rear chambers)

The forward muon reconstruction uses the forward tracking information of the CTD to reconstruct a muon track and the energy signature in the FCAL (energy in the electromagnetic and both hadronic parts) corresponding to a MIP. Also the muon hits in the forward muon chambers (FMUON: leads to an additional reconstruction of the muon) and the BAC information are used.
In the barrel and rear part, the CTD is used to reconstruct a muon track and the CAL to find the MIP signature of the muon. The barrel and rear muon chambers and the BAC are used in addition to identify the muon.

5.7.1 Muon reconstruction algorithms

Different algorithms for muon identification are available for ZEUS. Most of them are using the BRMUON or FMUON chambers (primarily BREMAT and MPMATCH), some the BAC (i.e. MUBAC) or only the CAL information (MV). The recently developed GMUON finder combines many algorithms in order to exploit the redundancy for a better signal to background ratio and good geometric coverage. In the following, only the algorithms actually used in this analysis are described.

GLOMU: Inclusive Muon Reconstruction at the third trigger level

The muon reconstruction algorithm GLOMU [Abb93] is a muon finder for the third level trigger. It is also available for offline analysis. GLOMU combines the muon track segment reconstruction in the inner chambers of BMUON and RMUON with the tracking in the CTD and a MIP signature in the CAL.
The χ^2 fit includes the following information:

muon track segments in the inner BRMUON chambers: For each track the point of entrance and the polar and azimuth angle θ and φ with the associated errors are available.

good quality track in the CTD: A track meeting the following requirements:

- $\chi^2 \leq 20$
- $D_H \leq 10\,\text{cm}$
- $|z| \leq 75\,\text{cm}$
- $\theta \geq 20^\circ$
- barrel region: $p_t \geq 1\,\text{GeV}$
- rear region: $p \geq 1\,\text{GeV}$

is extrapolated outwards to a fiducial volume outside the CTD. Each extrapolated track provides position, the direction in polar and azimuth angle θ and φ and the momentum and the errors at the fiducial volume.

MIP in the CAL: energy deposits compatible to a MIP are reconstructed using a specialized MIP finder. Output variables are the position and the timing information for each MIP.

The matching is performed in θ and φ separately for all combinations of the following properties. θ and φ obtained by:

- a CTD track
- a BRMUON track
- a segment connecting the CTD-CAL points
- a segment connecting the BMUI-CAL and RMUI-CAL points.

The total χ^2 is the sum of all χ^2_θ and χ^2_φ. A total $\chi^2 \leq 20$ is required for the matching. The advantage of GLOMU is the low p/p_t threshold and reasonably low background. But the algorithm is appropriate only for semi-isolated muons within the reduced geometrical coverage of the inner barrel and rear muon chambers. The efficiency to GLOMU is only moderate.

BREMAT: Barrel and Rear Extrapolation MATching

The BREMAT algorithm [Abb99] performs a match between tracks extrapolated from the CTD to the inner chambers of BMUON and RMUON and reconstructed muon segments. Only muons with a momentum of at least $1 - 1.5\,\text{GeV}$ traverse the CAL to reach the inner muon chambers. This defines the momentum threshold for BREMAT.

The extrapolation of a muon candidate track to a reference surface on the inner muon chambers takes into account the characteristics of a muon traversing the ZEUS detector.

The magnetic field in the CAL does not have a strong influence on the track extrapolation. The field is small in the CAL compared to the inside of the solenoid. The GEANT package [Bru84] and a Kalman filter are used for the extrapolation. They take into account the errors of the tracking to the muon chambers as well as multiple scattering and energy loss of the muon candidates. The tracks are extrapolated starting from the interaction point going outward. This ensures the best treatment for low momentum muons as they lose a significant fraction of their energy before they reach the inner muon chambers.

The algorithm is suited not only for isolated but also for non-isolated muons because no MIP signature in the CAL is required. Therefore also muons included in jets are reconstructed properly. The BREMAT algorithm uses the following cuts as an preselection of the muon candidate:

- track momentum $p > 1\,\text{GeV}$
- track polar angle $\theta > 20^\circ$
- track starting from the first CTD superlayer and reaching at least the third superlayer
- distance-of-closest-approach to the reference point $|D_H| < 10\,\text{cm}$
- z position of the distance-of-closest-approach to the reference point $|z_H| < 75\,\text{cm}$
- χ^2 per number of degrees of freedom $n.d.f.$ of the track fit $\chi^2/n.d.f. < 5$
- distance between a central point on a barrel/rear muon segment and the crossing point of a straight line obtained by continuing the track to the muon chambers $\Delta \leq 150\,\text{cm}$

The track requirement ensures an appropriate acceptance of the CTD. The cut on Δ has been safely set after a study of inclusive muon data samples to accept most of the low energy muons[Gia99].

The extrapolation ends at the reference surface where the match with the muon segments is performed. A muon segment can either consist of hits in the inner muon chambers or, if the muon reached the outer muon chambers, it consists of inner chamber hits and the reconstructed momentum combining inner and outer hits.

MPMATCH

For forward muons, the algorithm equivalent to BREMAT is called MPMATCH [Bel96]. It matches tracks in the forward muon chambers with tracks from the CTD in the overlap region of the CTD and the forward muon chambers.
A muon track reconstructed in the FMUON system is given by five parameters in the ZEUS reference frame: $(x, y, dx/dz, dy/dz, Q/p)$. The match starts with an FMUON track by opening a corridor in the polar angle θ and the azimuth angle φ around the track. The inner tracking detectors are searched for tracks inside this corridor. If at least one CTD track is found, the FMUON track is extrapolated backwards to the z coordinate of the most outer hit of the CTD track. For the extrapolation the GEANT package [Bru84] is used. A fit between the two tracks is performed using a Kalman filter [Kal60]. In the case of more than one CTD track in the corridor, the χ^2 of the fit is used to identify the best match. The procedure is repeated for each track. For the best match, a vertex refit is done for the FMUON track and it is extrapolated backwards to the z coordinate of the vertex. The last step is a fit between the extrapolated FMUON track and the CTD track including the vertex position. MPMATCH is suited also for high momentum non-isolated muons in the forward region but suffers from the low FMUON efficiency and a high momentum threshold.

MUFO: Muon reconstruction using FMUON and BAC

The MUFO reconstruction algorithm matches a track from the forward muon chambers to a track from the CTD similar to MPMATCH. It can use MUBAC for additional background rejection and provides a momentum fit of the muon using the FMUON and CTD information.

The advantages of the MUFO algorithm are similar to the MPMATCH. It represents a sophisticated algorithm including a momentum fit using also the forward muon chambers. The MUFO algorithm is also suited for non-isolated muons. The disadvantages for both algorithms are the limited geometrical coverage due to the restriction to the FMUON-CTD overlap region and a high momentum threshold.

MUBAC: Muon reconstruction in the BAC

The backing calorimeter (BAC) provides a digital (hit) and an analog (pad) readout which are used in combination to reconstruct muons, taking into account the errors on the measurement. The BAC provides a clean muon signature with a larger geometrical coverage than the muon chambers, in particular the bottom part of the detector and the gaps between the forward and barrel muon chambers are covered by the BAC. Due to the amount of material along the trajectory of the muon from the interaction point to the BAC, the momentum threshold on reconstructed muon is high. The minimum p_t of muons in the barrel to reach the BAC is 2 GeV. Muons in the forward region need $p > 2.8$ GeV and in the rear region $p > 1.6$ GeV is required.

The reconstructed BAC muon candidate is matched with a vertex fitted track from the inner vertex detectors by a simple distance-of-closest-approach (DCA) algorithm. A match is required to have a DCA of less than 120 cm. For high quality reconstructed muons, the cut on the DCA is tightened to 50 cm.

MV

The MV algorithm [Kuz00] is a CAL based algorithm, that uses a match of a MIP signature and a track to identify muons. It is designed for isolated muons of $p > 1$ GeV. The MV algorithm evaluates the compatibility of the cluster shape and energy distribution with a MIP signature like a neural-net. MV combines the energy deposit in different CAL sections (EMC, HAC1, HAC2), the number of cells in these sections and the polar and azimuth angle θ and φ and compares these variables to MC samples of muons and hadrons. Based on these quantities, it provides a probability for a MIP to originate from a muon.

MV is also useful for identification of very forward muons without a track because it is able to detect clusters without a track and it has a large geometric coverage with a low momentum threshold. It is only suited for isolated muons due to the large hadronic background for low momentum muons in the CAL. A simpler version of MV is also available at TLT level.

5.8 GMUON: General MUON reconstruction

The different algorithms available in ZEUS can be used separately or in combination to exploit the redundant and complementary components. The GMUON [Gei05] algorithm combines all muon finders mentioned above and provides an overall *quality* of the muon candidate. A high quality means, a high signal to background ratio is to be expected. For lower quality, this ratio decreases, depending on the sample used. GMUON is tuned on an inclusive $b\bar{b}$ MC sample. For this sample the relative signal to background ratio increases by about a factor of two for each quality level. *Signal* means semi-leptonic muons from beauty decay, while *background* refers to all other muon candidates in beauty events. To rely on the quality provided, the hadronic background of the $b\bar{b}$ events should not be much different to the hadronic activity of non-beauty events. The tuning of GMUON did not include background from cosmics or noise in the forward detector. To account for noise in the forward muon chambers, a modification routine for the ORANGE[2] GMUON quality has been applied (5.8.1). Muons of quality 4 and higher are suited for beauty quark analysis, if further cuts are applied to the muon candidates. The detection efficiency of muons from beauty quarks in this analysis is about 11 times higher using muons found by GMUON compared to muons found by BREMAT (requiring inner and outer muon chambers and $P > 0.01$).

[2] ORANGE: Overlying Routine for Analysis Ntuple GEneration, is a program package to produce a reduced data sample including cuts and particle identification

Examples of finder combinations and the resulting GMUON quality are given in Table 5.1 and 5.2. The cut values for the different finders are chosen according to analyses using some of these muon finders separately.

quality	finder combination	CTD match	match prob. or DCA	vtx ass.	MIP prob.	p^μ or η^μ
6	BREMAT 5dof	yes	> 0.01	yes	-	-
	MPMATCH or MUFO	yes	> 0.05	-	-	-
	MPMATCH/MUFO + MV	yes	$> 0.01, < 0.05$	-	> 0.6	$p > 1\,\mathrm{GeV}$
5	BREMAT 4dof + MV	yes	> 0.01	yes	> 0.6	$\|\eta\| > 0.6$
	MUBAC + MV	yes	-	yes	> 0.6	$\|\eta\| > 0.6$
	MUBAC+BREMAT4dof+MV	yes	> 0.01	yes	> 0.6	$\|\eta\| < 0.6$
	MUBAC+BREMAT5dof+MV	yes	> 0.01	no	> 0.6	-
	MPMATCH or MUFO	yes	$> 0.01, < 0.05$	-	-	-
	MUFO good vtx	no		yes	-	-
4	BREMAT 4dof	yes	> 0.01	yes	-	-
	MUBAC	yes	$< 50\,\mathrm{cm}$	yes	-	-
	MUBAC + MV	yes	$< 120\,\mathrm{cm}$	yes	> 0.6	$\|\eta\| < 0.6$
	MUBAC + MIP	yes	$< 120\,\mathrm{cm}$	-	impl.	$p_t > 2\,\mathrm{GeV}$
	MUFO other vtx	no	-	yes	-	-
	MCTS + MV	no	-	no	> 0.6	-

Table 5.1: Default muon quality assignments in ORANGE [Gei05] (quality ≥ 4).

5.8.1 Muon quality modification

Muons in the forward region are detected using the MPMATCH or MUFO finder. These finders rely on the forward muon chambers. The original GMUON quality assignment neglects some sources of background and overestimates the quality of forward muon candidates. The noise in the muon chambers is not included in the simulations but is sometimes high in data. If an arbitrary track is matched to these noisy cells the identification of muons can be faked. In addition, the forward region suffers from secondary particles produced in the magnets. To take this background into account, the default quality is reduced depending on the finders used. The reduction of spurious hits in the forward muon chamber is correlated with the number of detector planes used by the forward muon track fit. For less than five planes, the quality is reduced according to Table 5.3. Also the absence of a hit in the innermost chamber suggests a fake muon and the quality is reduced by one. The quality can be recovered if MUBAC or MV found the same muon candidate. An additional reconstruction in MUBAC increases the quality by one, in the case of MV, the quality is increased by two but only to a maximum of the initial quality. Thus the resulting quality is never higher than before the correction.

quality	finder combination	CTD match	match prob. or DCA	vtx ass.	MIP prob.	p^μ or η^μ
3	MV	yes	-	yes	> 0.95	$p > 1\,\mathrm{GeV}$
	BREMAT 5dof	yes	> 0.01	no	-	-
	GLOMU + MV	yes	implicit	-	> 0.6	-
	MUBAC + MV	yes	$< 120\,\mathrm{cm}$	-	> 0.4	$p > 1\,\mathrm{GeV}$
	MUBAC + GLOMU	yes	implicit	-	-	-
	MAMMA	no	-	-	impl.	-
	MAMMA +CTD	yes	-	-	impl.	-
	MAMMA +vtx	no	-	yes	impl.	-
2	MV	yes	-	yes	> 0.8	$p > 1\,\mathrm{GeV}$
	MCTS	no	-	no	-	-
	BAC	yes	$< 120\,\mathrm{cm}$	yes	-	-
	BREMAT 4dof	yes	> 0.01	no	-	-
	GLOMU	yes	implicit	-	-	-
1	MV	yes	-	yes	> 0.6	$p > 1\,\mathrm{GeV}$
0	MV	-	-	-	> 0.4	$p > 1\,\mathrm{GeV}$
	MIP	yes	-	-	impl.	$p_t > 2\,\mathrm{GeV}$
-1	BREMAT 5dof	yes	< 0.01	-	-	-
-2	BREMAT 4dof	yes	< 0.01	-	-	-
-3	any finder, same track	yes	-	-	-	-
-999	sim. μ,not rec.	-	-	-	-	$p > 1\,\mathrm{GeV}$
						$p_t > .5\,\mathrm{GeV}$
-1000	sim. π/K decay,not rec	-	-	-	-	$p > 1\,\mathrm{GeV}$
						$p_t > .5\,\mathrm{GeV}$

Table 5.2: Default muon quality assignments in ORANGE [Gei05] (quality < 4). These muon candidates are not selected for the final event sample.

For candidates found only by MUBAC, the quality is reduced by one to correct for noise in the BAC.

quality modifier	condition	comment
± 0	number of FMUON planes hit > 4	
-2	number of FMUON planes hit $= 4$	
-4	number of FMUON planes hit < 4	minimal number used: 3
-1	no hit in innermost FMUON chamber	low matching quality
$+1$	(MPMATCH or MUFO) and MUBAC	amplify gain of two identifications
$+2$	(MPMATCH or MUFO) and MV	amplify gain of two identifications
-1	only MUBAC identification	treat noise in BAC

Table 5.3: Modifications to the default muon quality.

HAC2 energy deposit

The rejection of muon candidates produced by noisy muon chambers is important, in particular because this kind of misidentification is not simulated by the MC. If a fake hit in the muon chambers is associated to a track coming from an other particle, usually this particle is not able to reach the second part of the hadronic calorimeter (HAC2). Muons leave a MIP energy deposit in the HAC2. Thus all muon candidates in the forward region without an energy deposit in HAC2 are rejected. In the barrel region the muon probability calculated by the MV finder is used in addition to take into account the passage of muons through gaps in the coverage of the CAL. Only muon candidates without an HAC2 energy deposit and an MV probability $P < 0.01$ are discarded.

5.9 MC muon efficiency correction

5.9.1 Efficiency calculation

The MC simulation of the muon detectors inside ZEUS in not very accurate compared to other detector components. For the cross section measurements of this analysis, the muon detection efficiency is essential and the efficiency in the MC has to be corrected to correspond to the efficiency in data.

To obtain the correction factors, a study has been performed to investigate the difference of detection efficiency of signal muons in MC and in data. This difference has to be derived for all muon detectors used in GMUON to correct each muon candidate individually. The different detector components correspond to individual reconstruction algorithms. The MUBAC algorithm corresponds to the BAC, BREMAT to the barrel/rear muon chambers and MPMATCH and MUFO correspond to the FMUON chambers.

In the first stage, the muon detection efficiency is measured for each of the three detector components in comparison to a forth muon reconstruction of a known efficiency. Furthermore the correction is a function of the muon transverse momentum p_t^μ and its pseudo-rapidity η^μ. The second stage applies the efficiency correction to each muon separately depending on the finder combination used.

The processes selected to study the muon efficiency are the decay $J/\Psi \to \mu^+\mu^-$ and Bethe-Heitler (BH) processes. They are chosen as the source of muons due to their simple and easily selectable topology of two isolated muons. Thus it is adequate to use the MV algorithm as the reference because it is well suited for isolated muons and uses the CAL for the reconstruction which is an independent, well simulated detector component. The shape in momentum and pseudo-rapidity of the selected processes is not needed to be reproduced perfectly by the Monte Carlo. The efficiency is calculated for each bin in p_t^μ and η^μ separately and is independent of the production process. For example, the detection efficiency does not depend on the isolation of the muon, because only the muon traverse the calorimeter and reaches the muon chambers or the BAC. The difference in the track matching probability for isolated and non-isolated muons

usually changes only the GMUON quality within the cut range of 4 to 6. To obtain a clean dimuon sample, the following cuts are applied:

- cut on the global event timing determined by the CAL relative to the bunch crossing: $|T_g| \leq 10\,\text{ns}$ to reject cosmics
- cut on the vertex position:
  - $|z_{vertex}| \leq 50\,\text{cm}$
  - existing measurement of the x and y vertex position
  - $\sqrt{x_{vertex}^2 + y_{vertex}^2} \leq 3\,\text{cm}$
- at least two muons reconstructed with GMUON of a quality of 1 or greater
- maximal two vertex tracks
- at least one dimuon system with:
  - different charge of the two muons
  - invariant mass: $2\,\text{GeV} \leq m_{\mu^+\mu^-} \leq 4\,\text{GeV}$: the large mass window allows muons from different processes, i.e. $J/\Psi \to \mu^+\mu^-$ and some Bethe-Heitler events. The background is sufficiently suppressed by the complete selection.
  - angular distance between the two muons: $\Delta r = \sqrt{\Delta\eta^2 + \Delta\varphi^2} > 0.5$
  - distance in polar angle θ between the two muons: $\Delta\theta = |\theta_{\mu_1} - (\pi - \theta_{\mu_2})| > \frac{\pi}{200}$ to reject perfectly back-to-back cosmic muons
  - distance in azimuth angle φ: $\Delta\varphi = ||\varphi_{\mu_1} - \varphi_{\mu_2}| - \pi| > \frac{\pi}{200}$ to reject cosmics muons
- cut on minimal energy in HAC2 according to Sec. 5.8.1

The MC sample used for the efficiency studies are produced by the GRAPE generator for Bethe-Heitler and J/Ψ events. The number of events in each sample is given in Table 5.4.

sample	selected events	cuts
2003 data	690	
2004 data	9737	
elastic BH MC	19270	2 muons with $5 < \theta < 180$ and $p_t > 0.5$
inelastic BH MC	44715	2 muons with $10 < \theta < 180$ and $p_t > 0.5$
J/Ψ MC	7463	

Table 5.4: Data and MC samples used for muon efficiency correction.

To eliminate a bias from the event trigger, events that are triggered only by muon related triggers are treated carefully. If only one muon triggered the event, it has to

be excluded from the efficiency calculation and only the second muon can be used. For events triggered by both muons each muon is included in this study.

In GMUON, two different configurations are used, denoted *loose* and *tight*. The two configurations are defined by:

- MUBAC: distance cut of the MUBAC hit to the track extrapolated to the BAC $\leq 50\,\text{cm}$ for the tight selection; $\leq 120\,\text{cm}$ for the loose selection
- BREMAT: probability ≥ 0.01 for tight; no cut for loose
- MPMATCH: probability ≥ 0.05 for tight; ≥ 0.01 for loose

For muon candidates found by MV the loose configuration is used while for muons not found by MV the harder cuts of the tight configuration are applied.

The detection efficiencies for BREMAT, MUBAC and MPMATCH are different for muons taken with tight or loose cuts, but do not depend on the detection by MV, i.e. is independent of the isolation of the muon [Gei05]. The dimuon event sample requires a MV hit for all events and thus fulfills the cuts of the loose configuration. The muon candidates in this sample are used to calculate the loose efficiencies in bins of η^μ and p_t^μ comparing MC with data. This procedure is performed separately for muons found by MUBAC, BREMAT or MPMATCH. In a second step the cuts of the tight configuration are applied to events in the dimuon sample to calculate the tight efficiencies for the three finders. As an example the comparison of the efficiency in data and MC for MUBAC is shown in Figure 5.9. The two-dimensional histograms of the MUBAC, BREMAT and MPMATCH correction factors are shown Appendix A.

5.9.2 Efficiency application

The GMUON quality of muons in this analysis is required to be at least 4. For muons in the MC sample without an MV hit, the tight cuts have been applied (compare Tab. 5.1) and the tight efficiencies have to be applied. Thus the lack of an MV hit is the condition to correct the MC efficiency using the tight correction[3]. All MC muons with an MV hit are corrected using the loose efficiency correction.

The efficiency correction is applied to the MC muons by weighting the event. The weight is calculated as the ratio of data to MC efficiency:

$$w = \frac{\epsilon^{data}}{\epsilon^{MC}} \tag{5.15}$$

For muons detected by more than one detector component, the combination of efficiencies for different muon detectors has to be taken into account. For every muon the weight is derived in the specific p_t and η bin for the applicable finder combination (see

[3]for the correction of the inner BREMAT chambers, an additional MUBAC hit is required. The correction for BREMAT outer is set to 0.8 for all η and p_t bins.

Tab. A.1). The weight is the product of finder efficiencies (ϵ) or inefficiencies ($1-\epsilon$) respectively. For details see Appendix A.
The limited statistics of the available MC and data sample requires a coarse binning of the efficiency histograms. Even with this binning the variations of the efficiency correction values from one bin to another are large for the tight configuration. Thus, for the time being, the loose configuration is used for all muons in this analysis. The error of this method is included in the systematical error (see Sec. 8.9).
The entire procedure is checked using distributions of muon finder combinations. The agreement between data and MC is better after applying the muon correction than before. The remaining differences are treated as a contribution to the systematic error.

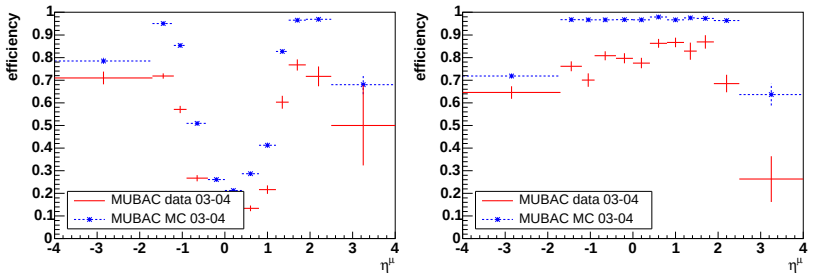

Figure 5.9: Efficiency of data and MC for the MUBAC finder. Shown is the efficiency as a function of η^μ for events of $1.5\,\text{GeV} < p_t^\mu < 1.75\,\text{GeV}$ (left) and $2.5\,\text{GeV} < p_t^\mu < 5.\,\text{GeV}$ (right) in the loose configuration. Most muons with low p_t^μ did not reach the BAC in the barrel region and the detection efficiency is low while at high transverse momentum most muons reach the BAC.

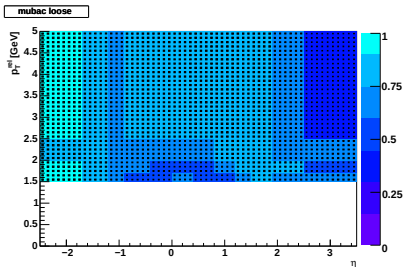

Figure 5.10: Correction factors for the MUBAC finder in the η-p_t plane for the loose configuration. Correction factors for all three finders can be found in Appendix A.

5.10 Jet reconstruction

As described in Sec. 2.3.3, quarks and gluons are not observable directly in a high energy experiment because the confinement of colored particles recombines them via fragmentation/hadronization into colorless hadrons. These hadrons appear as collimated flows of particles called *jets*. The energy and direction of the hadrons can be measured in the experiment. Thus it is possible to measure quarks and gluons indirectly using the strong correlation between the partons of the hard interaction and the reconstructed jets in the detector. In order to draw conclusions between theoretical predictions and experimental results, well defined jets are essential. Therefore a *jet algorithm* defines the jets in experiments and theory. In heavy quark production the jet algorithm should distinguish between the remnant of the proton and the jets from the hard process. To be suited for *ep*-colliders, the jet algorithm has to fulfill the following requirements:

- *collinear safety:* the resulting jets have to be independent of one parton splitting into two partons moving collinearly. Translated to the experimental point of view, the jet algorithm has to be independent of one particle releasing energy in two adjacent CAL cells.
- *infrared safety:* the resulting jets have to be independent of the emission of very low energy particles. Experimentally, this is also related to the noise in the detector.
- correct treatment of beam remnants especially of the proton and eventually of the photon.
- *Lorentz invariance:* independence from longitudinal Lorentz boosts

In this analysis, a k_t*-type clustering algorithm* [Cat92] in the *massive mode* is used to meet these requirements. The clustering approach has the advantage of unambiguously assigning the EFOs to a jet whereas the resolution of the jets depends on the relative transverse momentum of the combined objects. This defines an effective radius depending on the hardness of the jet. The jet clustering is characterized by the following algorithm [Cat92]:

1. the flagged DIS electron EFO is excluded from the list of EFOs for the jet clustering
2. for every object (EFO) i the distance to the beam is calculated as $d_i = E_{t,i}^2$
3. for every pair of objects i, j the distance between each other is defined as $d_{i,j} = \min(E_{t,i}^2, E_{t,j}^2) \cdot ((\eta_i - \eta_j)^2 + (\varphi_i - \varphi_j)^2)$
4. the smallest object in the list $\{d_i, d_{i,j}\}$ is determined
5. if $d_{i,j}$ is the smallest member of the list, the objects i and j are combined into a new pseudo-particle k following the E-recombination scheme. The four-vectors of

both massive objects $\vec{p_i}$ and $\vec{p_j}$ were added according to:

$$E_{t,k} = E_{t,i} + E_{t,j} \tag{5.16}$$

$$\eta_k = \frac{E_{t,i} \cdot \eta_i + E_{t,j} \cdot \eta_j}{E_{t,i} + E_{t,j}} \tag{5.17}$$

$$\phi_k = \frac{E_{t,i} \cdot \phi_i + E_{t,j} \cdot \phi_j}{E_{t,i} + E_{t,j}} \tag{5.18}$$

6. if the smallest quantity in the list is a d_i, the object i is labeled *remnant jet* and is removed from the clustering
7. the procedure is repeated until the smallest object in $\{d_i, d_{i,j}\}$ is above a certain d_{cut} threshold where $\Lambda^2 \ll d_{cut} \ll s$ with the QCD scale Λ and the center-off-mass energy $\sqrt{s}$. For this analysis, d_{cut} is set to $1\,\mathrm{GeV}^2$
8. all pseudo-particles, that are not associated to the remnant jets are called *hard final state jets*

This procedure results in hard final state jets and remnant jets. The E-recombination scheme is favored over other recombination schemes because the massive approach describes the jets of heavy flavor beauty quarks with only small differences between the reconstruction of the detector measurement and the theoretical calculation [Cor04].

5.10.1 Jets in the Breit frame

In order to select events of heavy quark production in BGF processes the jet algorithm is often used in the Breit frame (see Sec. 2.5.3). The four-momenta of all EFOs (except the DIS electron EFO) are boosted to the Breit frame and the clustering algorithm is applied. The final state jets are boosted back to the laboratory frame in order to compare the jet variables with all other event quantities, e.g. for the jet-muon association. For the different jet reconstruction methods used in this analysis, see Appendix C.

5.11 p_t^{rel} calculation

One technique to determine the fraction of beauty events in the data sample is the p_t^{rel} method. This method uses the high mass of the b quark to extract statistically the fraction of signal (events from beauty decay) to background (events originating from charm quark decay or muon candidates in light flavor events). While the mass of charmed mesons, e.g. D^0, is of the order of 1.9 GeV, the mass of beauty mesons is higher than 5.2 GeV. In semi-leptonic decays into muon and jet the quantity p_t^{rel} is a measure for the mass of the heavy quark. p_t^{rel} is the transverse momentum of the muon with respect to the axis of the jet including this muon (see Fig. 5.11). For charm quarks

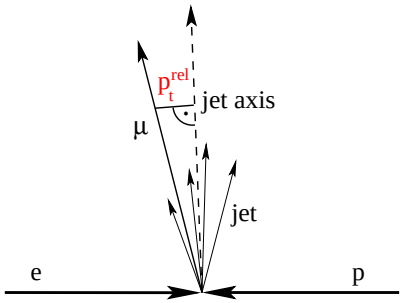

Figure 5.11: p_t^{rel} as the transverse momentum of the semi-leptonic muon with respect to the associated jet.

the p_t^{rel} is statistically lower than for beauty quarks (see Fig. 5.12). The p_t^{rel} of light flavor events is very similar to the charm p_t^{rel}.
The definition of p_t^{rel} used for this analysis is:

$$p_t^{rel} = |\vec{p}_t^{\,\mu}| \cdot \sin\left(\arccos\left(\frac{\vec{p}_t^{\,\mu} \cdot \vec{p}_t^{\,jet}}{|\vec{p}_t^{\,\mu}| \cdot |\vec{p}_t^{\,jet}|}\right)\right) \tag{5.19}$$

To calculate the number of beauty events in the data sample, a χ^2 fit is used. The shape of charm and light flavor events is very similar and a fit is not sensitive to the relative fraction of charm to light and both MC samples are added according to the generated luminosity before the fit procedure.

The number of signal plus background events in MC are normalized to the number of data events N_{data}:

$$N_{data} = P_{signal} \cdot N_{signal} + P_{background} \cdot N_{background}, \tag{5.20}$$

using numbers of generated events scaled to data luminosity N and scaling factors P for signal and background respectively. The P factors are determined by the minimization of χ^2, according to the function:

$$\chi^2 = \sum_i \frac{\left(N^i_{data} - \left(P_{signal} \cdot N^i_{signal} + P_{background} \cdot N^i_{background}\right)\right)^2}{\sigma^2_{i,data} + \sigma^2_{i,background} + \sigma^2_{i,background}} \tag{5.21}$$

where N^i are the numbers of events in each bin i. σ_i are the statistical errors for each bin.

The fraction of beauty events in the total data sample is calculated using the scaling factors from the fit:

$$f_{beauty} = \frac{P_{signal} \cdot N_{signal}}{N_{data}}. \tag{5.22}$$

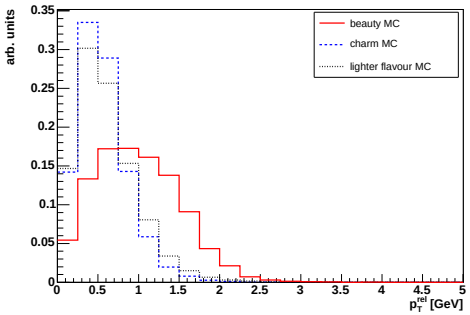

Figure 5.12: p_t^{rel} for beauty, charm and light flavor MC. The distributions for charm and light flavor peak at lower p_t^{rel} values than the beauty MC.

For the beauty quark cross section determination, the number of beauty event in data are needed. Therefore the scaled number of MC beauty events is used:

$$N^{data}_{beauty} = P_{signal} \cdot N_{signal} = f_{beauty} \cdot N_{data} \tag{5.23}$$

The relative statistical error of the *beauty fraction* is approximated as the error or the χ^2 fit:

$$\frac{\sigma_{f_{beauty}}}{f_{beauty}} = \frac{\sigma_{P_{signal}}}{P_{signal}} \tag{5.24}$$

with the absolute errors on the beauty fraction and beauty scaling factor f_{beauty} and P_{signal} respectively. This method assumes a $\chi^2/n.d.f.$ near 1.

5.12 p_t^{rel} correction

As the p_t^{rel} distribution of the background is essential to calculate the beauty fraction, investigations of the correct simulation of p_t^{rel} distributions have been conducted. In [Gut05] a procedure is described to compare the p_t^{rel} distribution of an inclusive data sample with MC. That analysis used the PYTHIA Monte Carlo generator in the photoproduction regime. There the p_t^{rel} distribution of light flavor events is softer in MC than in data and a correction of the MC p_t^{rel} shape has to be applied.

As shown in [Che04b], the p_t^{rel} description of HERA I data with the RAPGAP DIS MC is reasonable and no correction is necessary. For HERA II such an inclusive data sample is not yet available. For the ARIADNE MC sample, used in this analysis to simulate the light flavor background, the same check will be made, as soon as the required samples are produced. A rough comparison of light flavor RAPGAP MC and ARIADNE MC for HERA I result in a similar p_t^{rel} description of both MC generators. Thus, no change of the p_t^{rel} simulation is applied for this analysis yet.

5.13 Impact parameter method

The other quantity apart from the high mass to distinguish beauty and background, is the relative long lifetime of beauty mesons. The lifetime can be translated to a measurable quantity using the decay length of the boosted hadron:

$$l = c\tau\beta\gamma, \tag{5.25}$$

where τ is the lifetime in the particle rest frame and $\beta\gamma = |\vec{p}|/m$ denotes the boost of the particle relative to the laboratory frame. The boost of the lighter charm meson is higher for a given CMS energy and the decay length in the laboratory system can be larger than the decay length of beauty mesons. But the larger decay angle of beauty quarks results in a higher significance of the distance-of-closest-approach of the decay muon track to the beam-spot in the xy-plane, called *impact parameter* δ. In addition a sign is defined, using the jet including the muon (see Fig. 5.13). A positive sign means, that the muon crosses the jet, while a negative sign is used if the track passes the beam-spot on the direction opposite to the jet. Muons originating from a process at the beam-spot are expected to deliver impact parameters distributed symmetrically in positive and negative signs around the beam-spot. The width of the distribution is related to the detector resolution. Muons from long living hadrons are expected to produce a impact parameter distribution tending towards positive values, because the hadron momentum sets the boost of the decay products and in this way favors the muon direction to be similar to the jet direction.

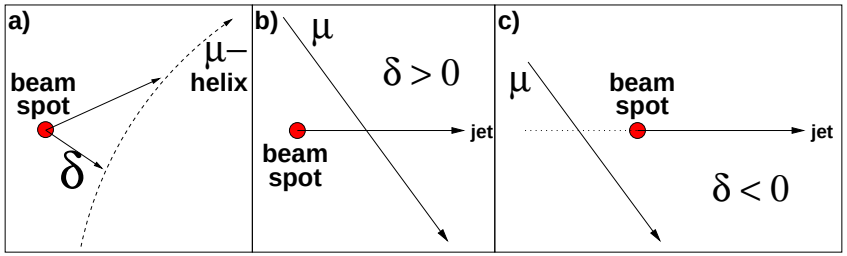

Figure 5.13: Definition of the impact parameter and its sign.

The impact parameter for beauty hadrons is in the order of tens to hundreds of micrometers. To resolve these distances, a high precision track measurement is required. Only in the HERA II period this resolution is provided by the MVD. This method is still not settled and is used in this analysis only as a cross check for a clean data sample and is not included in the data selection described in Section 7. To make use of the highest resolution for impact parameter studies the following cuts are applied in addition to all other selection cuts:

- number of CTD superlayers used $n_{\mathrm{SL}} \geq 3$

- reference point of the helix $|z_H| < 30\,\mathrm{cm}$
- number of MVD hits used $n_{\mathrm{MVD-hits}} \geq 4$

To reduce the background of events with a symmetric impact parameter, the negative part of the distribution is mirrored and subtracted from the positive part. Thus only the excess of positive impact parameters is left. This excess is proportional to the number of beauty and charm decays. As the impact parameter of charm is significantly smaller, the distribution can be used to fit the beauty to charm ratio in the data sample. Due to the reduced data sample used for this measurement, the fit is not reliable and only the distribution is shown in this analysis. For a larger data sample and a better understanding of the MVD, the impact parameter method could be used in a combined fit with the p_t^{rel} method. That would provide information about the fraction of light flavor events, charm and beauty events separately.

Chapter 6

Data and MC sample

6.1 Data sample

The data sample used for this analysis covers data, that were taken 2003 and 2004 in the HERA II period. This corresponds to a luminosity taken in ZEUS of $39.7\,\mathrm{pb}^{-1}$. The ntuples were produced with the software package ORANGE version 2004a.2 with some additional modifications. The default tracking is set to regular tracking. The data of the 2005 period are also available, but the corresponding MC is not yet generated.

Data taking period	Luminosity	Leptons
2003	$2.08\,\mathrm{pb}^{-1}$	e^+
2004	$37.63\,\mathrm{pb}^{-1}$	e^+
2005	$92.72\,\mathrm{pb}^{-1}$	e^-

Table 6.1: Configuration of the data samples. Luminosity for 2005 up to Sept. 6th.

6.1.1 Background

This analysis concentrates on the selection of muons to gain a clean sample of beauty events. The background of the muon selection comes from different processes. The semi-leptonic decay of charm quarks, not originating from beauty quarks, produces real muons. For this source of background, a dedicated charm MC sample has been produced.

The processes with only light quarks (u,d and s) involved can either produce real muons or fake the muon signature:

in-flight decays: particles like $\pi^\pm$ or $K^\pm$ decay with a $c\tau = 7.8\,\mathrm{m}$ or $c\tau = 3.7\,\mathrm{m}$ respectively. Thus they can decay within the detector and produce muons, e.g. in the reaction: $\pi^+ \to \mu^+\nu_\mu$ or $K^- \to \mu^-\bar{\nu}_\mu$. The momentum of these muons is in average low compared to signal muons and their rate is reduced by the p_t^μ cut.

punch-through: hadrons can produce secondary particles inside the CAL that leave the CAL and produce signals in the muon detectors.

sail-through: occasionally particles do not interact inside the CAL and are able to hit the muon detectors. The material in front of the muon chambers varies between 4 and 5 interaction lengths λ. The probability of particles not interacting with the material of thickness d in interaction length is given by:

$$P(d) = e^{-\frac{d}{\lambda}} \tag{6.1}$$

the probability of hadrons to traverse the CAL without interaction only is about 1% but the total number of events containing hadrons is very high.

To account for these processes an inclusive DIS MC is used after exclusion of events containing charm or beauty quarks to avoid double counting.

The MC samples used as signal and background simulation are generated by RAPGAP for beauty and charm samples and ARIADNE for the light flavor events (see Sec. 6.2). The different trigger configurations used for data taking are assigned to five configurations of the MC detector simulation. The luminosity of the data samples is taken to generate the MC samples accordingly. An overview of MC used in this analysis is given in Table 6.2. Due to the high cross section of the inclusive DIS sample, about 780

Process	Cross section	MC generator	Luminosity	Cuts
$ep \to b\bar{b}X$	0.908 nb	RAPGAP	990.61 pb^{-1}	$Q^2 > 1\,\mathrm{GeV}^2$
$ep \to c\bar{c}X$	90.03 nb	RAPGAP	100.27 pb^{-1}	$Q^2 > 1\,\mathrm{GeV}^2$
inclusive DIS	709.0 nb	ARIADNE	38.34 pb^{-1}	$Q^2 > 1.5\,\mathrm{GeV}^2$

Table 6.2: Configuration of MC samples.

times higher than the cross section of the signal MC, the generated sample is relatively small. The luminosity matches the data luminosity. The most time consuming part in production of a MC sample is the detector simulation FUNNEL and for further studies the inclusive MC has to be expanded.

To estimate the background from photo-production, a PYTHIA MC is used (see Tab. 6.3). To eliminate double counting a $Q^2_{\mathrm{true}} < 4$ cut is applied before the selection cuts. The number of beauty events after all cuts scaled to $\mathcal{L}_{\mathrm{data}}$ is only 4 events. This contribution is therefore neglected.

PHP Process	Cross section	MC generator	Luminosity
$ep \to b\bar{b}X$			
direct	4103.05 nb	PYTHIA	402.12 pb^{-1}
resolved	70815.51 nb	PYTHIA	389.49 pb^{-1}
exphoton	74485.12 nb	PYTHIA	409.67 pb^{-1}
exproton	410.18 nb	PYTHIA	426.65 pb^{-1}

Table 6.3: Configuration of background PHP MC samples.

6.2 Monte Carlo programs

The Monte Carlo program used in this analysis to generate *ep*-scattering events in the DIS regime is the RAPGAP [Jun95] event generator. It is used to generate beauty events as signal and charm events as a source of background.
The background from light flavor events is simulated using DJANGOH [Sch91], an interface between HERACLES [Kwi91, Kwi96] and ARIADNE [Lön92].

The HERACLES program, used by RAPGAP and DJANGOH, simulates the *ep*-scattering in DIS, including first order radiative corrections. The hard scattering between the parton and the photon is simulated according to the Standard Model cross sections and the proton PDFs. The parameterization of the PDF is chosen according to the CTEQ5 [Kuh99] set of proton PDFs.

RAPGAP is used for QCD corrections in order to simulate the complete *ep*-scattering process. The first order QCD processes are simulated using the exact matrix elements. These processes are the QCDC process and the BGF process. For higher order corrections, QCD parton showers, based on the *leading log* DGLAP [Alt77, Gri72, Lip75, Dok77] splitting functions are used. They can occur before and after the hard subprocess.

For the fragmentation, RAPGAP uses the Lund-string model, as it is implemented in JETSET/ Pythia [Sjo01] (see Fig. 6.1).

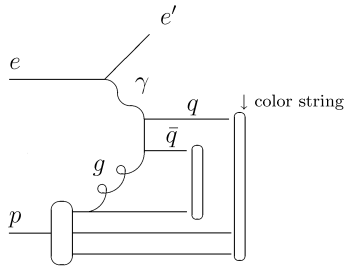

Figure 6.1: RAPGAP implementation of BGF. Shown are the color strings and the proton remnant in Boson-gluon-fusion of $O(a^{em}a_s)$. The proton remnant is the valence quark and valence diquark.[Jun95]

ARIADNE uses the color dipole model (CDM). In this model, gluon emissions from a $q\bar{q}$ pair are treated as radiation from the color dipole between the quark and the antiquark. This model incorporates BGF as an extra process, while QCDC is included in the color dipole radiation.
Like RAPGAP, also ARIADNE uses the Lund-string model for hadronization.

The MC predictions are not expected to describe the absolute number of events in the data. The normalization is usually taken from the comparison to the data. The MC sample is expected to describe the differential distributions in different variables in agreement with the data. In order to exclude effects, knowingly not simulated in the MC programs, e.g. cosmic muons in the detector, the event selection (see Sec. 7) cleans the event sample and brings the control distributions well under control.

Chapter 7

Event Selection

To select candidates for beauty production in DIS the first step is the restriction to DIS using the Sinistra electron finder and CAL properties. The semi-leptonic decay into a muon and a jet is selected by the requirement of at least one muon with a given quality from GMUON and a jet containing this muon. These steps and additional cuts to improve efficiency and purity are explained in detail in this chapter.

7.1 Pre-selection

The raw ZEUS data are processed using ORANGE in order to produce a reduced dataset of pre-selected data. The cuts require at least one muon with a GMUON quality greater or equal four (see Sec. 5.8). For the Monte Carlo sample, the same cut on reconstructed quantities is required or at least one true muon from a semi-leptonic beauty decay even if it is not reconstructed in the detector simulation. The true muon is necessary for the cross section calculation (see Sec. 8).

The control histograms shown in this chapter are distributions of events passing the pre-selection cuts and all selection cuts. Distributions demonstrating a cut on one variable, are populated with events passing cuts on all variables but not the shown one.

The distributions are comparisons of data and Monte Carlo events. The MC is normalized to the data and the relative fraction of signal to background MC is taken from a p_t^{rel} fit (see Sec. 5.11).

The indicated errors of the data points are statistical errors only. The statistical error on beauty and charm MC is much smaller, but the generated luminosity of the light flavor background MC is similar to the data luminosity. Thus the statistical error of the MC is approximately the same as of the data.

7.2 Trigger pre-selection

No explicit selection of triggers is used for this analysis. A combination of four TLT trigger slots for DIS events, as mentioned in Sec. 5.2 is used to study a possible bias of

the trigger selection. Over 99% of the MC events fulfilling all selection cuts are triggered by at least one of the four trigger slots. Even in the low Q^2 region the trigger efficiency is so high, because the requirement of a measured DIS electron in the selection is also the requirement for the DIS trigger slot. Thus, an explicit trigger selection is not needed.

7.3 General event requirements

The maximal total transverse momentum of the EFOs (Sec. 5.6.1) is required to be $p_t^{miss} < 10\,\text{GeV}$ to reject unbalanced events, e.g. CC DIS where a high fraction of the transverse momentum is not detected in the CAL.

The total transverse hadronic energy, measured in the CAL outside of a 10° cone around the beam pipe in the forward region is required to be $E_{t,cal} > 7.5\,\text{GeV}$. The energy of the DIS electron is excluded from this calculation (see Fig. 7.1).

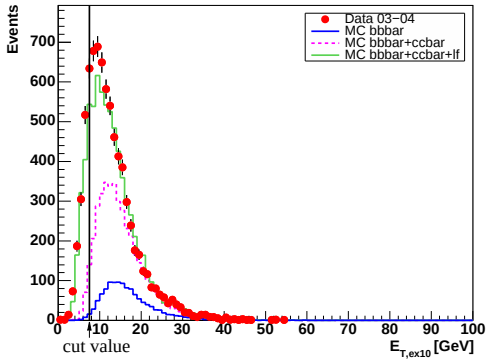

Figure 7.1: Control distribution of $E_{t,cal}$ outside of a 10° cone around the beam pipe without the DIS electron. A cut at 7.5 GeV rejects mainly background events. The 03/04 data are indicated by the red dots, the MC of the beauty signal is shown as a dark blue line, a magenta dashed line indicates charm background MC added to the beauty MC. The light green line is the sum of light flavor, charm background and beauty MC. The MC is normalized to the number of events in data. The relative fraction of signal to background is determined by a p_t^{rel} fit, described in Section 5.11

7.4 DIS selection

In DIS events the quantity δ_{had} (see Sec. 5.5) is within detector resolution (neglecting undetectable particles) double the electron energy, i.e. 55 GeV. The selection cut is chosen to require $40\,\text{GeV} < \delta_{had} < 65\,\text{GeV}$. Figure 7.2 shows δ_{had} (using EFOs) for

data in comparison to the sum of the MC samples. Due to the shift in MC w.r.t. data, the cut values are chosen to be relatively loose. Otherwise, the systematic difference between data and MC in the final sample would increase. To select a sample with a

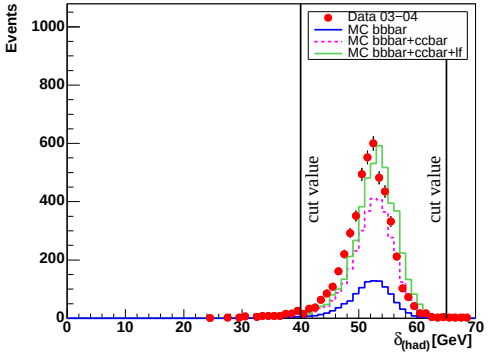

Figure 7.2: Control distribution $\delta_{had,efo}$ after applying all cuts except for the $\delta_{had,efo}$ cut. The MC description is shifted towards higher energies. The cut values are chosen to reject the poorly reconstructed tails of the distribution.

reliable measurement of the kinematic variables, a Sinistra electron has to be found, meeting the following requirements:

- Sinistra probability > 0.9
- $E_{el} > 10\,\text{GeV}$
- $Q^2_{el} > 4\,\text{GeV}^2$
- $y_{jb} > 0.05$ and $y_{el} < 0.7$

The cut on Q^2 is higher than in previous analyses for HERA I data, because the calorimeter around the rear beam pipe was moved outwards for the upgrade of HERA. The minimal measurable Q^2 therefore increased to higher values. Figure 7.3 shows the distribution of the photon virtuality. The Q^2 cut is set to 4 GeV because for lower Q^2 the electron acceptance is highly xy position dependent due to the asymmetric rectangular aperture of the CAL (see Fig. 7.4).

The electron energy is shown in Figure 7.5. A shift of data towards lower energies is clearly visible. This might be due to a incomplete description of the inactive material between the interaction point and the CAL. A similar underestimation of material in HERA II is seen in other distributions, most prominent in the multiplicity of not vertex associated tracks (Fig. 7.17). To keep the influence on acceptance small, all cuts on affected variables are chosen conservatively.

The kinematic variables Bjørken x and y are shown in Figure 7.6. The inelasticity cut is applied to the y_{el} value, reconstructed with the electron method (see Sec. 5.5) for the higher cut at 0.7 and to the Jacquet-Blondel y_{jb} for the lower cut at 0.05 to gain high measurement precision.

The distribution of data events in the kinematic plane of Q^2 and x is shown in Figure 7.7.

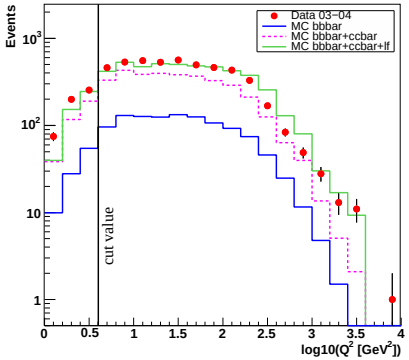

Figure 7.3: Control distribution of Q^2_{el}. The explicit cut is set to $Q^2_{el} > 4\,\text{GeV}^2$. The data is overestimated by the MC in the region $300\,\text{GeV}^2 < Q^2_{el} < 1000\,\text{GeV}^2$.

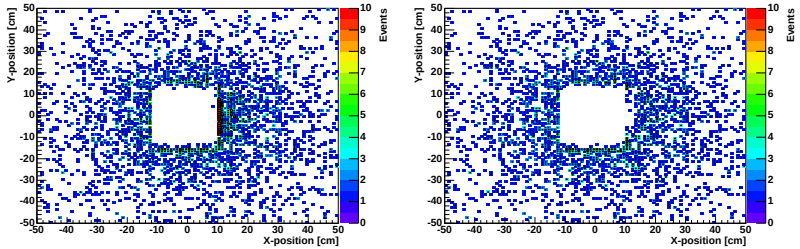

Figure 7.4: Distribution of the electron position in xy at the z position of the RCAL surface. No explicit position cut is applied but the minimal Q^2 cut is related to the electron xy position. The left histogram shows all 03/04 data events without an explicit Q^2_{el} cut. On the right, the cut is set to $Q^2_{el} > 4\,\text{GeV}^2$.

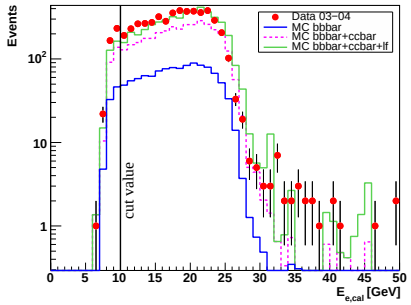

Figure 7.5: Control distribution of the DIS electron energy E_{el} with a cut of $E_{el} > 10\,\text{GeV}$

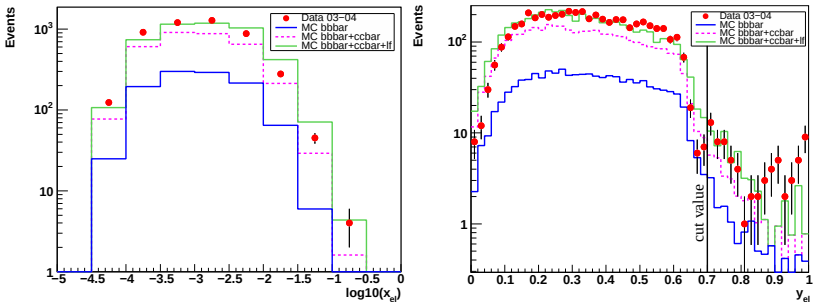

Figure 7.6: Distribution of Bjørken x_{el} and inelasticity y_{el}. The cuts on y are applied to y_{el} for the higher cut. The cut on y_{jb} for the lower y cut is not shown here.

7.5 Muon selection

For this analysis a sophisticated muon selection is essential to gain a high selection efficiency of both kinematic region and detector area.

The detector is divided into three regions of pseudo-rapidity η: the forward region ($\eta > 1.3$), the barrel region ($1.3 < \eta < -0.9$) and the rear region ($\eta < -0.9$).

At least one muon candidate found by GMUON (see Sec. 5.8) with a quality of at least four after the forward quality correction applied is required. In addition, a minimal transverse momentum $p_t^\mu > 1.5\,\text{GeV}$ is required to exclude the low efficiency and high background region. The muon selection requires implicitly a muon vertex-track, due to the EFO association (see Sec. 7.7).

As explained in Sec. 5.8.1, a muon candidate has to deposit energy in the HAC2 section of the CAL, to be considered as a muon. The cuts applied are:

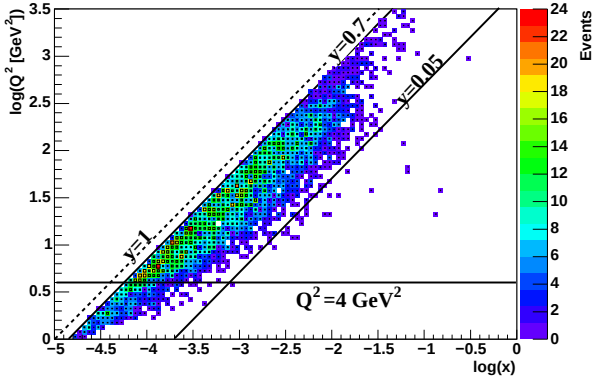

Figure 7.7: Kinematic plane $\log Q^2$ vs. $\log x$. Cuts in Q^2 and y are applied to the event sample.

- Forward region: Energy loss in HAC2 $> 0.4\,\text{GeV}$
- Barrel region: Energy loss in HAC2 $> 0.3\,\text{GeV}$ or a non-zero MV probability.

The MV selection is used, because MV takes into account also regions where a muon can traverse the CAL without leaving a MIP signature (e.g. cracks between CAL towers). The HAC2 distributions are shown in Figure 7.8. The poor MC simulation of the HAC2 energy deposit, especially for the forward region should be improved in the future. The effect on the acceptance is small due to the conservative HAC2 cuts. In order to suppress events with a very noisy BAC, the Number of BAC hits is required to be lower than 14.

The angular distribution of muons (see Fig 7.9) shows good correlation between data and MC. The acceptance dip at $-2 < \varphi < -1$ (bottom area of ZEUS) is due to the incomplete coverage of the muon chambers.

The transverse momentum of the muon (see Fig 7.10) is well described by the MC up to the highest p_t^μ.

The muon efficiency correction (see Sec. 5.9) is applied by assigning a weight to the muon. The weight of the event is determined from the weight of the muon associated to a jet (see Fig. 7.11). The number of muons found by different muon finders after the efficiency correction is shown in Figure 7.12. The difference of MC muons compared to muons in data for the different muon finders is much smaller after the correction. The remaining differences are treated as a contribution to the systematic error for the cross section measurement. Distributions for muon finder combinations are shown in Appendix A.

Summery of muon selection cuts:

- GMUON quality ≥ 4

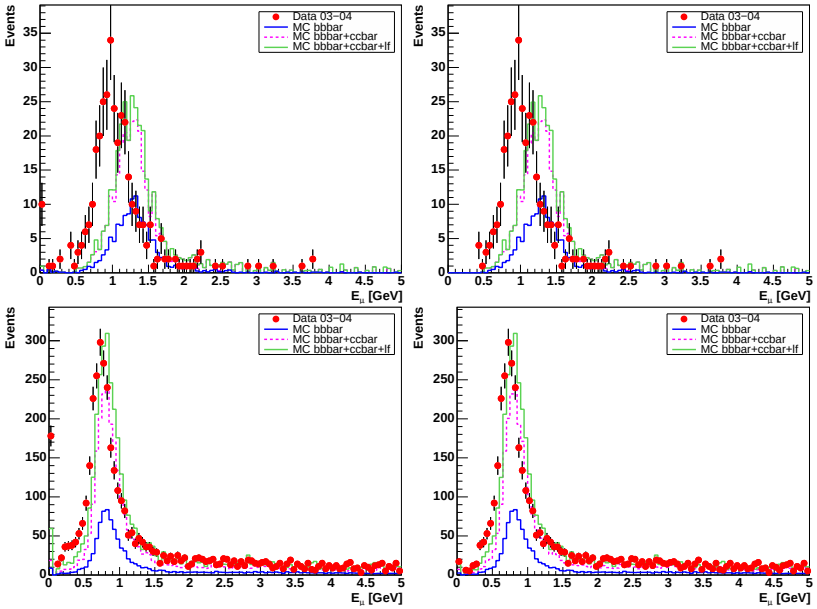

Figure 7.8: Control distribution muon HAC2 energy for the forward region (upper histograms) and the barrel region (lower line). The left histograms show the poorly simulated contribution of muon candidates with very low HAC2 energy deposit. The histograms on the right show the distribution after the HAC2 cut applied. A 0.3 GeV shift of forward MC HAC2 energy towards lower values is obvious. The shift in the barrel region is smaller but significant.

- $p_t^\mu > 1.5\,\text{GeV}$
- $\eta^\mu > -1.6$

7.6 Jet selection

The jet selection requires at least one jet, reconstructed in the laboratory frame. Alternatively one jet in the Breit frame can be required.

Jets are reconstructed using the KTCLUS algorithm on the corrected list of EFOS without the DIS electron (see Sec. 5.6.1). The transverse energy of the jet has to exceed $E_t^{lab} > 5\,\text{GeV}$ in the pseudo-rapidity range of $-2 < \eta < 2.5$.

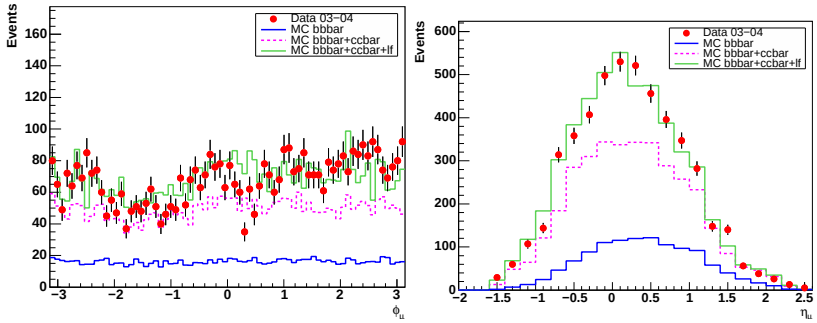

Figure 7.9: Control distribution of φ^μ (left) and η^μ (right).

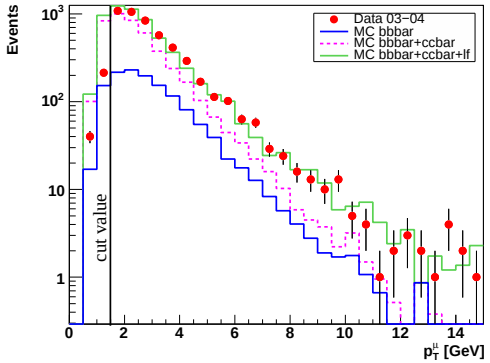

Figure 7.10: p_t^μ distribution. A cut at 1.5 GeV is chosen to reject the low p_t contribution. Due to high fluctuations in the muon efficiency correction in the region below $p_t < 1.5\,\text{GeV}$ the muon distribution below this cut is expected to be poorly simulated.

Figure 7.13 shows the number of jets per event. The reasonable MC description of higher multiplicities is a measure for the quality of the matrix element plus parton shower approach to simulate higher order effects.

The distributions of the jet angle are shown in Figure 7.14. Only jets are counted, where a muon is associated to the jet. Thus the angular distributions of jets are highly correlated to the muon distributions of Fig. 7.9.

The distribution of jet masses (see Fig. 7.15) in data is described by MC quite accurate to the highest masses.

All jet cuts, that are applied:

- one jet reconstructed in the laboratory frame

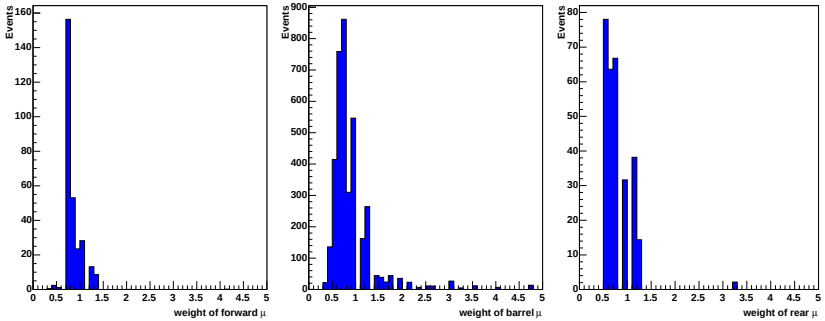

Figure 7.11: Weights of the muon efficiency correction for the forward, barrel and rear region (from left to right). The correction is applied to all MC events.

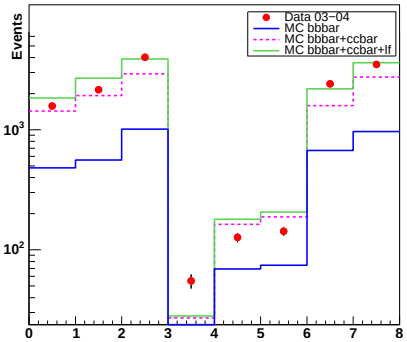

Figure 7.12: Muon finders used to identify muons. The different finders are: GLOMU (1st bin), BREMAT (2.), MUBAC (3.), MAMMA (4.), MPMATCH (5.), MUFO (6.), MIP (7.), MV (8.)

- $E_t^{jet,lab} > 5\,\mathrm{GeV}$
- $-2 < \eta^{jet} < 2.5$

In order to calculate jet cross sections, not only the reconstruction of jets from reconstructed EFOs is necessary, but for MC events jets are reconstructed also from hadrons. Therefore stable final state hadrons on MC generator level are used as input for the jet algorithm. All B hadrons are defined to be stable particles for true MC jets. A comparison of jets from hadrons and EFOs is given in Figure 7.16. The correlation of p_t^{jet}(EFO) and $p_t^{jet}(hadron)$ is good (RMS about $0.2{\cdot}p_t(hadron)$). The distribution of η^{jet}(EFO) compared to $\eta^{jet}(hadron)$ is centered around zero with a RMS of 0.2.

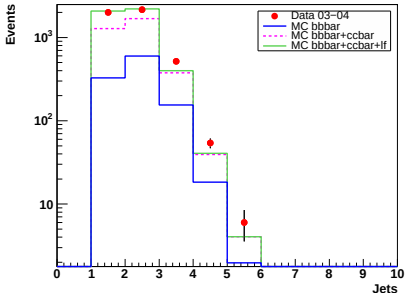

Figure 7.13: Number of jets per event. At least one jet meeting the jet cuts is required, other jets in a event only need to satisfy the looser cuts of the KTCLUS algorithm.

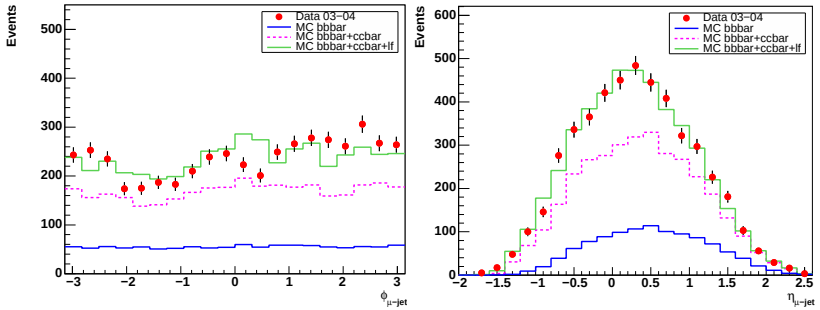

Figure 7.14: Control distribution of φ^{jet} and η^{jet} for jets associated to a muon.

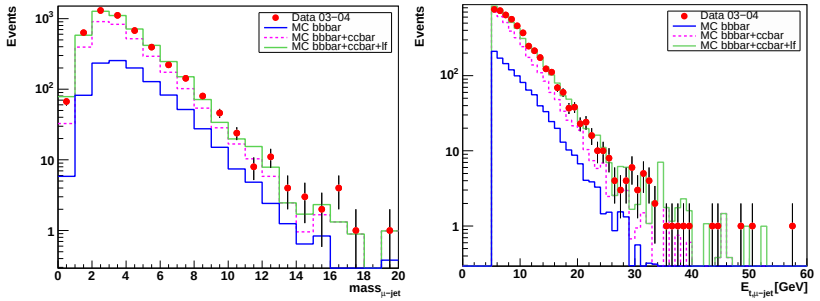

Figure 7.15: Mass and E_t of the jet associated to a muon after all selection cuts applied.

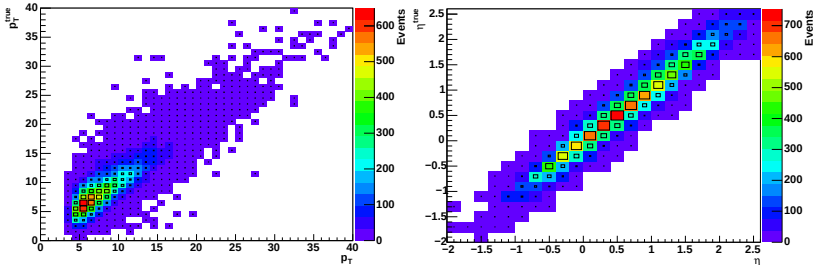

Figure 7.16: True versus reconstructed jet quantities p_t^{jet} (left) and η^{jet} (right). Shown are beauty MC events passing all selection cuts. The cut on reconstructed $E_t^{jet} > 5\,\text{GeV}$ is clearly visible in the p_t^{jet} distribution.

Events from beauty decays contain high numbers of charged particles inside jets coming from the event vertex. Figure 7.17 shows the multiplicity of vertex tracks and of all tracks per event. The data distribution, in particular for all tracks, is clearly shifted towards higher values with respect to the MC predictions. This feature is probably caused by an underestimation of secondary interactions in dead material. Thus, only a conservative requirement of at least 8 tracks is applied in this analysis, in order to avoid to cut differently on data and MC. In the future, a track cut should be applied to vertex associated tracks, to be more reliable.
The difference in track multiplicity for charm and light flavor MC seems to be a possibility to fit the charm and light flavor background separately. But it has to be checked, that the difference is not only due to differences between RAPGAP (used for beauty and charm) and ARIADNE (light flavor).

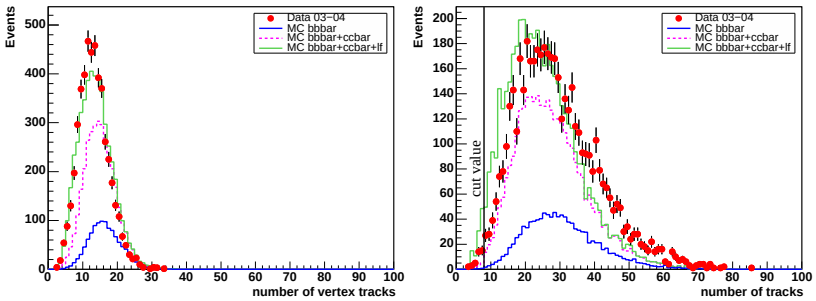

Figure 7.17: Track multiplicity of vertex tracks (left) and all tracks (right). The distribution of total track multiplicity is shifted in data compared to MC towards higher values. A minimal number of 8 tracks is required by the selection cuts.

7.7 Jet-Muon association

To select semi-leptonic beauty quark decays into a muon and a jet, the muon has to be contained in the jet. The muon has to pass the muon cuts and the muon EFO has to be part of a jet, meeting all jet cuts. A source of background is the reconstruction of an isolated muon as a jet associated to itself. These jets consist mainly of the muon and a cut of $p_t^{\mu} - E_t^{jet}$ removes them. The transverse jet energy originating not from the muon is required to be at least 0.7 GeV. The fraction of muon p_t to jet E_t is shown in Figure 7.18. In this distribution isolated muons would contribute to values near 1.
The additional cuts for the jet muon association are:

- $E_t^{jet} - p_t^{\mu} < 0.7\,\text{GeV}$

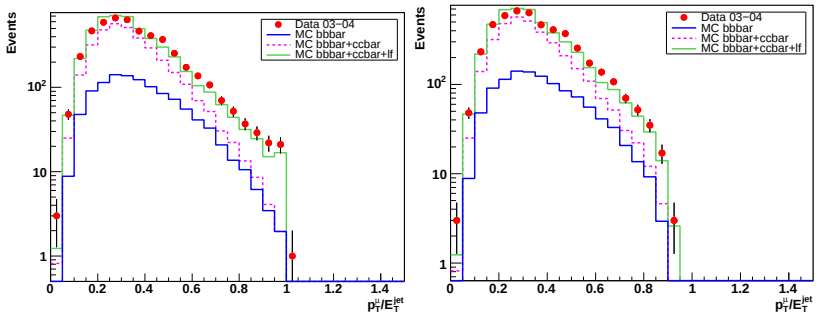

Figure 7.18: Muon p_t over jet E_t. Without a $E_t^{jet} - p_t^{\mu}$ cut (left) and after the cut (right).

An overview of all cuts applied to the data is given in Table 7.1. After these selection cuts, a sample of 4734 events remains.

category	cut value
DIS selection	Sinistra probability > 0.9
	$Q^2_{el} > 4\,\mathrm{GeV}^2$
	$E_{el} > 10\,\mathrm{GeV}$
	$y_{jb} > 0.05$ and $y_{el} < 0.7$
	$40\,\mathrm{GeV} < \delta_{had} < 65\,\mathrm{GeV}$
muon selection	GMUON quality ≥ 4
	$p_t^\mu > 1.5\,\mathrm{GeV}$
	$\eta^\mu > -1.6$
jet selection	$E_t^{jet,lab} > 5\,\mathrm{GeV}$
	$-2 < \eta^{jet} < 2.5$
muon-jet association	$E_t^{jet} - p_t^\mu < 0.7\,\mathrm{GeV}$
track multiplicity	$n_{tracks} > 8$
missing transverse momentum	$p_t^{miss} < 10\,\mathrm{GeV}$
CAL energy outside 10° cone	$E_{t,cal} > 7.5\,\mathrm{GeV}$

Table 7.1: Summery of the selection cuts.

7.8 Selection criteria of a restricted analysis

In order to compare measurement directly with the previous analysis [Che04b], the selection cuts for muons and jets are modified for the so-called *restricted analysis*:

- one muon (GMUON quality ≥ 4) with
  $-1.6\,\mathrm{GeV} < \eta^\mu < -0.9\,\mathrm{GeV}$ with $p^\mu > 2\,\mathrm{GeV}$ or
  $-0.9\,\mathrm{GeV} < \eta^\mu < 1.3\,\mathrm{GeV}$ with $p_t^\mu > 2\,\mathrm{GeV}$
- one jet reconstructed in the Breit frame with
  - $E^{jet}_{t,Breit} > 6\,\mathrm{GeV}$
- one muon associated to a jet of $E^{jet}_{t,Breit} > 4\,\mathrm{GeV}$

All other cuts are the same as defined in Table 7.1.

Chapter 8

Cross section measurement

This chapter describes the measurement of the DIS cross section of beauty quark production and decay into muon and jet. As a comparison to the previous analysis (see Sec. 3.3.4), the cross section is first measured in the same kinematic region, with jets in the Breit frame. After this measurement, the jet reconstruction in the laboratory frame is used to extend the accessible phase space. In addition, the muon selection is extended to the forward region of the detector and to lower transverse momenta. The visible and differential cross sections are presented. Furthermore, as the main step towards a determination of the beauty contribution to F_2, double differential cross sections are measured. Finally, the systematic uncertainties for all measurements are determined.

8.1 Determination of cross sections

The cross section σ of a process b is defined as number of events from this process N_b per integrated luminosity $\mathcal{L}$:

$$\sigma_b = \frac{N_b}{\mathcal{L}}. \tag{8.1}$$

In order to measure the cross section of the process

$$e\,p \to e\,b\bar{b}\,X \to e\,\mu\,jet\,X' \tag{8.2}$$

in DIS, the fraction of events in the data event sample coming from this process has to be determined. The cross section of beauty quark production σ_b is defined as:

$$\sigma_b = \frac{N^{\mathtt{data}} \cdot f_b}{\mathcal{L} \cdot \mathtt{acc}} \tag{8.3}$$

where $N^{\mathtt{data}}$ denotes the number of selected events in the data sample and f_b is the fraction of beauty events in this sample. f_b is determined by a p_t^{rel} fit of MC generated beauty events against MC background events to the data (see Sec. 5.11). The acceptance $\mathtt{acc}$ is the number of events defined as true (generator level) $N^{\mathtt{true}}$, divided by the

number of reconstructed events (not necessary also true events) $N^{\mathtt{rec}}$:

$$\mathtt{acc} = \frac{N^{\mathtt{rec}}}{N^{\mathtt{true}}} \tag{8.4}$$

To have a measure of the extrapolation from reconstructed events to true events, the purity is defined. It is the fraction of true events in the reconstructed event sample:

$$\mathtt{purity} = \frac{N^{\mathtt{rec} \wedge \mathtt{true}}}{N^{\mathtt{rec}}} \tag{8.5}$$

where $N^{\mathtt{rec}\wedge\mathtt{true}}$ is the number of true events which are reconstructed and $N^{\mathtt{rec}}$ is the number of reconstructed events.

For cross sections, differential in one variable, e.g. Q^2, p_t^μ or η^μ, the fit procedure has to be repeated separately for p_t^{rel} distributions containing only events of one bin of the designated variable.

8.2 Definition of the visible signal region

To determine the fraction of signal events in the event sample after applying all selection cuts (see Chapter 7), the Monte Carlo, defined in Section 6.2, is used. All events containing a beauty quark or anti-quark, a muon and a jet in a given kinematic range are defined as signal. The kinematic range is chosen to reflect the regions were the event selection provides reasonable acceptance ($\mathtt{acc} \gtrsim 30\%$ in every bin). For the main analysis in this thesis (called *extended analysis*), the following cuts are applied to MC quantities:

- $Q^2 > 4\,\mathrm{GeV}^2$
- $y > 0.05$
- $y < 0.7$
- one MC jet originating from a beauty quark is required to be found in the laboratory frame. The k_t algorithm in the massive scheme is used to cluster jets from stable final state particles (including B hadrons):
  - $E_{t,lab}^{jet} > 5\,\mathrm{GeV}$
  - $-2 < \eta^{jet} < 2.5$
- a muon originating from a beauty quark decay (direct or indirect):
  - $p_t^\mu > 1.5\,\mathrm{GeV}$
  - $\eta^\mu > -1.6$

The cuts for the restricted analysis correspond to the cuts of the previous analysis, given in Section 3.3.4:

- $Q^2 > 2\,\mathrm{GeV}^2$
- $y > 0.05$
- $y < 0.7$
- one jet with:
  - $E^{jet}_{t,Breit} > 6\,\mathrm{GeV}$
  - $-2.0 < \eta^{jet}_{lab} < 2.5$
- one muon originating from beauty quark decay (direct or indirect) associated to a jet with:
  - $-0.9 < \eta^{\mu} < 1.3$ and $p^{\mu}_t > 2.0\,\mathrm{GeV}$ or $-1.6 < \eta^{\mu} < -0.9$ and $p^{\mu} > 2.0\,\mathrm{GeV}$

The main differences to the extended analysis are the requirement of one jet in the Breit frame and the restriction to muons in the barrel and rear detector with a higher p^{μ}_t threshold in the barrel.

8.3 Signal determination

The determination of the beauty fraction is performed by a fit of the p^{rel}_t distributions of beauty and the sum of charm and light flavor MC to the data, according to Equation 5.22 after all selection cuts (see Sec. 7) applied. For the extended analysis the p^{rel}_t distribution of the different MC samples normalized to data luminosity is shown in Figure 8.1 (left). The fit to the data distribution results in a scaling factor for the beauty MC of 2.36 ± 0.23 and a beauty fraction of $23.2 \pm 2.3\%$ (Fig. 8.1 right). The number of beauty events obtained in the extended analysis is 1100. This underestimation of beauty production by a factor of ~ 2 by this kind of MC generators (LO matrix elements with DGLAP parton showers) was expected from results of other analyses (e.g. [Gut05]). The background MC is scaled by a factor of 1.06 to describe the data. This means, that the absolute normalization of the charm and light flavor contribution in data is nearly described by the MC without scaling.
For the restricted sample, a selection defined in Section 7.8 is used. The p^{rel}_t fit applied to the restricted sample (see Fig. 8.2) results in a slightly higher beauty fraction of $24.3 \pm 3.1\%$ but a significantly lower absolute number of beauty events of 580. The scaling factor of the beauty MC of 2.23 ± 0.28 is compatible with the scale for the extended analysis within errors.

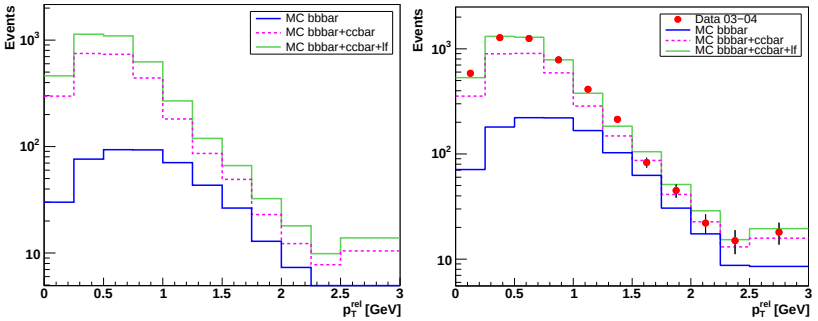

Figure 8.1: p^{rel}_t distribution of the luminosity weighted MC sample (left) and after the fit to the data points (right).

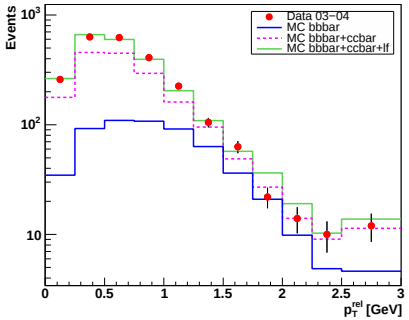

Figure 8.2: p^{rel}_t distribution for the restricted analysis after the fit to the data points.

8.4 Cross section in the restricted analysis

The cross section in the restricted signal region on the 03/04 data sample of $39.7\,\mathrm{pb}^{-1}$ luminosity is determined to be

$$\sigma^{b\bar{b}}(ep \to e\, b\bar{b}\, X \to e\, jet\, \mu\, X') = 39.2 \pm 5.1(\mathrm{stat.})^{+1.8}_{-5.4}(\mathrm{syst.})\,\mathrm{pb}. \quad (8.6)$$

Compared to the published cross section for a data sample of $72\,\mathrm{pb}^{-1}$ (99/00 data) [Che04b] of

$$\sigma^{b\bar{b}} = 40.9 \pm 5.7(\mathrm{stat.})^{+6.0}_{-4.4}(\mathrm{syst.})\,\mathrm{pb} \quad (8.7)$$

and the NLO QCD prediction with hadronization corrections of

$$20.6^{+3.1}_{-2.2}\,\mathrm{pb} \quad (8.8)$$

the new results agree very well. Due to the higher acceptance of the new muon selection, the statistical error of the new analysis is smaller, even though the luminosity is 1.8 times lower. The given systematic error is obtained by the procedure described in Section 8.9. The MC predicted cross section is $17.5 \pm 0.1(\text{stat.})\,\text{pb}$ and the scaling factor therefore set to 2.23.

8.5 Differential cross section in the restricted analysis

To derive differential cross sections for p_t^μ, the beauty contribution has to be determined for every p_t^μ bin using the p_t^{rel} method. In the histograms of differential cross sections the MC is scaled by a scaling factor (2.23) extracted from the p_t^{rel} fit for the total data sample. This is not necessarily the same as the normalization of the differential cross sections. For a comparison with the previous analysis, the same bins are chosen with an additional bin at low p_t^μ. Thus, the measurements are directly comparable and the region with a high difference between data and NLO (and MC) is supplemented with a new data point. The purity and acceptance for this selection are shown in Figure 8.3. For barrel muons, a cut of $p_t^\mu > 2\,\text{GeV}$ is applied, thus the lowest p_t^μ bin is populated only with muons from the rear region where no transverse momentum cut is applied but a momentum cut $p^\mu > 2\,\text{GeV}$.

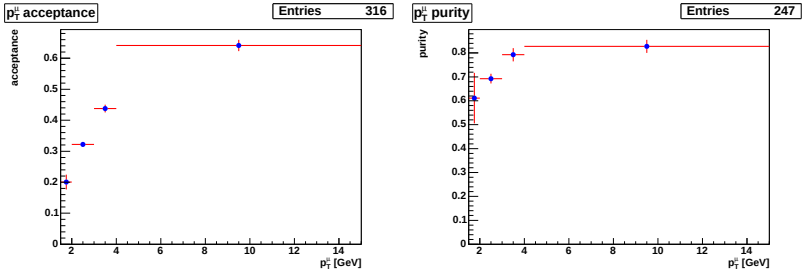

Figure 8.3: Acceptance (left) and purity (right) of the differential muon p_t cross section measurement in the restricted analysis.

In order to reduce the statistical error and extend the phase space also for the lowest p_t^μ bin to the barrel region, the barrel muon p_t cut is lowered to $p_t^\mu > 1.5\,\text{GeV}$. This analysis is called *modified restricted analysis*. The resulting purity and acceptance are shown in Figure 8.4. With the same acceptance for a larger phase space in the lowest bin, the number of events is 8 times larger in the modified restricted analysis.

The differential cross sections of this modified analysis still allow a direct comparison with the previous analysis in all bins of $p_t^\mu > 2\,\text{GeV}$. A direct comparison

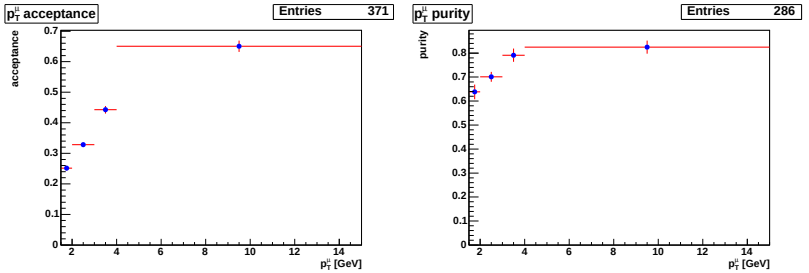

Figure 8.4: Acceptance (left) and purity (right) of the differential muon p_t cross section measurement with a p_t cut lowered to $p_t^\mu > 1.5\,\text{GeV}$ in the modified restricted analysis.

with the data of the previous analysis and its NLO QCD prediction from HVQDIS is shown in Figure 8.5. For $p_t^\mu > 3\,\text{GeV}$, the new measurement is in agreement with the NLO prediction. For lower transverse momenta ($2\,\text{GeV} < p_t^\mu < 3\,\text{GeV}$), the difference between data and NLO QCD is smaller than in the previous measurement ($\sigma^{b\bar{b}}_{data03/04} = 19.1 \pm 3.5(\text{stat.})^{+3.0}_{-3.2}(\text{syst.})\,\text{pb}$, $\sigma^{b\bar{b}}_{data99/00} = 30.5 \pm 7.6(\text{stat.})^{+6.3}_{-4.2}(\text{syst.})\,\text{pb}$, $\sigma^{b\bar{b}}_{NLO(HVQDIS)} = 7.8$ to $11.0\,\text{pb}$). The LO matrix element plus parton shower MC (RAPGAP) describes the shape of the data distribution within errors, even for the lowest p_t^μ bins.

Due to the improved muon detection efficiency, the statistical errors of the new measurement in the $p_t^\mu < 3\,\text{GeV}$ region are smaller than in the previous analysis, even for the lower luminosity of the new data sample. In the higher p_t^μ region, the efficiency was high already in the 99/00 analysis and the statistical error of the 03/04 analysis is larger. Furthermore, the small number of events (in particular for $3\,\text{GeV} < p_t^\mu < 4\,\text{GeV}$) results in a large error of the p_t^{rel} fit.

In the cross section measurement with the extended analysis, the number of events is larger and the uncertainties are smaller.

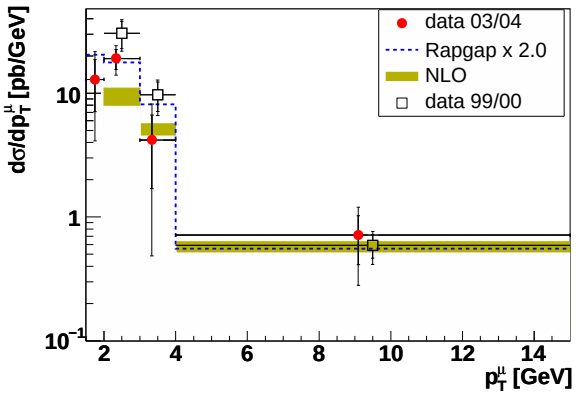

Figure 8.5: Differential cross section in p_t^μ for the measurement in the restricted analysis. The new measurement using the 03/04 data is shown as red dots. The error bars on the data points correspond to the statistical uncertainty (inner error bars) and to the statistical and systematic uncertainties added in quadrature (outer error bars). The scaled RAPGAP MC is shown as a blue, dotted line. Furthermore results of the previous analysis of 99/00 data are shown as open squares. The yellow band correspond to NLO QCD calculations with hadronization corrections.

8.6 Cross section in the extended analysis

Having shown the compatibility of the restricted analysis with the previous analysis, the measurement of cross sections in the extended analysis is presented in the following. The visible cross section in the kinematic region defined by the cuts in Sec. 8.2, is determined to be

$$\sigma^{b\bar{b}}(ep \to e\, b\bar{b}\, X \to e\, jet\, \mu\, X') = 57.9 \pm 5.8(\text{stat.})^{+3.5}_{-8.1}(\text{syst.})\,\text{pb}. \qquad (8.9)$$

The higher cross section compared to the restricted analysis is mainly due to the lower p_t^μ cut of 1.5 GeV, the wider pseudo-rapidity region $\eta^\mu > -1.6$ and the different jet selection. The higher Q^2 cut ($Q^2 > 4\,\text{GeV}$ in the new analysis) reduces the cross section of the extended analysis by about 8%. The NLO QCD calculations for the extended analysis are not yet available , thus the measurements are compared to the scaled LO matrix element plus parton showering MC (RAPGAP). The cross section predicted by the MC is $25.2 \pm 0.2(\text{stat.})\,\text{pb}$ and the scaling factor is obtained to be 2.36. As soon as the NLO QCD calculations are available, they will be included in the comparison.

8.7 Differential cross section in the extended analysis

Differential cross sections are measured in the following variables: virtuality Q^2, p_t and η of the muon, p_t and η of the jet. The procedure is described for the measurement of $d\sigma/dQ^2$. For the other differential cross section measurements the same procedure is applied accordingly.

8.7.1 $d\sigma/dQ^2$

The p_t^{rel} distributions for the determination of the beauty fraction for each bin in Q^2 are shown in Figure 8.6

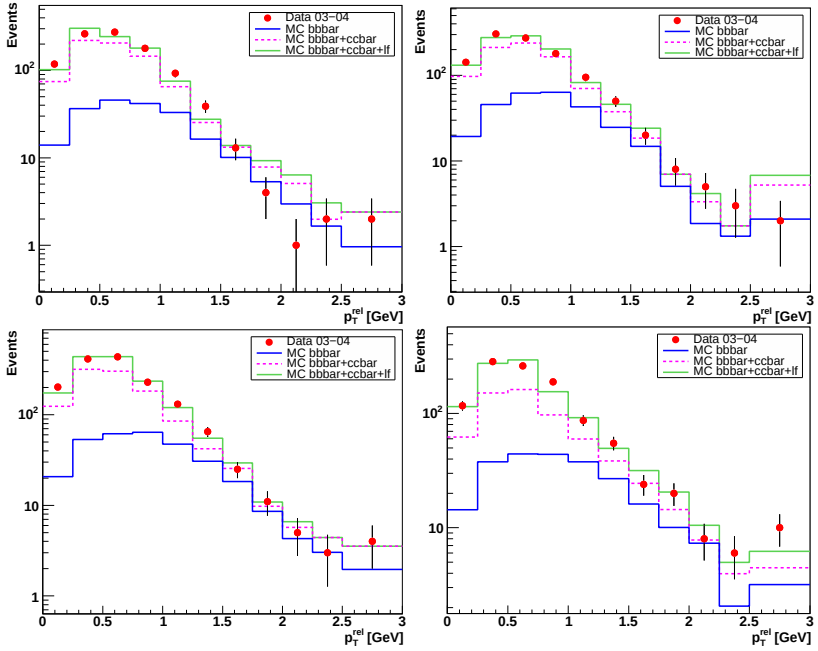

Figure 8.6: p_t^{rel} distributions for the four Q^2 regions used to determine the beauty fraction: $4\,\text{GeV}^2 < Q^2 < 10\,\text{GeV}^2$(upper left), $10\,\text{GeV}^2 < Q^2 < 25\,\text{GeV}^2$(upper right), $25\,\text{GeV}^2 < Q^2 < 100\,\text{GeV}^2$(lower left) and $100\,\text{GeV}^2 < Q^2 < 1000\,\text{GeV}^2$(lower right)

The corresponding acceptance and purity are shown in Figure 8.7. The measurement

of differential cross sections $d\sigma/dQ^2$ and the MC predictions (scaled up by a factor of 2.36) are shown in Figure 8.8. The MC reproduces the shape of the data very well.

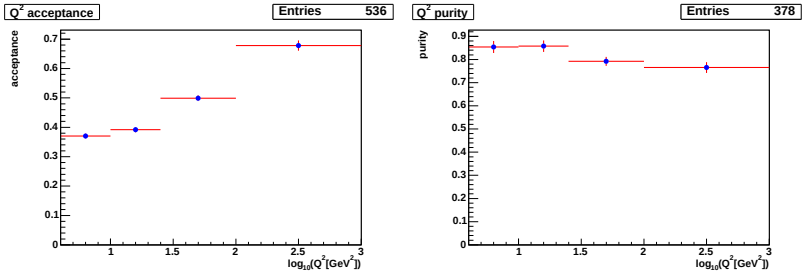

Figure 8.7: Acceptance (left) and purity (right) of the differential cross section in Q^2. Only statistical errors are shown.

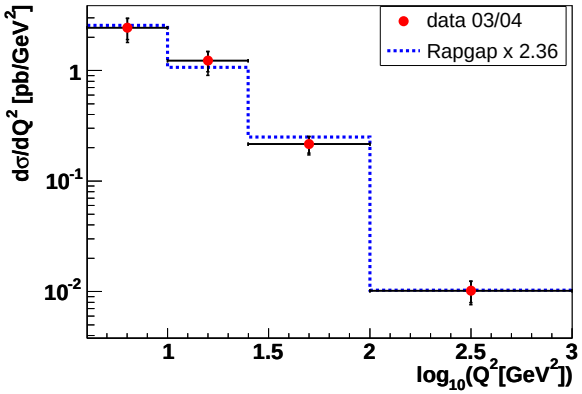

Figure 8.8: Differential cross section $d\sigma/dQ^2$. The measurement is shown as red dots. The error bars on the data points correspond to the statistical uncertainty (inner error bars) and to the statistical and systematic uncertainties added in quadrature (outer error bars). The RAPGAP MC (blue, dotted line) is scaled by a factor of 2.36 determined by the global p_t^{rel} fit.

8.7.2 $d\sigma/dp_t^\mu$ and $d\sigma/dp_\eta^\mu$

The differential cross section as a function of muon transverse momentum $d\sigma/dp_t^\mu$ is shown in Figure 8.9. The MC describes the shape of the data within statistical errors.

No difference between data and MC for low p_t^μ, as measured in the previous analysis, is found. The uncertainties are smaller than in the restricted analysis.

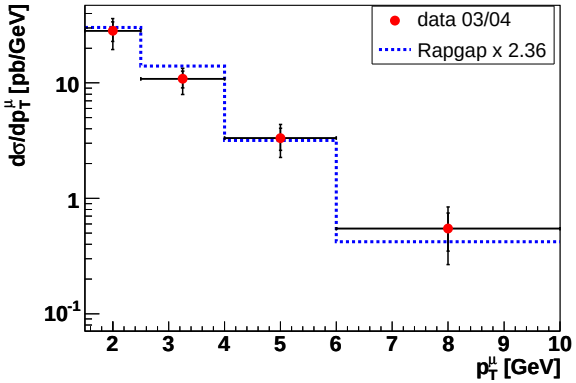

Figure 8.9: Differential cross section $d\sigma/dp_t^\mu$. The data (red dots) are compared to scaled RAPGAP MC (dotted line). Details are as described in the caption to Fig. 8.8.

In Figure 8.10, the differential cross sections for muon pseudo-rapidity $d\sigma/d\eta^\mu$ is shown. In general, the data and MC agree in shape. The observation of the previous analysis, that the prediction (NLO QCD and RAPGAP MC) is below the data for high η^μ is not found in the extended phase space of this analysis.

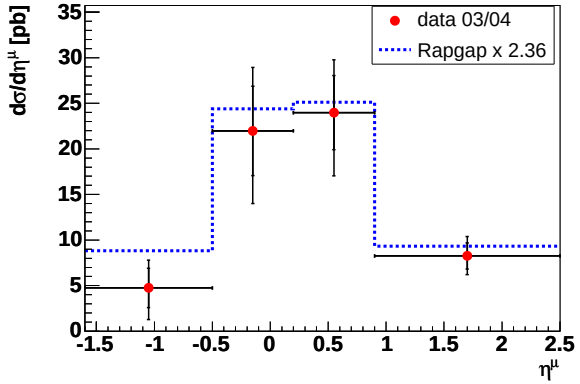

Figure 8.10: Differential cross section $d\sigma/d\eta^\mu$ of data and scaled RAPGAP MC. Details are as described in the caption to Fig. 8.8.

8.7.3 $d\sigma/dp_t^{jet}$ and $d\sigma/dp_\eta^{jet}$

Figure 8.11 shows the differential cross section as a function of p_t^{jet} of the jet associated to the muon. The shape of the data is reproduced by the MC. The measurement of $d\sigma/d\eta^{jet}$, shown in Figure 8.12, agrees with the scaled MC prediction.

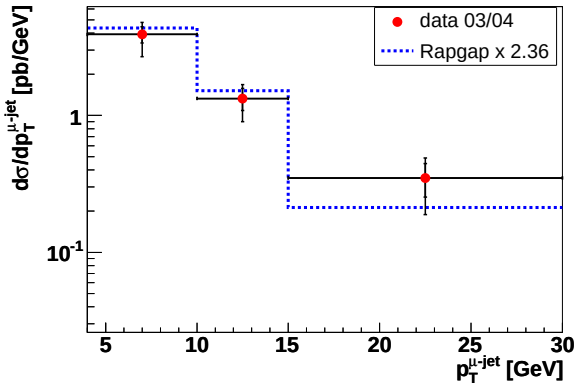

Figure 8.11: Differential cross section $d\sigma/dp_t^{jet}$ of data and scaled RAPGAP MC. Details are as described in the caption to Fig. 8.8.

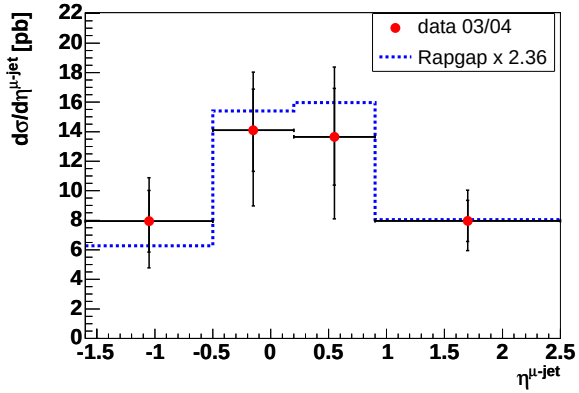

Figure 8.12: Differential cross section $d\sigma/d\eta^{jet}$ of data and scaled RAPGAP MC. Details are as described in the caption to Fig. 8.8.

8.8 Double differential cross section

In order to extract the beauty contribution to the proton structure function $F_2^{b\bar{b}}$, double differential cross section are needed. The measurement of $d^2\sigma/dQ^2dx$ is related to $F_2(x,Q^2)$ via Equation 2.12. As quoted in [Akt05b], the structure function $F_2^{b\bar{b}}$ can be derived from the reduced cross section:

$$\tilde{\sigma}^{b\bar{b}} = F_2^{b\bar{b}} - \frac{y^2}{1+(1-y)^2} F_L^{b\bar{b}} \tag{8.10}$$

where the contribution of the longitudinal structure function $F_L^{b\bar{b}}$ to the reduced cross section is estimated by NLO QCD calculations. The reduced cross section $\tilde{\sigma}^{b\bar{b}}$ is defined as

$$\tilde{\sigma}^{b\bar{b}}(x,Q^2) = \frac{d^2\sigma^{b\bar{b}}}{dxdQ^2} \frac{xQ^4}{2\pi\alpha^2(1+(1-y)^2)}, \tag{8.11}$$

The double differential cross sections are measured in bins of Q^2x. In order to convert these bin averages into measurements at given Q^2x points, the values of Q^2, x and y for each bin have to be determined. In [Akt05b] this determination is performed using NLO QCD expectation for $\tilde{\sigma}^{b\bar{b}}$. The measured double differential cross sections are shown in Figure 8.13 as well as in Table 8.1. The MC describes the shape of the data distributions well within the uncertainties.

The next step would be to perform the NLO QCD calculations to extract the reduced cross sections and to derive $F_2^{b\bar{b}}$. The good description of the data by the MC, that is found in this measurement, is a necessary condition for a reliable extrapolation to $F_2^{b\bar{b}}$. A very preliminary estimation of the error of this measurement leads to errors competitive to the errors given in [Akt05b] (see Fig 3.9) for a larger data sample of 57.4 pb^{-1}.

Q^2 range [GeV^2]	$\log_{10} x$ range	$\frac{d^2\sigma}{dQ^2dx}$ [pb/ GeV^2]	Δ_σ^{stat}
$[4, 25]$	$[-4.5, -3.6]$	0.284	0.122
$[4, 25]$	$[-3.6, -3.0]$	1.53	0.29
$[25, 100]$	$[-3.6, -3.0]$	0.103	0.034
$[25, 100]$	$[-3.0, -2.5]$	0.313	0.057
$[100, 3162]$	$[-2.0, -2.5]$	0.00149	0.00055
$[100, 3162]$	$[-2.5, -2.0]$	0.00356	0.00084
$[100, 3162]$	$[-2.0, -1.0]$	0.00113	0.00036

Table 8.1: Double differential cross sections.

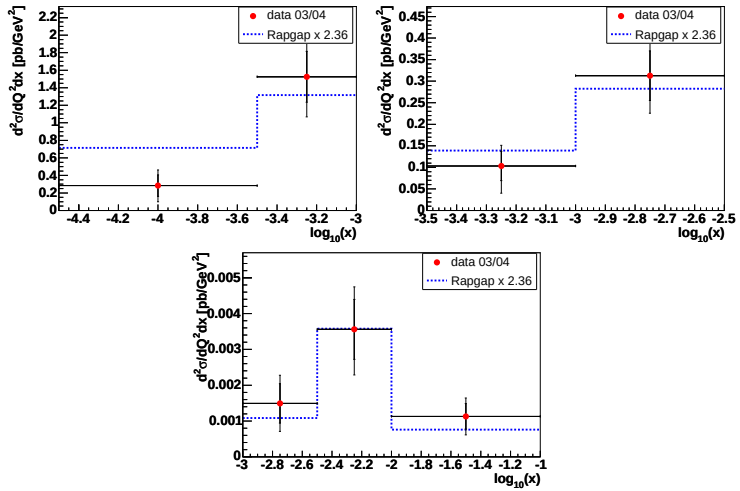

Figure 8.13: Double differential cross section $d^2\sigma/dQ^2dx$ for $4\,\mathrm{GeV}^2 < Q^2 < 25\,\mathrm{GeV}^2$ (upper left), $25\,\mathrm{GeV}^2 < Q^2 < 100\,\mathrm{GeV}^2$ (upper right) and $100\,\mathrm{GeV}^2 < Q^2 < 3162\,\mathrm{GeV}^2$ (lower plot). The data are compared to scaled RAPGAP MC. Details are as described in the caption to Fig. 8.8.

8.9 Systematic errors

The systematic errors of the cross section measurement are determined by changing the selection cuts or the analysis procedure and repeating the extraction of the cross sections. The uncertainties of the visible cross section are shown in Table 8.2. For the differential distributions the systematic uncertainties are calculated for each bin and are included in the figures (as the quadratic sum of statistical and systematic error). The following systematic studies were performed:

Light flavor background: The uncertainties of the background description is estimated by changing the ratio of charm to light flavor MC events. The light flavor fraction of the background is scaled by 1.5 and by 0.5. This leads to cross section differences of -3.9% and $+2.3\%$, respectively.

BREMAT efficiency correction: The difference between data and MC in the muon finder distribution (see Fig. B.1) is minimal if the BREMAT efficiency correction is reduced by 18%. Also the distribution of p_t^μ is better described applying this reduction (see Fig. B.2). The resulting decrease of the cross section after this modification of -11.5% is expected to cover the systematic uncertainty of the BREMAT efficiency correction.

The increase of the correction factors increases also the differences between data and MC in the muon finder distribution. Thus only the reduction is treated as a systematic uncertainty.

MUBAC efficiency correction: The systematic error of the MUBAC efficiency correction is determined by varying the ratio of muons corrected by the tight and loose configuration. Either all muons fulfilling the tight and loose cuts are corrected using the tight and loose configuration, or all muons are corrected using the loose configuration. The difference in the cross section is -0.7%.

Energy scale uncertainty: The energy of the jets in MC relative to data is scaled by $\pm 3\%$. The changes of the cross section are $+3.8\%$ and -5.6% respectively.

These uncertainties are added in quadrature separately for the positive and negative variations to derive the total systematic error. The uncertainty of the luminosity measurement is 4.2% [Sto05] for the data period used. The luminosity error affects the overall normalization and is a correlated error in each data bin. This uncertainty is added in quadrature to the total visible cross section but is not shown in the differential cross section distributions. A difference in the p_t^{rel} distribution of the light flavor MC and the data is measured for the PYTHIA MC, e.g. in [Gut05]. In [Che04b], RAPGAP is used as MC generator and the uncertainty due to the imperfect p_t^{rel} description is within the error of the muon efficiency correction. For the HERA II data and MC used in this analysis no such study has been performed yet. As the error is expected to be small, it is not included in the systematic study yet but will be included when the MC and data samples are available.

Quantity	Variation	Δ_σ
Light flavor background	1.5*lf MC	-3.9%
	0.5*lf MC	$+2.3\%$
BREMAT eff variation	BREMAT eff -18%	-11.5%
muon eff variation MUBAC	use loose and tight	-0.7%
Energy scale uncertainty	E_t^{jet} $+3\%$	$+3.8\%$
	E_t^{jet} -3%	-5.6%
Luminosity measurement		$\pm 4.2\%$
Total systematic error		$+6.1\%$
		-14.0%

Table 8.2: Systematic errors.

Chapter 9

Outlook

While LO matrix element plus parton shower MC is able to describe the shape of differential cross section measurements, NLO QCD calculations are expected to predict the absolute values. To perform these calculations has the first priority.

The potential of the ZEUS detector at HERA II is not fully exploited yet. The measurement of the impact parameter (see Sec. 5.13) is possible using the MVD. It provides an independent method for the determination of the beauty (or charm) content. A combined fit of the p_t^{rel} distribution and the impact parameter distribution would increase the precision of the beauty measurement. The distribution of the impact parameter for events selected in the extended analysis is shown in Figure 9.1. The left figure

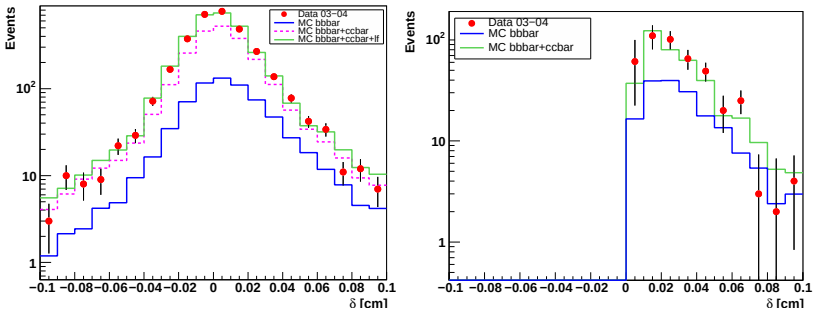

Figure 9.1: Impact parameter distribution for the selected event sample (left). Impact parameter distribution after subtraction of the mirrored negative part of the distribution.

shows the data and the MC distributions. The right figure shows the positive part of the impact parameter distribution with the mirrored negative distribution subtracted. The symmetric light flavor background cancels and the different shape of the beauty and charm distributions can be used to perform a fit to the data. As the MC, scaled with the scaling factors from the p_t^{rel} fit, shows very good agreement with the data, an

additional impact parameter fit is expected to improve the error of the beauty cross section measurement without changing the central value significantly. The simulated impact parameter distribution shown here is smeared according to studies performed in [Zeu05]. The smearing is not optimized for this analysis but the data are described very well.

The next step planned is to include the newest 2005 data into the analysis. This will enhance the luminosity by a factor of > 3 and allows the combination of the p_t^{rel} and the impact parameter method for the whole data sample.

The HERA I data are also available, providing a luminosity ~ 4 times higher than used in this analysis. On HERA I data the analysis is restricted to the p_t^{rel} method due to the absence of the MVD.

The measurement of the beauty contribution to the structure function $F_2^{b\bar{b}}(Q^2, x)$ requires the determination of Q^2, x and y for each bin of $d^2\sigma^{b\bar{b}}/dQ^2dx$. It is expected, that this information can be provided soon. The uncertainty of the double differential cross sections measured in this analysis allows to estimate, that the uncertainty of the $F_2^{b\bar{b}}$ measurement resulting from the cross sections in this thesis is competitive to the uncertainties in the previous H1 measurement [Akt05b].

Chapter 10

Conclusions

In this thesis measurements of beauty quark production in the process:
$ep \to e\ b\bar{b}\ X \to e\ jet\ \mu\ X'$ in deep inelastic scattering at ZEUS have been presented. Total visible and differential cross sections of this process were measured. Furthermore double differential cross sections, a necessary step towards a measurement of the beauty contribution to the proton structure function $F_2^{b\bar{b}}$, were measured. This analysis used a data sample of $\mathcal{L} = 39\,\mathrm{pb}^{-1}$ collected in the years 2003 and 2004 after the upgrade of HERA.

Events were selected that contain a scattered electron, a jet and a muon inside the jet. To reach a high efficiency the redundancy of different muon detectors was exploited. This method allows the selection of muons covering a large pseudo-rapidity range with a low transverse momentum threshold.

The fraction of events from beauty quark production was extracted on a statistical basis using the transverse momentum of the muon relative to the associated jet. A beauty fraction of 23.2 % has been achieved, equivalent to 1100 events containing beauty quarks. The total visible cross section was measured to be:

$$\sigma^{b\bar{b}}(ep \to e\ b\bar{b}\ X \to e\ jet\ \mu\ X') = 57.9 \pm 5.8(\mathrm{stat.})^{+3.5}_{-8.1}(\mathrm{syst.})\,\mathrm{pb} \qquad (10.1)$$

in the kinematic region defined by: $Q^2 > 4\,\mathrm{GeV}^2$, $y > 0.05$ and $y < 0.7$,
one jet originating from a beauty quark with: $E^{jet}_{t,lab} > 5\,\mathrm{GeV}$ and $-2 < \eta^{jet} < 2.5$
and a muon originating from a beauty quark decay (direct or indirect) included in this jet with: $p_t^\mu > 1.5\,\mathrm{GeV}$ and $\eta^\mu > -1.6$ (for details see Sec. 8.2).
This cross section is a factor of 2.36 higher than predicted by MC using LO matrix elements with DGLAP parton showers. This underestimation of beauty production is typical for this kind of MC generators and was seen also in other analyses [Gut05]. Differential cross sections in p_t^μ and η^μ, in p_t^{jet} and η^{jet} and in Q^2 were measured. In all distribution the data are described by the scaled MC prediction within errors. Double differential cross sections $d^2\sigma/dQ^2dx$ were measured. The good description of the data by the MC, that is found in this measurement, is a necessary condition for a reliable extrapolation to $F_2^{b\bar{b}}$.

The previous analysis of 1999 and 2000 data [Che04b], performed in a restricted phase space compared to the new analysis, saw the data above the prediction in some regions (at low values of p_t^μ and Q^2 and high values of η^μ). The data in these regions are well described by the MC in the extended phase space of the analysis described in this thesis. This result indicates the validity of QCD predictions for this phase space.

In order to compare results of this analysis directly with the previous measurement, the same kinematic region was chosen. The total cross section measurements of both analyses are in good agreement. Also the differential cross section measurement $d\sigma/dp_t^\mu$ is in agreement with the previous measurement within statistical and systematic errors. It is in better agreement with the NLO QCD predictions in the region of low p_t^μ, where the most significant discrepancy in the previous analysis was seen.

Perturbative QCD, in the approach of LO matrix elements with DGLAP PS, provides an excellent description of the shape of all data distributions shown. In general, QCD predictions agree well with the data in beauty quark production.

The improved vertex resolution for the new data allows a second, independent determination of the beauty quark fraction, the impact parameter method. The first distributions of the impact parameter in data are well described by the MC promising a reduction of the uncertainty of the beauty quark cross section measurement and a more precise determination of $F_2^{b\bar{b}}$.

Appendix A

Muon efficiency correction

The application of the muon efficiency correction factors (see Fig. A.2, A.3 and A.4) is done by weights of the muons. The weights depend on p_t^μ and η^μ and the combination of muon finders detecting this muon. The muon efficiencies are calculated according to Tab. A.1.

Muon detected by	weight
BREMAT AND MUBAC	$w = \frac{\epsilon^{data}_{BREMAT}}{\epsilon^{MC}_{BREMAT}} \cdot \frac{\epsilon^{data}_{MUBAC}}{\epsilon^{MC}_{MUBAC}}$
BREMAT AND NOT MUBAC	$w = \frac{\epsilon^{data}_{BREMAT}}{\epsilon^{MC}_{BREMAT}} \cdot \frac{1-\epsilon^{data}_{MUBAC}}{1-\epsilon^{MC}_{MUBAC}}$
NOT BREMAT AND MUBAC	$w = \frac{1-\epsilon^{data}_{BREMAT}}{1-\epsilon^{MC}_{BREMAT}} \cdot \frac{\epsilon^{data}_{MUBAC}}{\epsilon^{MC}_{MUBAC}}$
MPMATCH AND MUBAC	$w = \frac{\epsilon^{data}_{MPMATCH}}{\epsilon^{MC}_{MPMATCH}} \cdot \frac{\epsilon^{data}_{MUBAC}}{\epsilon^{MC}_{MUBAC}}$
MPMATCH AND NOT MUBAC	$w = \frac{\epsilon^{data}_{MPMATCH}}{\epsilon^{MC}_{MPMATCH}} \cdot \frac{1-\epsilon^{data}_{MUBAC}}{1-\epsilon^{MC}_{MUBAC}}$
NOT MPMATCH AND MUBAC	$w = \frac{1-\epsilon^{data}_{MPMATCH}}{1-\epsilon^{MC}_{MPMATCH}} \cdot \frac{\epsilon^{data}_{MUBAC}}{\epsilon^{MC}_{MUBAC}}$

Table A.1: Efficiency correction weights

A special case is the BRMUON correction, because a so called *dead LST* correction has been applied to the MC at ORANGE level. This correction is meant to apply the inefficiency of BRMUON in data to the trigger simulation in MC. It seems, that this procedure over-corrects the efficiency and the result is, that the efficiency in MC is lower than in data in some p_t^μ-η^μ bins.

The muons used in the DIS analysis are shown in the p_t-η plane are shown in Figure A.5. Taking the distribution of muons into account, the range of correction factors

applied for MUBAC goes from 0.4 to 1.0, for BREMAT between 0.5 and about 2.0 and for MPMATCH in the range of 0.7 to 1.5.

Figure A.6 shows the effect of the correction to the muon finder combinations.

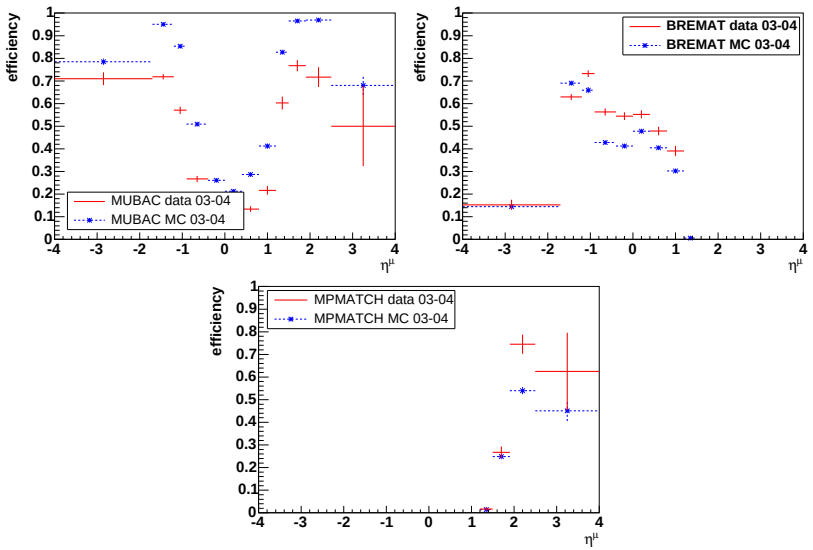

Figure A.1: Absolute efficiencies for MUBAC, BREMAT and MPMATCH for 1.5 GeV $< p_t^\mu <$ 1.75 GeV for the loose configuration. Efficiency of muons in data (solid red crosses) and MC (dashed blue crosses) with statistical errors are shown.

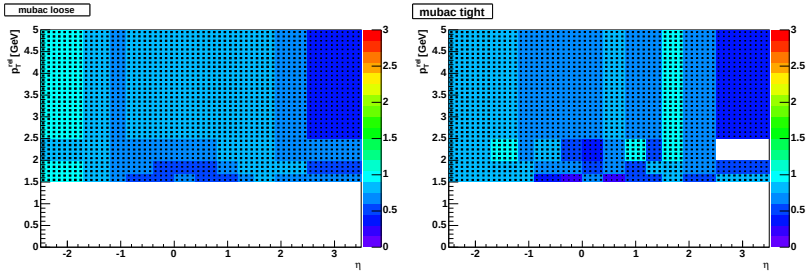

Figure A.2: Correction factors for the MUBAC finder in the η-p_t plane for loose and tight configuration.

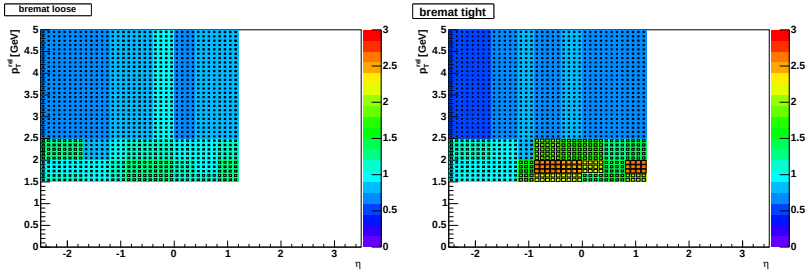

Figure A.3: Correction factors for the BREMAT finder in the η-p_t plane for loose and tight configuration.

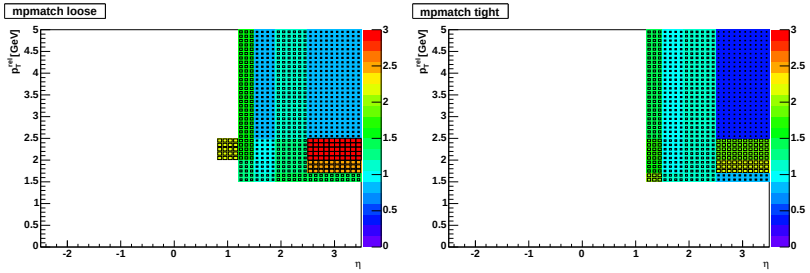

Figure A.4: Correction factors for the MPMATCH finder in the η-p_t plane for loose and tight configuration.

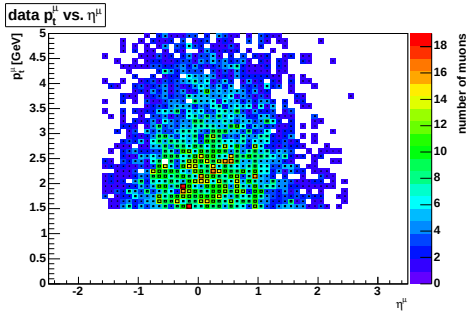

Figure A.5: Number of data muons in the η-p_t plane after all cuts

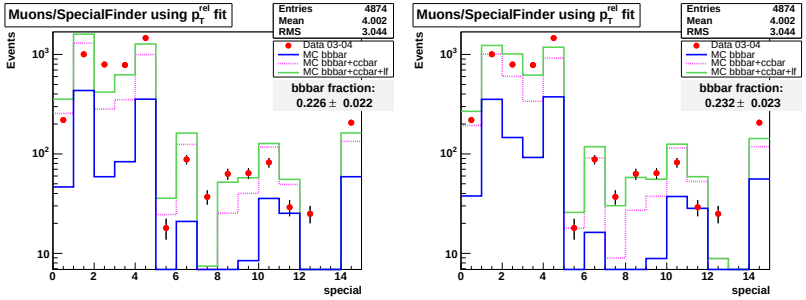

Figure A.6: Control plot for the different muon finder combinations (see Tab. A.2) before and after muon efficiency correction.

Number	Section	BREMAT	MUBAC	MPMATCH or MUFO	MV
0	barrel	yes	yes		no
1	barrel	yes	yes		yes
2	barrel	yes	no		
3	barrel	no	yes		no
4	barrel	no	yes		yes
5	rear	yes	yes		no
6	rear	yes	yes		yes
7	rear	yes	no		
8	rear	no	yes		no
9	rear	no	yes		yes
10	forward		yes	yes	no
11	forward		yes	yes	yes
12	forward		no	yes	
13	forward		yes	no	no
14	forward		yes	no	yes

Table A.2: Combinations of muon finders.

Appendix B

Systematic uncertainties of the muon correction

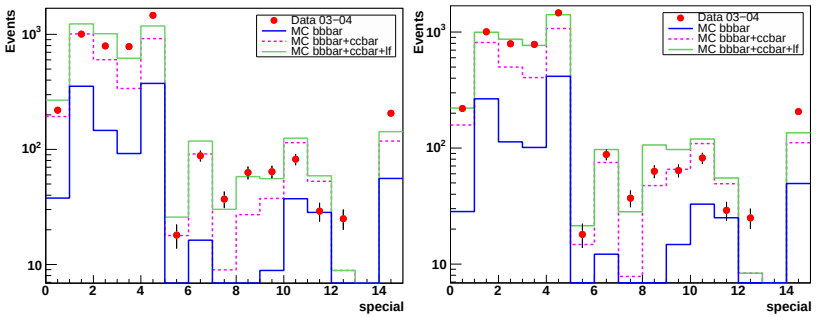

Figure B.1: Control plot for the different muon finder combinations (see Tab. A.2) using the BREMAT correction (left) and using a BREMAT correction scaled 18% down (right). The data in the barrel region (bins 0 to 4) are better described by the MC in the right histogram. This region dominates the total visible cross section measurement. In the rear region (bins 5 to 9) the description of the data becomes worse. This variation of the efficiency correction is used for the study of the systematic error.

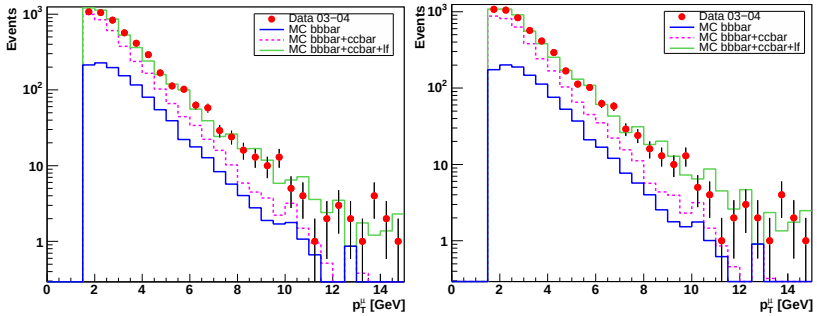

Figure B.2: Control plot for muon p_t using the BREMAT correction (left) and using a BREMAT correction scaled 18% down (right). The data distribution is well described by the MC applying the scaled corrections.

Appendix C

Jets in Orange

For this analysis, different jet types are reconstructed. In order to use one ntuples for different analysis, the jet clustering is performed in the laboratory frame and the Breit frame for DIS events. In addition, the jet algorithm is executed on all EFOs for PHP events. The list of EFOs used for the jet finding should stay the same for each jet algorithm. Therefore the EFO, corresponding to the DIS electron is not removed completely from the list of EFOs, but is flagged to ignore this EFO for DIS jets.

In Figure C.1 the η-distribution of jets in a b MC for the different jet finder configurations is shown.

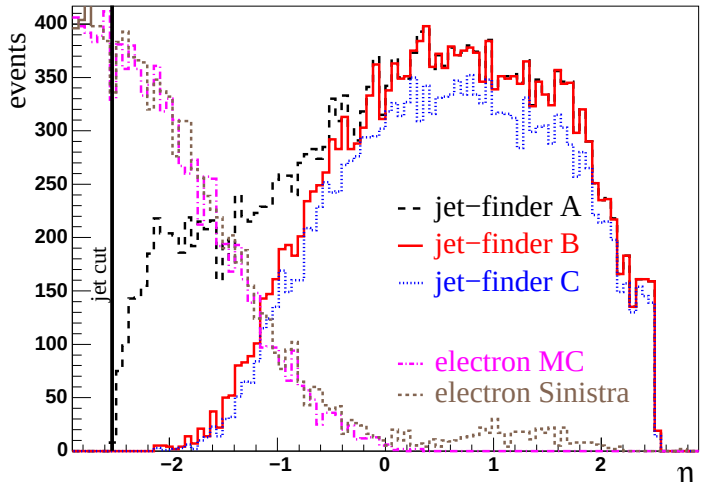

Figure C.1: Pseudo-rapidity distribution of jets. Jets are reconstructed including all EFOs (jet-finder A) or excluding a DIS electron in labframe (jet-finder B) and Breit frame (jet-finder C). In addition the distribution of the DIS electron is shown.

Technically, the identification of the EFO (or ZUFO) corresponding to the Sinistra electron is done by the tufo-id. A value of 3000 is added to the original tufo-id if the ZUFO matches the Sinistra electron, so the final tufo range is from 3001 to 3041.

The k_t-jet finder is called four times with different arguments. For the first finder, called KTJETSA, no electron removal is used and jets are reconstructed in the lab frame for PHP analysis(ORANGE flags ORANGE-EREJECTA 0; ORANGE-JETBSTA 0). KTJETSB uses the ZUFO electron removal for DIS jets in the lab frame (ORANGE-EREJECTB 3; ORANGE-JETBSTB 0). Jet finder C and D are called to reconstruct jets in the Breit frame, while for finder C, the variables are boosted back to the lab frame and finder D saves the Breit frame variable directly (ORANGE-EREJECTC 3; ORANGE-JETBSTC 1 and ORANGE-EREJECTD 3; ORANGE-JETBSTD 3)

List of Figures

List of Tables

Bibliography

[Aba95] S.Abachi *et al.*, *Inclusive mu and B quark production cross-sections in p anti-p collisions at S**(1/2) = 1.8-TeV*, Phys. Rev. Lett. **74**, 3548 (1995)

[Abb93] G.Abbiendi *et al.*, *The ZEUS barrel and rear muon detector*, Nucl. Instrum. Meth. A**333**, 342 (1993)

[Abb93] G.Abbiendi *et al.*, *Observation of $J/\Psi \to \mu^+\mu^-$ in the first 273 nb-1 of 1993 run*, ZEUS-Note, 93-120, (1993)

[Abb99] G.Abbiendi, *Global tracking of muons in the Barrel and Rear region*, ZEUS-Note, 99-063 (1999)

[Abb00] B.Abbott *et al.*, D0 Collab., *The b anti-b production cross section and angular correlations in p anti-p collisions at s**(1/2) = 1.8-TeV*, Phys. Lett. B**487**, 264 (2000)

[Abe96] F.Abe *et al.*, CDF Collab., *Measurement of correlated mu - anti-b jet cross-sections in p anti-p collisions at s**(1/2) = 1.8-TeV*, Phys. Rev. D**53**, 1051 (1996)

[Abe02] K.Abe *et al.*, Belle Collab., *Measurement of the inclusive semileptonic branching fraction of B mesons and |V(cb)|. ((B))*, Phys. Lett. B**547**, 181 (2002)

[Abr95] H.Abramowicz, A.Caldwell, R.Sinkus, *Neural network based electron identification in the ZEUS calorimeter*, Nucl. Instrum. Meth. A **365** 508 (1995); R.Sinkus, T.Voss, *Particle identification with neural networks using a rotational invariant moment representation*, Nucl. Instrum. Meth. A**391**, 360 (1997)

[Abt97] I.Abt *et al.*, H1 Collab., *The H1 detector at HERA*, Nucl. Inst. Meth. A**386**, 310 and 348 (1997)

[Abt03] I.Abt *et al.*, HERA-B Collab., *Measurement of the b anti-b production cross section in 920-GeV fixed-target proton nucleus collisions*, Eur. Phys. J. C**26**, 345 (2003)

[Ach05] P.Achard *et al.*, L3 Collab., *Measurement of the cross section for open-beauty production in photon photon collisions at LEP*, Phys. Lett. B **619** 71 (2005)

[Aco02] D.Acosta *et al.*, CDF Collab., *Measurement of the B+ total cross section and B+ differential cross section dsigma/dp(T) in p anti-p collisions at s**(1/2) = 1.8-TeV*, Phys. Rev. D**65**, 052005 (2002)

[Adl03] C.Adloff *et al.*, H1 Collab., *Measurement and QCD analysis of neutral and charged current cross sections at HERA*, Eur. Phys. J. C**30** 1 (2003)

[Akt05] A.Aktas *et al.*, H1 Collab.,*Measurement of beauty production at HERA using events with muons and jets*, Eur. Phys. J. C**41** 453-467 (2005)

[Akt05b] A.Aktas *et al.* H1 Collab., *Measurement of F2(c anti-c) and F2(b anti-b) at low Q**2 and x using the H1 vertex detector at HERA*, arXiv:hep-ex/0507081

[Alb91] C.Albajar, *et al.*, UA1 Collab., *Beauty Production At The Cern P Anti-P Collider*, Phys. Lett. B**256**, 121 (1991);
Erratum-ibid. B **262**, 497 (1991)

[Alb94] C.Albajar, *et al.*, UA1 Collab., *Measurement of b anti-b correlations at the CERN p anti-p collider*, Z. Phys. C**61**, 41 (1994)

[Ale99] T.Alexopoulos, *et al.*, E771 Collab., *A measurement of the b anti-b cross section in 800-GeV/c proton silicon interactions*, Phys. Rev. Lett. **82**, 41 (1999)

[Alt77] G.Altarelli, G.Parisi, *Asymptotic Freedom In Parton Language*, Nucl. Phys. B**126**, 298 (1977)

[And83] B.Andersson, G.Gustafson, B.Sonderberg, *A General Model For Jet Fragmentation*, Z. Phys. C**20**, 317 (1983)

[And01] J.Andruszkow *et al.*, ZEUS Luminosity Group, *Luminosity measurement in the ZEUS experiment*, Acta Phys. Polon. B**32**, 2025 (2001)

[Aub03] B.Aubert *et al.*, BABAR Collab., *Measurement of the branching fraction for inclusive semileptonic B meson decays*, Phys. Rev. D**67**, 031101 (2003)

[Bai02] D. Bailey *et al.* , *Study of beam-induced backgrounds in the ZEUS detector from 2002 HERA running*, (unpublished) (2002), ZEUS-Note 02-018;
Addendum 1 (unpublished), (2002), ZEUS-Note 02-020;
Addendum 2 (unpublished), (2003), ZEUS-Note 02-027, all available on `http://www-zeus.desy.de/~kuze/zeusbg/`

[Bam97] A.Bamberger *et al.*, ZEUS Collab., *The small angle rear tracking detector of ZEUS*, Nucl. Instr. Meth., A**401**, 63 (1997)

[Bas95] U.Bassler, G.Bernardi, *On the kinematic reconstruction of deep inelastic scattering at HERA: The Sigma method*, Nucl. Instrum. Meth. A **361**, 197 (1995)

[Bel96] L.Bellagamba, *MVMATCH: A package to match FMUON tracks with Central Detectors*, ZEUS-Note 96-051 (1996)

[Ben91] S.Bentvelsen, J.Engelen, P.Kooijman *Reconstruction of* (x, Q^2) *and extraction of structure functions at HERA*, PHYSICS AT HERA vol.1, W. Buchmüller and G. Ingelman (eds.), Hamburg (1991)

[Bjo69] J.D.Bjorke, *Asymptotic Sum Rules At Infinite Momentum*, Phys. Rev. **179**, 1547 (1969)

[Blo69] Bloom *et al.*, *High-Energy Inelastic E P Scattering At 6-Degrees And 10-Degrees*, Phys. Rev. Lett. **23**, 930 (1969)

[Blo79] F. Jacquet, A. Blondel. Proc. of the Study of an ep facility for Europe, ed. U.Amaldi, DESY 79/48, 391, (1979)

[Blo05] I.Bloch, *Studies of beauty at H1 and ZEUS*, arXiv:hep-ex/0506006.

[Blo05b] I.Bloch, *Measurement of beauty production from dimuon events at Hera/Zeus* PhD thesis

[Bob92] M.Bobrowski, *et al.*, *Proportional counters as monitoring detectors of BAC chambers at the ZEUS experiment*, Nucl. Instrum. Meth. A**323**, 309 (1992)

[Bre00] J. Breitweg *et al.*, ZEUS Collab., *Measurement of open beauty production in photoproduction at HERA*, Eur. Phys. J. C **18**, 625 (2001)

[Bru84] R.Brun, *et al.*, CERN-DD/EE/84-1 (1984)

[Bus95] D.Buskulic *et al.*, ALEPH Collab., *Measurement of the effective b quark fragmentation function at the Z resonance*, Phys. Lett. B**357**, 699 (1995)

[Bor33] M.Born, Optik, Springer, Berlin (1933)

[Aco05] D. Acosta *et al.*, CDF Collab.,*Measurement of the J/psi meson and b-hadron production cross sections in p anti-p collisions at s**(1/2) = 1960-GeV*, Phys. Rev. D **71**, 032001 (2005)

[Cal69] C.G.Callan, D.J.Gross, *High-Energy Electroproduction And The Constitution Of The Electric Current*, Phys. Rev. Lett. **22**, 156 (1969)

[Car03] T.Carli, V.Chiochia, K.Klimek, *Definition and calculation of bottom quark cross-sections in deep-inelastic scattering at HERA and determination of their uncertainties*, JHEP **0309** 070 (2003)

[Cat92] S.Catani, Dokshitzer, L.Yuri, B.R.Webber, *The K-perpendicular clustering algorithm for jets in deep inelastic scattering and hadron collisions*, Phys. Lett. B**285**, 291-299 (1992);
S.Catani, Dokshitzer, L.Yuri, B.R.Webber, *Longitudinally invariant K(t) clustering algorithms for hadron hadron collisions*, Nucl. Phys. B**406** 187-224 (1993)

[Che03] S.Chekanov *et al.*, ZEUS Collab., *Beauty photoproduction measured using decays into muons in dijet events in e p collisions at s**(1/2) = 318-GeV*, arXiv:hep-ex/0312057

[Che04] S.Chekanov *et al.*, ZEUS Collab., *Evidence for a narrow baryonic state decaying to K0(S) p and K0(S) anti-p in deep inelastic scattering at HERA.*, Phys. Lett. B**591**, 7-22 (2004)

[Che04a] S. Chekanov *et al.*, ZEUS Collab., *Bottom photoproduction measured using decays into muons in dijet events in ep collisions at s**(1/2) = 318-GeV*, Phys. Rev. D **70**, 012008 (2004).

[Che04b] S.Chekanov *et al.*, ZEUS Collab., *Measurement of beauty production in deep inelastic scattering at HERA*, Phys. Lett. B**599** 173 (2004)

[Chi03] V.Chiochia, *Measurement of beauty quark production in deep inelastic scattering at HERA*, DESY-THESIS-03-031 (2003)

[Cia88] M.Ciafaloni, *Coherence Effects In Initial Jets At Small Q**2 / S*, Nucl. Phys. B**296**, 49 (1988);
S.Catani, F.Fiorani, G.Marchesini, *CD Coherence In Initial State Radiation*, Phys. Lett. B**234**, 339 (1990) and Nucl. Phys. B**336**, 18 (1990)

[Cor04] M.Corradi, M.Turcato, *Beauty production in dijet events* (unpublished), ZEUS-Note 04-005, (2004)

[Dan04] *A radiation monitor for the ZEUS detector at HERA*, IEEE Transactions on Nuclear Science, **51**, 4, p.1606 - 1612, (2004)

[Der91] M.Derrick *et al.*, *esign and construction of the ZEUS barrel calorimeter*, Nucl. Instrum. Meth. A**309**, 77 (1991);
A.Andresen *et al.*, *Construction and beam test of the ZEUS forward and rear calorimeter*, Nucl. Instrum. Meth. A**309**, 101 (1991);
A.Caldwell *et al.*, *Design and implementation of a high precision readout system for the ZEUS calorimeter*, Nucl. Instrum. Meth. A**321**, 356 (1992);

A.Bernstein *et al.*, *Beam tests of the ZEUS barrel calorimeter*, Nucl. Instrum. Meth. A**336**, 23 (1993)

[Dha03] S.Dhawan, Proceedings of the Conference Real Time'03, Montreal (2003); M.Sutton, Proceedings of the Conference Real Time'03, Montreal (2003); C.Youngman, Proceedings of the Conference Real Time'03, Montreal (2003); A.Polini, ECONF C0303241, MOGT005 (2003).

[Doe94] T.Doeker, A.Frey, M.Nakao, *Electron Position Reconstruction - Update of the ELECPO routines*, ZEUS-Note 94-123 (1994)

[Dok77] Y.Dokshitser, *Calculation Of The Structure Functions For Deep Inelastic Scattering And E+ E- Annihilation By Perturbation Theory In Quantum Chromodynamics. (In Russian)*, Sov. Phys. JETP **46**, 641 (1977)

[Eid04] S.Eidelman *et al.*, Particle Data Group, *Review of particle physics*, Phys. Lett. B**592**, 1 (2004)

[Fey69] R.P.Feynman, *Very High-Energy Collisions Of Hadrons*, Phys. Rev. Lett. **23**, 1415 (1969)

[Fis93] S.M.Fisher, P.Palazzi, *ADAMO Reference Manual for Version 3.3.*, CERN ECP, available on `http://adamo.web.cern.ch/Adamo/refmanual/Document.html`

[Fru87] R.Fruhwirth, Nucl. Inst. Meth. A**262**, 444 (1987)

[Gab04] A.Gabareen Mokhtar, H1 Collab., *Recent electroweak measurements from the H1 and ZEUS experiments*, arXiv:hep-ex/0406036

[Gar99] A.Garfagnini, *The ZEUS microvertex detector*, Nucl. Instrum. Meth. A**435**, 34 (1999);
R.Klanner, Prepared for International Europhysics Conference on High- Energy Physics (EPSHEP 99), Tampere, Finland, 15-21 Jul 1999;
C.Coldewey, *The ZEUS microvertex detector*, Nucl. Instrum. Meth. A**447**, 44 (2000);
E.N.Koffeman, *A silicon micro vertex detector for the ZEUS experiment*, Nucl. Instrum. Meth. A**453**, 89 (2000);
C.Coldewey, *Test of silicon strip detectors for the ZEUS microvertex detector*, Nucl. Instrum. Meth. A**453**, 149 (2000);
E.N.Koffeman, *The construction of the ZEUS micro vertex detector*, Nucl. Instrum. Meth. A**473**, 26 (2001);
M.C.Petrucci, *The ZEUS microvertex detector*, Int. J. Mod. Phys. A **16S1C**, 1078 (2001);
U.Koetz, *Test of silicon strip detectors for the ZEUS microvertex detector*, Nucl. Instrum. Meth. A**461**, 210 (2001);

V.Chiochia, *The ZEUS micro vertex detector*, Nucl. Instrum. Meth. A**501**, 60 (2003);
D.Dannheim *et al.* , *Design and tests of the silicon sensors for the ZEUS micro vertex detector*, Nucl. Instrum. Meth. A**505**, 663 (2003)

[Gei05] A.Geiser, *GMUON - a general ZEUS muon finder*, in preparation (2005)

[Gel64] M.Gell.Mann, *A Schematic Model Of Baryons And Mesons*, Phys. Lett. **8**, 214 (1964); G.Zweig, CERN-8192/TH 401 (1964); G.Zweig, CERN-8419/TH 402 (1964)

[Gia99] V.Giannotti, University of Roma, thesis, unpublished (1999)

[Gla03] C.Glasman, *Jet production in deep inelastic e p scattering at HERA*, arXiv:hep-ex/0312011

[Gri72] V.Gribov, L.Lipatov, *Deep Inelastic E P Scattering In Perturbation Theory*, Sov. J. Nucl. Phys. **15**, 438 and 675 (1972)

[Gri87] D.J.Griffiths, *Introduction to elementary particles*, John Wiley & Sons, (1987)

[Gut05] O.Gutsche, *Measurement of beauty quark cross sections in photoproduction with the ZEUS experiment at the electron proton collider HERA*, DESY-THESIS-2005-010 (2005)

[Hal84] F.Halzen, A.D.Martin,*Quarks and Leptons: An Introduction Course in Modern Particle Physics*, John Wiley & Sons, (1984)

[Ham81] Hamburg Desy - DESY HERA 81-10 (81,REC.AUG.) 292p.

[Har89] N.Harnew *et al.*, *Vertex Triggering Using Time Difference Measurements In The Zeus Central Tracking Detector*, Nucl. Instrum. Meth. A**279**, 290 (1989);
B.Foster *et al.*, *The Performance of the Zeus central tracking detector z-by-timing electronics in a transputer based data acquisition system*, Nucl. Phys. Proc. Suppl. **32**, 181 (1993);
B.Foster *et al.*, *The Design and construction of the ZEUS central tracking detector*,Nucl. Instrum. Meth. A**338**, 254 (1994)

[Har96] B.W.Harris, *Electroproduction of Heavy Quarks at NLO*, Presented at 1996 Annual Divisional Meeting (DPF 96) of the Division of Particles and Fields of the American Physical Society, Minneapolis, MN, (1996)

[Har98] G.Hartner, ZEUS-Note 98-058 (1998)

[Hol93] U.Holm (ed.), ZEUS Collab., *The ZEUS Detector. Status Report*, (unpublished), DESY (1993), available on `http://www-zeus.desy.de/bluebook/bluebook.html`

[Isg89] N.Isgur, M.B.Wise, *Weak Decays Of Heavy Mesons In The Static Quark Approximation*, Phys. Lett. B **232** 113 (1989);
N.Isgur, M.B.Wise, *Weak Transition Form-Factors Between Heavy Mesons*, Phys. Lett. B **237** 527 (1990)

[Jan95] D.M.Jansen *et al.*, *Measurement of the bottom quark production cross-section in 800-GeV/c proton - gold collisions*, Phys. Rev. Lett. **74**, 3118 (1995)

[Jon78] L.M.Jones, H.W.Wyld, *A Measurement of Beauty Production in High-Energy Positron-Proton Scattering*, Phys. Rev. D**17**, 759 (1978)

[Jun95] H.Jung, Comp. Phys. Commun. **86** 147 (1995);
H. Jung, *The RAPGAP Monte Carlo for Deep Inelastic Scattering*, version 3.10, Lund University, (2005) `http://www.quark.lu.se/~hannes/rapgap/`

[Kal60] Kalman, Rudolph, Emil, Transactions of the ASME-Journal of Basic Engineering D**82**, 35 (1960)

[Kle91] M.Klein, in *Physics at HERA*, edited by W. Buchmüller and G. Ingelman Vol. 1, 71, Hamburg, (1991)

[Koh05] T.Kohno, International Workshop on Advanced Computing and Analysis Techniques in Physics Research (ACAT05), Zeuthen (2005)

[Kuh99] S.Kuhlmann, *CTEQ5 parton distributions and ongoing studies*, Nucl. Phys. Proc. Suppl. **79** 108 (1999)

[Kur76] E.A.Kuraev, L.N.Lipatov, V.S.Fadin, *Multi - Reggeon Processes In The Yang-Mills Theory*, Sov. Phys. JETP **44**, 443 (1976); E.A.Kuraev, L.N.Lipatov, V.S.Fadin, *The Pomeranchuk Singularity In Nonabelian Gauge Theories*, Sov. Phys. JETP **45**, 199 (1977); I.I.Balitzki, L.N.Lipatov, *The Pomeranchuk Singularity In Quantum Chromodynamics*, Sov. J. Nucl. Phys. **28**, 822 (1978)

[Kuz00] V.A.Kuzmin, *Identification of leptons by ZEUS calorimeter*, Nucl. Instrum. Meth. A**453**, 336 (2000)

[Kwi91] A.Kwiatkowski, H.Spiesberger, H.-J.Möhring,*HERACLES 4.1 - An event generator for ep interactions at HERA including radiative processes*, Proc. of the Workshop on Physics at HERA, Vol. 3, edited by W.Buchmüller, G.Ingelman (1991), p. 1294.

[Kwi96] A.Kwiatkowski, H.Spiesberger, H.-J.Möhring, *HERACLES - An event generator for ep interactions at HERA including radiative processes. version 4.6*, (1996), `http://www.desy.de/~hspiesb/heracles.html`

[Leo05] G.Leonid, private communication

[LEP01] LEP/SLD Electroweak Heavy Flavor Results Winter 2001 Conferences, `http://lepewwg.web.cern.ch/LEPEWWG/heavy/`

[Lip75] L.Lipatov, *The Parton Model And Perturbation Theory*, Sov. J. Nucl. Phys. **20**, 94 (1975)

[Lön92] L.Lönnblad, *ARIADNE version 4: A Program for simulation of QCD cascades implementing the color dipole model*, Comp. Phys. Commun. **71**, 15 (1992)

[Lon03] A.Longhin, *Measurement of beauty production at HERA with a D* + mu tag*, DESY-THESIS-2004-050 (2003)

[Lop99] A.Lopez-Duran Viani, S.Schlensted, *Electron finder efficiencies and impurities. a comparison between SINISTRA95, EM and EMNET*, ZEUS-Note 99-077 (1999)

[Mad04] E.Maddox, (unpublished), PhD thesis, (2004)

[Mar04] A.D.Martin, R.G.Roberts, W.J.Stirling, R.S.Thorne, *Uncertainties of predictions from parton distributions. II: Theoretical errors*, Eur. Phys. J. C**35** 325 (2004)

[Nas88] P.Nason, S.Dawson, R.K.Ellis, *The Total Cross-Section For The Production Of Heavy Quarks In Hadronic Collisions*, Nucl. Phys. B**303**, 607 (1988);
P.Nason, S.Dawson, R.K.Ellis, *The One Particle Inclusive Differential Cross-Section For Heavy Quark Production In Hadronic Collisions*, Nucl. Phys. B**327**, 49 (1989)

[Ng95] J.Ng., W.Verkerke, *An Overview of SRTD Analysis*, ZEUS-Note 95-037 (1995)

[Oku77] S.Okubo, *Phi Meson And Unitary Symmetry Model*, Phys. Lett. **5**, 165 (1963);
S.Okubo, *Consequences Of Quark Line (Okubo-Zweig-Iizuka) Rule*, Phys. Rev. D **16**, 2336 (1977);
J.Iizuka, K.Okada, O.Shito, *Systematics And Phenomenology Of Boson Mass Levels. 3*, Prog. Th. Phys. **35**, 1061 (1966);
J.Iizuka, *Systematics And Phenomenology Of Meson Family*, Prog. Th. Phys. Suppl. **37**, 21 (1966)

[Pet83] C.Peterson, D.Schlatter, I.Schmitt, P.M.Zerwas, *Scaling Violations In Inclusive E+ E- Annihilation Spectra*, Phys. Rev. D**27**, 105 (1983)

[Rit97] T. van Ritbergen, J.A.M.Vermaseren, S. A. Larin, *The four-loop beta function in quantum chromodynamics*, Phys. Lett. B **400** 379 (1997)

[Sax87] D.H.Saxon, ZEUS Collab., *Development Of The Zeus Detector*, DESY-87-165, Presented at DESY Theory Workshop, Hamburg, Germany, Oct 12-14, (1987)

[Sch91] G.A.Schuler, H.Spiesberger, Physics at HERA proceedings **3**, 1419 (1991)

[Sch98] U.Schneekloth, (ed.). DESY-HERA-98-05 (1998)

[Sjo01] T.Sjostrand *et al.*, *High-energy-physics event generation with PYTHIA 6.1*, Comput. Phys. Commun. **135**, 238 (2001)

[Smi92] W.H.Smith, K.Tokushuku, L.W.Wiggers, Proc. Computing in High-Energy Physics (CHEP), Annecy, France, 1992, C. Verkerk and W.Wojcik (eds.), p.222. CERN, Geneva, Switzerland (1992).
Also in pre print DESY-92-150B

[Sto05] U.Stösslein, private communication

[Tri05] Heavy Flavour Physics Group Trigger Page.
`http://www-zeus.desy.de/physics/hfla/zeus/hfl_trig/`

[Tun01] N.Tuning, *ZUFOs: Hadronic final state reconstruction with calorimeter, tracking and backsplash correction*, ZEUS-Note 01-021, (2001)

[Zeu97] ZEUS Collaboration, *A Microvertex Detector for ZEUS* (unpublished), Tech. Report DESYPRC 97/01, (1997)

[Zeu04] ZEUS Structure Functions and Electroweak Physics working group, Combined H1 and ZEUS proton PDFs (unpublished), 2004, available on
`http://www-zeus.desy.de/physics/sfew/PUBLIC/sfew_results/preliminary/moriond04/zeush1.php`

[Zeu05] Zeus Collab. *Measurements of beauty photoproduction at HERA II*, LP05 Conference, submitted to the Eur. Phys. Soc.(2005)

[Zwe64] G. Zweig, CERN Report No. 8419 TH 412, 1964 (unpublished); reprinted in Developments in the Quark Theory of Hadrons, edited by D. B. Lichtenberg and S. P. Rosen (Hadronic Press, Massachusetts, 1980).

Acknowledgment

The results of this thesis could never have been achieved without the combined efforts of the members of the ZEUS collaboration and many others. I would like to express my special gratitude to:
Robert Klanner for the opportunity to work on my thesis at ZEUS and for his valuable questions and corrections of the drafts of this thesis.
My supervisor Achim Geiser for all his new ideas, enthusiastic discussions and his support at all stages of my analysis.
The "beauty team" for the combined effort to develop the multi-purpose analysis code and for fruitful discussions with all members: Ingo Bloch, Oliver Gutsche, Ursula Samson, A. Elizabeth Nuncio Quiroz and all others.
The heavy flavor working group for the environment where this analysis developed. The MVD group, where I performed my technical task, especially Tobias Haas for his kind support and Alessandro Polini for his unfailing help, no matter for which component of ZEUS.
Specially I would like to thank Katrin for her patience and her encouragement during the last years.
Last but not least, I would like to express my deep gratitude to my family, not only but also for their support and interest in my work.